การวิเคราะห์สมรรถนะและหาสภาวะที่เหมาะสมของระบบร่วมซึ่งประกอบด้วยกระบวนการแก๊สซิฟิเคชั่นของถ่านหินกับชีวมวล เซลล์เชื้อเพลิงชนิดออกไซด์ของแข็งแบบนำโปรตอน และระบบทำความเย็นแบบดูดซึมด้วยลิเธียมโบรไมด์

PERFORMANCE ANALYSIS AND OPTIMIZATION OF COAL/BIOMASS GASIFICATION, PROTON-CONDUCTING SOLID OXIDE FUEL CELL AND A LITHIUM BROMIDE ABSORPTION CHILLER INTEGRATED SYSTEM

รติกร ศรอำพล

RATIKORN SORNUMPOL

วิทยานิพนธ์นี้เป็นส่วนหนึ่งของการศึกษาตามหลักสูตรปริญญาวิศวกรรมศาสตรดุษฎีบัณฑิต

สาขาวิชาวิศวกรรมเคมี

คณะวิศวกรรมศาสตร์

สถาบันเทคโนโลยีพระจอมเกล้าเจ้าคุณทหารลาดกระบัง

พ.ศ.2566

KMITL-2023-EN-D-228-119

PERFORMANCE ANALYSIS AND OPTIMIZATION OF COAL/BIOMASS GASIFICATION, PROTON-CONDUCTING SOLID OXIDE FUEL CELL AND A LITHIUM BROMIDE ABSORPTION CHILLER INTEGRATED SYSTEM

RATIKORN SORNUMPOL

A THESIS SUBMITTED IN PARTIAL FULFILLMENT

OF THE REQUIREMENT FOR THE DEGREE OF

DOCTOR OF ENGINEERING IN CHEMICAL ENGINEERING

SCHOOL OF ENGINEERING

KING MONGKUT'S INSTITUTE OF TECHNOLOGY LADKRABANG

2023

KMITL-2023-EN-D-228-119

หัวข้อวิทยานิพนธ์	การวิเคราะห์สมรรถนะและหาสภาวะที่เหมาะสมของระบบร่วมซึ่งประกอบด้วยกระบวนการแก๊สซิฟิเคชั่นของถ่านหินกับชีวมวล เซลล์เชื้อเพลิงชนิดออกไซด์ของแข็งแบบนำโปรตอน และระบบทำความเย็นแบบดูดซึมด้วยลิเธียมโบรไมด์
นักศึกษา	รติกร ศรอำพล
รหัสประจำตัว	60601170
ปริญญา	วิศวกรรมศาสตรดุษฎีบัณฑิต
สาขาวิชา	วิศวกรรมเคมี
พ.ศ.	2566
อาจารย์ที่ปรึกษาวิทยานิพนธ์	รศ.ดร. ญาณีพร พัชรวรโชติ

บทคัดย่อ

จุดประสงค์หลักของวิทยานิพนธ์นี้คือการศึกษาและออกแบบกระบวนการผลิตพลังงานไฟฟ้าจากเซลล์เชื้อเพลิงชนิดออกไซด์ของแข็งแบบนำโปรตอนเพื่อเป็นแหล่งพลังงานไฟฟ้าทางเลือกในอนาคต โดยแก๊สไฮโดรเจนที่เป็นเชื้อเพลิงในเซลล์เชื้อเพลิงนั้นสามารถผลิตได้จากกระบวนการแก๊สซิฟิเคชั่นของชีวมวล แต่การใช้ชีวมวลเพียงอย่างเดียวอาจจะเกิดปัญหาในด้านการเปลี่ยนแปลงทางฤดูกาลและค่าความร้อนของชีวมวลมีค่าต่ำ ดังนั้นถ่านหินซึ่งมีค่าความร้อนและมีสัดส่วนระหว่างคาร์บอนต่อไฮโดรเจนสูงจึงถูกแนะนำให้ใช้เป็นสารป้อนร่วม โดยปกติแล้วแก๊สไฮโดรเจนที่ได้จากกระบวนการแก๊สซิฟิเคชั่นมักมีสารอื่นปนอยู่เสมอ ดังนั้นกระบวนการแคลเซียมลูปปิ้งจึงถูกติดตั้งต่อมาเพื่อเพิ่มความบริสุทธิ์ของแก๊สไฮโดรเจน โดยการป้อนแก๊สผลิตภัณฑ์ที่ได้จากกระบวนการแก๊สซิฟิเคชั่นเข้าไปยังกระบวนการดังกล่าวทำให้ไม่เพียงแต่เป็นการลดแก๊สคาร์บอนไดออกไซด์ แต่ยังเป็นการลดแก๊สคาร์บอนมอนอกไซด์อีกด้วย ส่งผลให้แก๊สไฮโดรเจนที่ได้จากกระบวนการนี้มีความบริสุทธิ์สูง แก๊สไฮโดรเจนสามารถนำมาใช้เป็นเชื้อเพลิงให้กับเซลล์เชื้อเพลิงชนิดออกไซด์แข็งแบบนำโปรตอนซึ่งผลิตได้ทั้งกระแสไฟฟ้าและความร้อนเหลือทิ้ง เมื่อความร้อนเหลือทิ้งนี้ถูกนำไปใช้ในการขับเคลื่อนระบบทำความเย็น จะสามารถเรียกระบบร่วมระหว่างการผลิตกำลังไฟฟ้า ความร้อน และความเย็นว่าระบบไตรเจนเนอเรชั่น ในวิทยานิพนธ์นี้จะดำเนินการศึกษาผลของสภาวะการดำเนินงานที่มีต่อสมรรถนะของระบบผ่านการจำลองกระบวนการโดยใช้โปรแกรมแอสเพนพลัส เวอร์ชั่น 10 สมการสำหรับการคำนวณองค์ประกอบในชีวมวลและถ่านหิน และแบบจำลองทางไฟฟ้าเคมีซึ่งนำมาใช้หาสมรรถนะทางไฟฟ้าของเซลล์เชื้อเพลิงถูกเขียนอยู่ในบล็อคการคำนวณด้วยภาษาฟอร์แทน เมื่อทราบแนวโน้มของผลของสภาวะดำเนินการแล้ว จะทำการศึกษาหาสภาวะการดำเนินงานที่เหมาะสมโดยใช้โปรแกรมดีไซน์เอ็กเปอร์ท เวอร์ชั่น 11 ผลที่ได้จากการศึกษาแบ่งออกเป็นสองส่วน ส่วนแรกเป็น

การศึกษาการผลิตแก๊สไฮโดรเจนจากกระบวนการแก๊สซิฟิเคชั่นจากถ่านหินกับชีวมวลร่วมกับการดักจับคาร์บอนไดออกไซด์ด้วยกระบวนการแคลเซียมลูปปิ้ง ซึ่งพบว่าเพื่อให้ได้การผลิตแก๊สไฮโดรเจนมากที่สุด (99.59 เปอร์เซ็นต์โดยปริมาตร) กระบวนการแก๊สซิฟิเคชั่นต้องดำเนินงานที่อุณหภูมิเท่ากับ 700 องศาเซลเซียส อัตราส่วนของไอน้ำต่อสารป้อนเท่ากับ 2 และอัตราส่วนของถ่านหินต่อชีวมวลเป็น 0.75:0.25 ส่วนกระบวนการเคมิคอลลูปปิ้งควรดำเนินการที่อุณภูมิของเครื่องคาร์บอเนเตอร์เท่ากับ 450 องศาเซลเซียส อุณหภูมิของเครื่องรีเจนเนอร์เรเตอร์เท่ากับ 950 องศาเซลเซียส และอัตราส่วนแคลเซียมออกไซด์ต่อสารป้อนเท่ากับ 3 โดยระบบดังกล่าวมีประสิทธิภาพทางพลังงานเท่ากับ 42.86 เปอร์เซ็นต์ ซึ่งจะเห็นได้ว่าเมื่อถ่านหินถูกนำมาใช้เป็นสารป้อนร่วมแล้ว จะได้แก๊สไฮโดรเจนปริมาณสูง ในขณะที่การดำเนินการของระบบอยู่ในช่วงปานกลาง โดยเฉพาะอย่างยิ่งอุณหภูมิของคาร์บอเนอเตอร์ที่ใช้เพียง 450 องศาเซลเซียส ซึ่งถือว่าต่ำกว่างานวิจัยทั่วไป ส่วนการศึกษาในส่วนที่สองซึ่งเป็นการผลิตพลังงานไฟฟ้า ความร้อน และความเย็น จากเซลล์เชื้อเพลิงชนิดออกไซด์ของแข็งแบบนำโปรตอนร่วมกับระบบทำความเย็นแบบดูดซึมด้วยลิเธียมโบรไมด์ นั้นพบว่าเมื่อเซลล์เชื้อเพลิงดำเนินงานที่อุณหภูมิ 700 องศาเซลเซียส ความดัน 10 บาร์ สัมประสิทธิ์การใช้เชื้อเพลิง 0.8 และอัตราส่วนการใช้อากาศต่อเชื้อเพลิง เท่ากับ 2 จะได้ประสิทธิภาพของระบบเป็น 93.40 เปอร์เซ็นต์ เมื่อระบบทำความเย็นดำเนินการที่สภาวะที่เหมาะสม จะได้สมรรถนะการทำงานเท่ากับ 0.7238 นอกจากนี้พบว่าเซลล์เชื้อเพลิงที่ผลิตทั้งไฟฟ้าและความร้อนมีประสิทธิภาพทางพลังงานและทางเอ็กเซอร์จีสูงที่สุด ตามมาด้วยระบบไตรเจนเนอเรชั่น การศึกษาในส่วนนี้ได้แสดงถึงประสิทธิภาพและความเป็นไปได้ของระบบไตรเจนเนอเรชั่นที่ประกอบด้วยเซลล์เชื้อเพลิงชนิดออกไซด์ของแข็งแบบนำโปรตอนและระบบทำความเย็นแบบดูดซึมด้วยลิเธียมโบรไมด์

Thesis Title	Performance analysis and optimization of a trigeneration process consisting of coal/biomass gasification, proton-conducting solid oxide fuel cell and a lithium bromide absorption chiller integrated system
Student	Ratikorn Sornumpol
Student ID.	60601170
Degree	Doctor of Engineering
Program	Chemical Engineering
Year	2023
Thesis Advisor	Assoc.Prof.Dr. Yaneeporn Patcharavorachot

ABSTRACT

The main objective of this dissertation is the study and design on power generation from proton-conducting solid oxide fuel cell (SOFC-H^+) for alternative electrical energy source in the future. Hydrogen used as fuel for SOFC-H^+, can be produced from biomass gasification. However, the use of pure biomass has some problems in terms of the variable seasons and low calorific value of biomass. Therefore, coal, which has high calorific value and carbon-to-hydrogen ratio, is recommended to use as co-feed in the gasification. In general, hydrogen products obtained from gasification process always contain other contaminates. Thus, the calcium looping process is subsequently installed to provide purified hydrogen. Feeding the gas product from gasification into the calcium looping process causes reductions not only carbon dioxide but also carbon monoxide. This leads to high purity of hydrogen. The obtained hydrogen can be used as fuel in SOFC-H^+ which produces both electricity and waste heat. When the waste heat is utilized to drive the lithium bromide (LiBr) absorption chiller, cooling can be provided. The combined power, heating and cooling is called as trigeneration process. In this dissertation, the investigation on effects of operating conditions on system performance is performed through the simulation by using Aspen Plus simulator version 10. The equations for calculating composition in biomass and coal and electrochemical model for

determining the electrical characteristics of SOFC-H^+ are written in the calculator block with Fortran. When the trends of operating condition are examined, the optimization is performed through Design Expert version 11. The results obtained from this study can be divided into two parts. The first part is hydrogen production from co-gasification of coal and biomass integrated with calcium looping process. The simulation results revealed that to obtain the maximum hydrogen production (99.59 %vol.), the gasification must be operated at a temperature of 700 °C, a steam to feed ratio of 2 and a coal to biomass ratio of 0.75:0.25 while the chemical looping process should be operated with a generator temperature of 450 °C, a regenerator temperature of 950 °C and a CaO to feed ratio of 3. This system has the energy efficiency of 42.86%. It is found that when coal is used as co-feed, the hydrogen content is high while the operating condition is moderate. Especially, the temperature of carbonation is only 450 °C which is quite lower than other literature. The second part is the combined power, heating and cooling from the SOFC-H^+ and LiBr adsorption chiller. It was found that the SOFC-H^+ operated at a temperature of 700 °C, a pressure of 10 bar, fuel utilization of 0.8 and air-to-fuel ratio of 2 can provide the overall system efficiency as 93.40%. Under the optimal operating conditions of chiller, the coefficient of performance was 0.7238 Additionally, it was found that the combined power and heat system has the highest energy and exergy efficiencies, followed by a trigeneration process. This study presents the efficiency and feasibility of the proposed trigeneration process, consisting of SOFC-H^+ and a LiBr absorption chiller.

ACKNOWLEDGEMENT

I would like to express my sincere gratitude an appreciation to my advisor, Assoc. Prof. Dr. Yaneeporn Patcharavorachot for great supporting throughout this research. Studying for a doctoral engineering degree is the single page of my life.

I would like to thank of my thesis committee Assoc. Prof. Dr. Amornchai Arpornwichanop , Assoc. Prof. Dr. Dang Saebea, Asst. Prof. Dr. Tanawan Pinnarat and Asst. Prof. Dr. Walairat Chandra-ambhorn for their time and useful comments that can improve this research.

I am very thankful to my family for inspiration. Also, special thanks to Ms. Pimchanok Thongphan for making me believe in myself and trust in me.

Ratikorn Sornumpol

CONTENTS

Pages

CONTENTS (CONTINUE)

Pages

CONTENTS (CONTINUE)

Pages

CONTENTS (CONTINUE)

Pages

CONTENTS (CONTINUE)

Pages

LIST OF TABLES

Pages

LIST OF TABLES (CONTINUE)

Pages

LIST OF TABLES (CONTINUE)

Pages

LIST OF FIGURES

Pages

LIST OF FIGURES (CONTINUE)

Pages

LIST OF FIGURES (CONTINUE)

Pages

LIST OF ABBREVIATIONS

A	Active area of cell (m^2)
COP	Coefficient of performance (-)
$D_{an,eff}$	Effective diffusion coefficient of anode side (m^2/s)
$D_{ca,eff}$	Effective diffusion coefficient of cathode side (m^2/s)
$E_{\text{electrode}}$	Activation energy of each electrode (J/mol)
E^0	Open-circuit voltage at the standard pressure (V)
E^{OCV}	Open-circuit voltage (V)
E_{H^+}	Activation energy for the carrier of protons (J/mol)
Ex	Exergy flow rate (W)
ex^{ch}	Specific chemical exergy (J/mol)
$\dot{E}x_{des}$	Exergy destruction rate (W)
ex_i	Specific exergy (J/mol)
ex^{ph}	Specific physical exergy (J/mol)
$\dot{E}x_Q$	Exergy of heat transfer (W)
$\dot{E}x_W$	Exergy of work (W)
F	Faraday constant (C/mol)
H_2^i	Molar flow rate of hydrogen supplied to the integrated system (kmol/hr)
h_j	Specific enthalpy of species *j* (kJ/kg)
I	Current (A)
j	Total current density (A/m^2)
$j_{0,\text{electrode}}$	Exchange current density of each electrode (A/m^2)
k_B	Boltzmann constant (m^2 kg/s K)

LIST OF ABBREVIATIONS

$k_{\text{electrode}}$	Pre-exponential factor of each electrode (A/m^2)
LHV_{biomass}	Lower heating value of biomass (kJ/kg)
LHV_{coal}	Lower heating value of coal (kJ/kg)
LHV_{H_2}	Lower heating value of hydrogen (kJ/kg)
$\dot{m}_{\text{biomass}}$	Mass flow rate of biomass (kg/hr)
$\dot{m}_{\text{coal}}$	Mass flow rate of coal (kg/hr)
m_j	Mass flow rate of species *j* (kg/s)
$\dot{m}_{\text{steam}}$	Mass flow rate of steam (kg/hr)
N_{cell}	Number of cells (cells)
$\dot{n}_{\text{H}_2}$	Molar flow rate of hydrogen (kmol/hr)
$\dot{n}_i$	Molar flow rate of species *i* (kmol/hr)
$\dot{n}_{\text{H}_2,\text{ele}}$	Molar flow rate of hydrogen used in the SOFC-H^+ (kmol/hr)
O_2^i	Molar flow rate of oxygen supplied to the integrated system (kmol/hr)
P	Operating pressure (bar)
$P_{i,\text{electrode}}$	Partial pressure of species *i* at each electrode side (bar)
$P_{i,\text{electrode}}^{\text{I}}$	Partial pressure species *i* at interface of each electrode side (bar)
P_{SOFC}	Power density (W/m^2)
$\dot{Q}$	Heat required for the system (kW)
Q_{evap}	Heat required for the evaporator (kW)
Q_{gen}	Heat required for the generator or desorber (kW)
$Q_{\text{hot utility}}$	Heat required for the hot utility (kW)
$Q_{\text{waste heat}}$	Waste heat recovery from process (kW)

LIST OF ABBREVIATIONS

R	Gas constant (J /K · mol)
R_{ohm}	Resistance of the cell (Ω m^{-2})
s	Entropy at operating temperature (J/K)
T	Operating temperature (K)
T_0	Reference temperature at 298.15 K (K)
U_f	Fuel utilization (-)
V	Cell voltage (V)
W_{COMP}	Compressor consumption (kW)
X_1	Factor
X_2	Dependent variable
y	Response variable

Greek letters

β_0, β_1	Regression coefficient
ε	Error observed in response y.
ε_a	Porosity at anode (-)
$\varepsilon_{Absorption}$	Exergy efficiency of the absorption chiller (%)
ε_c	Porosity at cathode (-)
ε_{CHP}	Exergy efficiency of the integrated system (%)
ε_{exergy}	Exergy efficiency (%)
$\eta_{act,electrode}$	Activation overpotential at each electrode (V)
$\eta_{conc,electrode}$	Concentration overpotential at the electrode (V)
η_{H_2}	Energy efficiency of H_2 production of co-gasification process (%)

LIST OF ABBREVIATIONS

η_{ohm}	Ohmic overpotential (V)
$\eta_{overall}$	Overall efficiency of the SOFC-H^+ (%)
η_{SOFC}	Electrical efficiency of the SOFC-H^+ (%)
η_{Tri}	Trigeneration efficiency (%)
σ_{0,H^+}	Pre-factor of proton conductivity ($S{\cdot}m^{-1}\,{}^{o}C$)
σ_{ele}	Protonic conductivity ($S{\cdot}m^{-1}\,{}^{o}C$)
τ_{an}	Anode thickness (m)
τ_{ca}	Cathode thickness (m)
τ_{ele}	Electrode thickness (m)

Subscripts

abs	Absorber
absorption	Lithium bromide absorption chiller
act	Activation overpotential
anode, an	Anode
cathode, ca	Cathode
ch	Chemical
con	Condenser
conc	Concentration overpotential
CHP	Combined heat and power
CCHP	Combined cooling, heating and power
des	Desorber or generator
ele :	Electrolyte

LIST OF ABBREVIATIONS

evap	Evaporator or cooling capacity
Fuel	Purified hydrogen feed
gen	Generator or desorber
in	Input
j	Species j
o	Reference state (298 K , 1 bar)
out	Output
ohm	Ohmic loss
Overall	Overall
ph	Physical
SOFC	Solid oxide fuel cell
Tri	Trigeneration
W	Work

CHAPTER I

INTRODUCTION

1.1 Background

Currently, the conventional method of generating power, which relies on fossil fuels, faces various challenges. These include the depletion of fossil fuel and the emission of CO_2, a greenhouse gas known to contribute to climate change. Consequently, researchers have turned their focus to developing alternative renewable energy sources that can replace fossil fuels. Among these options, hydrogen has emerged as a promising energy carrier for the future due to its clean and sustainable nature. Hydrogen can serve as a fuel for both mobile and stationary applications and powering fuel cells or internal engines [1]. To support sustainable energy system, hydrogen should be derived from renewable resources, e.g., biomass [2], ethanol [3-4] and biodiesel [5].

Biomass, derived from agricultural residue, serves as a plentiful, easily accessible, and cost-effective alternative renewable energy source. Its key benefit lies in CO_2 neutrality, achieved by balancing CO_2 emissions from production with plant-based CO_2 absorption. Generally, biomass finds extensive use in energy and heat production via the combustion process [6]. Additionally, there has been significant interest in converting biomass into fuels, chemicals, or gaseous products due to their ease of storage, transportation, and handling as energy storage solutions.

In general, there are two thermochemical processes that include pyrolysis and gasification used for converting biomass into useful substance. The choice of methods for producing chemical products from biomass depends on the desired output. In this work, the biomass-to-hydrogen conversion is focused and thus, the gasification process becomes a recommended approach. Currently, the investigation on gasification process based on experiment and process simulation are gaining more attention in terms of gasifier operating conditions and types of gasifying agents. The process simulation of the gasification of animal wastes in a dual fluidized bed gasifier through the Aspen Plus simulator was done by Fernandez-Lopez et al. [7]. Steam and CO_2 were

considered as gasifying agent. They reported that a higher H_2/CO ratio can be provided from a steam gasification. The results showed that high temperatures favored the production of H_2 and CO for both steam and CO_2 gasifying agents. Steam gasification resulted in higher H_2 production, while CO_2 gasification enhanced CO formation. The gasifying agent/biomass ratio influenced CH_4 production and the syngas' low heating value (LHV). For the Fischer-Tropsch process, steam gasification at 850°C with a gasifying agent/biomass ratio of 0.7 was most suitable, while CO_2 gasification at 750°C with a ratio of 0.1 produced syngas with a high LHV for energy production. Shen et al. [8] used a lab-scale auto-thermal gasifier to perform a CO_2 gasification of woody biomass. Their result indicated that the syngas is composed of higher amount of CO. They revealed a significant increase in the composition of CO, accompanied by a decrease in CH_4 levels, which can be attributed to the occurrence of the Boudouard reaction. This reaction facilitates the conversion of carbon and leads to a rise in carbon conversion and cold gas efficiency (CGE) when CO_2 is introduced as an additive agent.

Since biomass as a renewable resource is facing challenges due to its variable availability influenced by factors such as agriculture, season, cultivated area, and agricultural production volume. Moreover, the utilization of biomass for energy generation poses obstacles due to its high moisture content, low bulk density, and low calorific value, which directly impact hydrogen production [9]. To address this issue, numerous researchers have turned their attention to the co-gasification of biomass and coal [10-12]. The reason that coal is suggested to mix with biomass can be explained by its inexpensive, easily transportable, and abundant. Additionally, coal has a higher energy calorific value compared to biomass and thus, the coal gasification exhibits higher efficiency in hydrogen production. Shahabuddin. et al. [10] investigated the performance of the co-gasification between coal and biomass through thermodynamic equilibrium modeling. They analyzed the effect of various parameters, including equivalence ratio, temperature, pressure, and the coal-to-biomass blending ratio, on syngas composition, LHV, and CGE. They reported that increasing biomass concentration in the blend led to a decrease in the yield of CO. A significant drop in CO concentration was observed with a blending ratio above 50%. This decrease in CO was attributed to the decrease in carbon content in the sample, resulting in a reduction of CO by 0.7 to 5.3 percentage points when adding biomass in various proportions. The

conversion of CO_2 followed a similar trend to CO, with significant variations over a biomass ratio of 50%. Hu et al. [11] focused on the synergy effect between coal and biomass during co-gasification in a vertical fixed bed reactor. The result revealed that the co-gasification of coal and biomass resulted in enhanced conversion of residual char and tar into gas. This synergy effect was observed, and it reached its maximum extent at around 40% biomass blending ratio. The interaction between coal and biomass during gasification contributed to this enhanced conversion.

When the coal and biomass is used as feedstock in the gasification process, the synthesis gas or syngas, consisting of H_2, CO, CO_2, and a small amount of CH_4 can be produced. Obviously, there are high amount of CO and CO_2 contaminated in syngas. To increase H_2 yield in the syngas, a subsequent CO_2 removal process becomes necessary. Among various CO_2 capture technologies, chemical looping process, that uses calcium oxide (CaO) to adsorb CO_2 in syngas, stands out as the most promising method. Utilizing calcium oxide (CaO) as a low-cost and abundantly available sorbent, this technology offers cost savings and environmental friendliness [13-14]. When CO_2 presented in syngas is adsorbed on the surface of CaO in a carbonator as an exothermic reaction, the clean syngas as well as calcium carbonate ($CaCO_3$) can be provided. $CaCO_3$ is further regenerated through a regenerator reactor, where it undergoes desorption to yield CO_2 and CaO. Under the operation of a carbonator, it is possible to occur the water gas shift reaction. In a same unit, CO_2 produced from water gas shift reaction is adsorbed by CaO. Therefore, this approach, not only CO_2 but also CO can be reduced.

Nowadays, there are many researchers publishing on the gasification and chemical looping process integrated system [15-17]. However, previous research has focused on a sensitivity analysis with wider range of operating conditions or several types of gasifying agent. The results show the trends of operating conditions on performance of system. Nevertheless, the optimization, determining the global optimal operating conditions, should be performed. In this work, the key operating conditions that affect on performance of system are examined through the statistical method.

As mentioned before, hydrogen can be used as fuel for fuel cells which offer a promising alternative energy source, generating electrical energy from the chemical energy of fuel and oxidant without combustion. When fueled with pure hydrogen, fuel

cells are considered environmentally friendly as they produce electricity, water, and heat. Among various types of fuel cell, solid oxide fuel cell (SOFCs), operating at high temperatures (600-1,000°C), provide several advantages over other fuel cell types. Notably, they achieve high chemical conversion and kinetic rates without relying on costly noble metal catalysts [18]. Additionally, the high-temperature operation of SOFCs enables the utilization of hydrocarbon fuels instead of pure hydrogen, as reforming reactions can take place directly within the fuel cell [19]. Lastly, the high-temperature exhaust gas from SOFCs can be effectively utilized by redirecting it to other heat utilities within the process, thereby improving the overall system efficiency [20]. The SOFCs enable the simultaneous generation of heat and power, commonly known as combined heat and power (CHP) or co-generation process.

Nowadays, there exist two types of solid oxide electrolytes suitable for use in SOFCs. The first type is based on oxygen-ion conductor electrolyte (SOFC-O^{2-}) or conventional SOFCs which offers chemical stability and low electrical resistance [21]. During the operation of SOFC-O^{2-}, steam produced at the anode side will dilute the hydrogen concentration and this leads to a drop in the open-circuit voltage. Thus, the fuel recirculation is required to enhance electrical efficiency [22]. In contrast to SOFC-O^{2-}, the SOFC based on proton-conducting electrolyte (SOFC-H^{+}) produces steam at the cathode side, which enhances the hydrogen concentration at the anode side. As a result, the open-circuit voltage and theoretical efficiency can be improved [23]. In a recent year, there are a number of researchers focused on SOFC-H^{+} in both theoretical and experimental studies [24-30]. From previous study [24], theoretical performance analysis indicated that direct internal reforming SOFC-H^{+} exhibits higher potential than SOFC-O^{2-}. However, under similar operating conditions, actual performance of SOFC-O^{2-} was greater than that of SOFC-H^{+} due to the higher total resistance observed in the latter. Interestingly, it was found from previous works [24-26] that the actual performance of SOFC-O^{2-} was outstanding at high temperatures (around 800 °C), whereas the SOFC-H^{+} exhibits higher performance at lower operating temperatures (around 600 °C). This implies that a protonic conductivity is higher when the operating temperature is lower. Additionally, previous publications also support the suitability of SOFC-H^{+} for low-temperature operation, offering advantages such as wider material options and reduced fabrication and operating costs [30].

During SOFC operation, high-temperature exhaust gases are always generated at both the anode and cathode outlets. This waste heat can be effectively utilized harnessed as a heat source for thermally driven cooling systems. While vapor compression is the prevalent method in refrigeration systems, the absorption chiller presents a novel option for enhancing overall system efficiency. The system offers numerous advantages over vapor compression, including reliability, absence of moving parts, and extended lifespan. Utilizing waste heat to drive the chiller results in lower costs compared to electricity consumption. When the absorption chiller is integrated into the system, it is referred to as combined cooling, heating, and power (CCHP) or trigeneration process.

Previous research has focused on studying the trigeneration of integrated conventional SOFC (SOFC-O^{2-}) and absorption chiller systems which founded that the integrated system yields high overall system performance. Ozcan et al. [31] evaluated the performance of an integrated trigeneration system comprising SOFC, organic Rankine cycle, and absorption chiller. The results indicated that the thermochemical gasifier exhibits the highest energy and exergy efficiencies among the subunits within the overall system. Pandya et al. [32] developed a model of the integration of SOFC and vapor absorption refrigeration system for various refrigerated trucks, i.e., series and parallel. The results revealed that the parallel configuration exhibited improved thermo-economic performance. Gwak et al. [33] presented a model of trigeneration utilizing a high-temperature (HT-) proton exchange membrane fuel cell (PEMFC) and LiBr-H_2O absorption chiller. The exhaust gas obtained from HT-PEMFC is utilized to heat up water, and the hot water is pumped to recover energy in conjunction with a lithium bromide (LiBr) solution. Simulation results indicated that high current operation in the HT-PEMFC stack is necessary to attain the required cooling capacity. Katsaros et al. [34] developed a model of trigeneration, incorporating gasification, SOFC and NH_3 solution absorption chiller. The results demonstrated that increasing the air-to-fuel ratio and gasification temperature improved the overall system performance.

From the literature survey, it is found that the trigeneration system aims to provide electricity, heat, and cooling energy for residential areas. However, the integration between SOFC-H^+ and absorption chiller systems has not been extensively explored. Although the use of SOFC-H^+ instead of SOFC-O^{2-} may provide same trends

of performance. Due to the fact that the main attractive feature of SOFC-H^+ is a complete conversion of fuel and oxidant into products. Therefore, the operating condition of an SOFC-H^+ must carefully identify in the integration of SOFC-H^+ and absorption chiller to compromise between electrical performance and thermal performance. In order to clarify the possibility of integration between SOFC-H^+ and absorption chiller, not only sensitivity analysis but also optimization is performed. Additionally, the energy and exergy efficiencies are determined to ensure that this integrated system is useful for operation.

1.2 Objectives

1.2.1 To examine the effect of operating conditions of coal/biomass gasification integrated with a calcium looping carbon dioxide capture process on hydrogen production.

1.2.2 To identify the optimal operating conditions of coal/biomass gasification integrated with a calcium looping carbon dioxide capture process that maximizing hydrogen production.

1.2.3 To determine the energy efficiency of coal/biomass gasification integrated with the calcium looping carbon dioxide capture process.

1.2.4 To examine the effect of operating conditions of the SOFC-H^+ integrated with a LiBr absorption chiller on the system performance.

1.2.5 To identify the optimal operating conditions the SOFC-H^+ integrated with a LiBr absorption chiller that maximizes system performance.

1.2.6 To determine the energy and exergy efficiencies of trigeneration process, consisting of SOFC-H^+ and LiBr absorption chiller.

1.3 Scopes of work

This dissertation can be divided into two main parts as follows:

1.3.1 Coal/biomass gasification integrated with a calcium looping carbon dioxide capture process.

1.3.1.1 develop the model of gasification from biomass and coal through Aspen Plus simulator version 10.

1.3.1.2 validate the model proposed in 1.3.1.1 with the experimental data extracted from literature.

1.3.1.3 develop the model of calcium looping carbon dioxide capture process through Aspen Plus simulator version 10.

1.3.1.4 validate the model proposed in 1.3.1.3 with the experimental data extracted from literature.

1.3.1.5 investigate the effect of conditions in gasification (i.e. gasification temperature, steam to feed ratio, and coal to biomass ratio) on hydrogen production.

1.3.1.6 investigate the effect of conditions in calcium looping carbon dioxide capture process (i.e. carbonator temperature, regeneration temperature, and CaO to feed mass ratio) on hydrogen production.

1.3.1.7 perform the optimization of the gasification and calcium looping process that provide the maximum hydrogen production through Design Expert 11.

1.3.1.8 determine the energy efficiency of coal/biomass gasification integrated with the calcium looping process.

1.3.2 Trigeneration process consisting of SOFC-H^+ and LiBr absorption chiller.

1.3.2.1 develop the model of SOFC-H^+ through Aspen Plus simulator version 10.

1.3.2.2 Validate the model proposed in 1.3.2.1 with the experimental data extracted from literature.

1.3.2.3 Develop the model of LiBr absorption through Aspen Plus simulator version 10.

1.3.2.4 Validate the model proposed in 1.3.2.3 with the experimental data extracted from literature.

1.3.2.5 Examine the effect of operating conditions in SOFC-H+ (i.e. operating pressure, operating temperature, fuel utilization and air to fuel ratio) on electrical efficiency and overall efficiency.

1.3.2.6 Examine the effect of operating conditions in LiBr absorption (i.e. the hot water mass flow rate, hot water and steam inlet temperature, evaporator temperature and generator temperature) on COP.

1.3.2.7 Perform the optimization of the SOFC-H^+ and LiBr absorption chiller that provide the maximum system performance through Design Expert 11.

1.3.2.8 Perform the energy and exergy analysis of trigeneration process, consisting of SOFC-H^+ and LiBr absorption chiller.

1.4 Expected benefit

1.4.1 To obtain the models of coal/biomass gasification integrated with calcium looping carbon dioxide capture process.

1.4.2 To obtain the models of trigeneration process consisting of SOFC-H^+ and LiBr absorption chiller.

1.4.3 To understand the effect of important operating conditions in coal/biomass co-gasification and calcium looping carbon dioxide capture process on hydrogen production.

1.4.4 To understand the effect of important operating conditions in SOFC-H^+ and LiBr absorption chiller on overall system efficiency.

1.4.5 To provide the optimal conditions of coal/biomass co-gasification and calcium looping carbon dioxide capture process for hydrogen production.

1.4.6 To provide the optimal conditions of trigeneration process, consisting of SOFC-H^+ and LiBr absorption chiller for producing electricity, heating and cooling.

1.5 Dissertation overview

This dissertation is divided into six chapters as follows;

Chapter I presents background and motivation, objectives, scopes of work and the expected benefit.

Chapter II describes the main principle of gasification process, calcium looping carbon dioxide capture, the basic knowledge, operation, electrochemical model of

SOFC as well as absorption chiller principle and trigeneration process definition. The equations used to evaluate performance of integrated process like thermodynamic and exergy efficiency analysis are explained in this chapter. Additionally, this chapter provides the general concept which is used to optimize systems such as factorial design, analysis of variance (ANOVA) and design of experiment (DOE). Lastly, previous publication reported on the investigations of gasification, chemical looping, carbon capture process, SOFC, absorption chiller, co-generation and trigeneration system are reviewed.

Chapter III proposes methodology, the development of mathematical model of both processes : (1) co-gasification of biomass and coal integrated with calcium looping carbon dioxide capture process and (2) SOFC-H^+ integrated with LiBr absorption chiller system. The sensitivity analysis method is implemented to study the significant operating conditions on hydrogen production, COP, electrical and overall efficiency. The analysis of variance method is applied to optimize system after optimization process completely. Finally, the thermodynamic efficiency is applied to evaluate system performance.

Chapter IV presents the performance analysis and optimization of co-gasification of coal and biomass integrated with calcium looping carbon dioxide capture process. The contents are included the comparison between model predictions and experimental results extracted from the literature, the effects of the operating conditions in process on hydrogen production, the optimization of process and energy efficiency.

Chapter V presents the performance analysis and optimization of a trigeneration process consisting of SOFC-H^+ and a LiBr absorption chiller. The comparison results obtained from the simulation of SOFC-H^+ and LiBr absorption chiller with the experimental data, the performance analysis of integrated process with wider range of operating conditions, the optimization of integrated process and the exergy efficiency are explained in this chapter.

Chapter VI shows the summary of this work and recommendation for the future work.

CHAPTER II

THEORY AND LITERATURE REVIEWS

2.1 Biomass [8]

Biomass comprises organic matter derived from living organisms and can serve as an energy source in both animal and plant forms. It undergoes biochemical and thermochemical processes to transform into solid or liquid biofuels, and scientists categorize it as a renewable energy source.

2.2 Coal [35]

Coal, a fossil fuel, primarily consists of carbon and hydrogen. Its combustion generates higher heat compared to biomass. With abundant reserves, easy transport, and low cost, coal is suitable for power generation. However, its drawback lies in the sulfur content, leading to the production of acidic gases that can impact the environment.

2.3 Gasification process [36]

Gasification is a controlled combustion process using gasifying agents like steam and air to convert solid materials into gas. The resulting gas, known as synthesis gas, contains hydrogen and carbon monoxide, along with methane, carbon dioxide, and steam. The optimal temperature for this process is 600 °C. The biomass gasification process can be summarized in the following steps. Drying process or drying zone, in this step, moisture in biomass will rapidly decrease and evaporate from biomass in vapor phase. The operating temperature range is 100 – 200 °C. Moisture in biomass will decrease below 5 % wt/wt

Pyrolysis zone or devolatilization is biomass decomposition without oxygen. Volatile matter, tar and hydrocarbon evaporate from biomass. Finally, it remained charcoal.

Oxidation zone or combustion process is a reaction between solid carbon and oxygen. When carbon and hydrogen are combusted and then, converted to carbon dioxide and water as Eqs. (2.1) and (2.2). If it has limited oxygen. The reaction may be partial oxidation and product is carbon monoxide.

$$C + O_2 \rightarrow CO_2 \quad (2.1)$$

$$H_2 \rightarrow 0.5O_2 \rightarrow H_2O \quad (2.2)$$

Reduction zone is step without oxygen. The carbon dioxide from oxidation zone converts from reduction reaction. Carbon dioxide can react with carbon and formed to be carbon monoxide (Eq. (2.3)). This reaction is called as Boudouard reaction which the favorable temperature is 800 °C. In addition, methane formation in gasification is a process that converts biomass or other carbon-rich materials into methane gas. The process involves heating the material to a high temperature in the presence of steam or carbon dioxide, which causes the material to break down into its constituent molecules. These molecules then recombine to form methane (Eq. (2.4)).

$$C + CO_2 \rightarrow 2CO \quad (2.3)$$

$$C + 2H_2 \rightarrow CH_4 \quad (2.4)$$

2.4 Carbon dioxide capture with calcium looping process [37]

In general, the synthesis gas obtained from gasification H_2, CO, CO_2 and CH_4. In order to provide higher H_2 yield, the contaminations, i.e., CO and CO_2 should be removed. Among various technologies of carbon dioxide capture process, the carbon dioxide adsorption process has been received much interest since the calcium oxide (CaO) used as adsorbent is abundant resource, cheap and high efficiency. Figure 2.1 shows the carbon dioxide capture with CaO adsorbent at atmospheric pressure and operating temperature 650 °C. CaO particle reacted with CO_2 in a carbonator unit and formed to be calcium carbonate ($CaCO_3$) that named carbonation reaction then mixed

stream spliced to be CaO particle and flue gas and recycled back to calciner unit for adsorbent regeneration process. Increasing temperature more than 900 °C will shift reverse chemical equilibrium back to high purity CO_2. The energy efficiency improvement method is implemented heat integration between carbonator unit and calciner unit. Exothermic reaction of carbonation reaction (Eq. (2.5)) released heat to endothermic reaction of calcination reaction (Eq. (2.6)) in a regeneration unit.

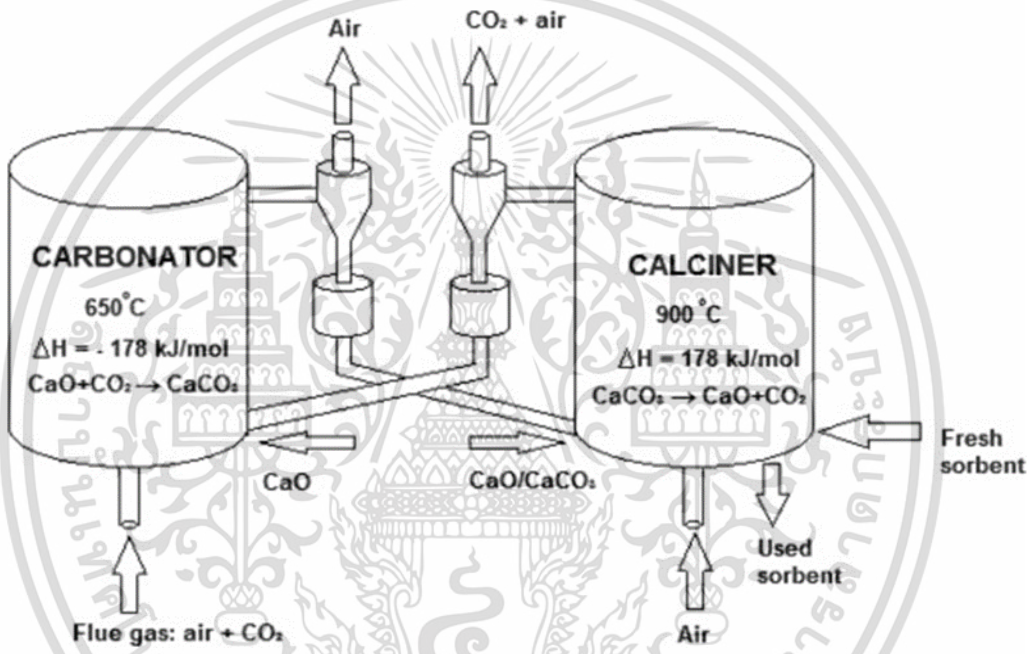

Figure 2.1 Carbon dioxide capture with calcium oxide [38].

Carbonation reaction

$$CaO + CO_2 \rightarrow CaCO_3 \qquad (2.5)$$

Calcination reaction

$$CaCO_3 \rightarrow CaO + CO_2 \qquad (2.6)$$

2.5 Sorption enhanced water-gas shift process [34]

The carbon dioxide capture process is introduced to remove CO_2 from the synthesis gas. However, synthesis gas is also composed of CO. In general, the water-gas shift reaction (Eq. (2.7)) can be used to decrease amount of CO. However, it can be observed that CO_2 is always generated during water-gas shift reaction. Thus, it is possible to separate the CO_2 produced from water-gas shift reaction by using the CaO absorbent in a same unit. This is called as the sorption-enhanced water-gas shift (SE-WGS) process which can reduce both CO and CO_2 and thus, higher H_2 yield can be provided.

$$CO + H_2O \leftrightarrow H_2 + CO_2 \tag{2.7}$$

2.6 Solid oxide fuel cell (SOFC-O^{2-}) [39]

A solid oxide fuel cell (SOFC) is a device for large power plants that converts chemical energy in hydrogen to electricity and heat through exothermic reactions. It operates within a temperature range of 600-1,000°C, offering high efficiency and fuel flexibility. It can utilize various fuels like coal synthesis gas, natural gas, and ethanol, which easily undergo steam reforming. The conventional SOFC is based on an oxygen-conducting electrolyte (SOFC-O^{2-}). The SOFC is divided into three sections: electrolyte, anode, and cathode. In the anode, hydrogen gas flows through a porous medium and oxidizes with oxygen ions, forming steam and electron water (Eq. (2.8)). The electron flows from the anode to the cathode. In the cathode, oxygen diffuses through a porous medium and reacts with electron to form oxygen ions (Eq. (2.9)) that travel from the cathode to the anode. The overall reaction is expressed in (Eq. (2.10)). It can be seen that the SOFC not only produce electricity but also provides steam and heat as by-product. The principle of SOFC-O^{2-} is shown in Figure 2.2.

$$H_2 + O^{2-} \rightarrow H_2O + 2e^- \tag{2.8}$$

$$0.5O_2 + 2e^- \rightarrow O^{2-} \tag{2.9}$$

$$H_2 + 0.5O_2 \rightarrow H_2O \tag{2.10}$$

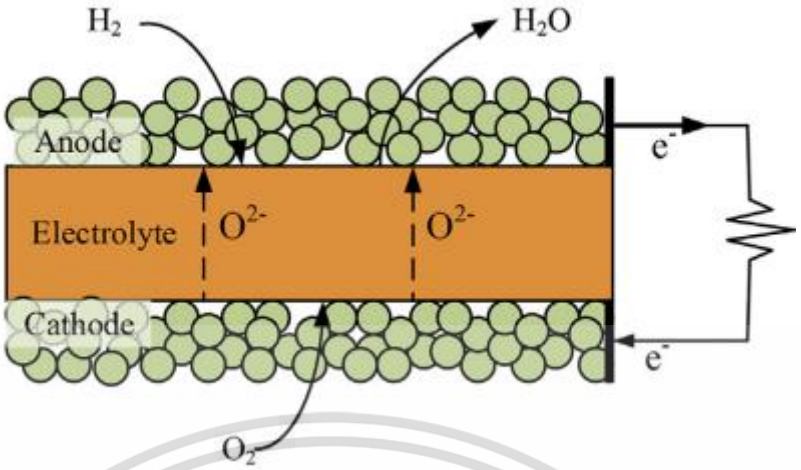

Figure 2.2 The principle of SOFC-O^{2-} [39].

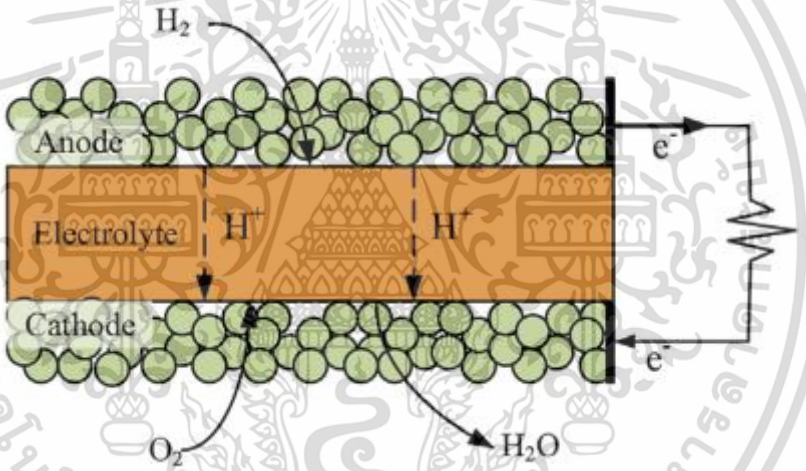

Figure 2.3. The principle of SOFC-H^+ [39].

2.7 Proton conducting solid oxide fuel cell (SOFC-H^+) [40]

Apart from an electrolyte based on an oxygen-conducting, a solid oxide-based proton conductor can be used as an electrolyte in SOFC. The SOFC based proton conducting electrolyte can be called in short as SOFC-H^+. The main difference between SOFC-O^{2-} and SOFC-H^+ is the location of steam generation. For the SOFC-H^+, steam is produced at the cathode side. This means that no dilution of steam at the anode side, the concentration of hydrogen an anode is higher and thus, the theoretical voltage can be enhanced. The principle of SOFC-H^+ as shown in Figure 2.3 involves hydrogen

oxidation at the anode where hydrogen is decomposed into electron and proton. (Eq. (2.11)). Electron flows through the electric circuit from the anode to the cathode. While proton travels through electrolyte from anode to cathode and reacts with oxygen supplied from the cathode (Eq. (2.12)). This results in the formation of water molecules at the cathode side.

$$H_2 \rightarrow 2H^+ + 2e^- \tag{2.11}$$

$$0.5O_2 + 2H^+ + 2e^- \rightarrow H_2O \tag{2.12}$$

2.8 Electrochemical model of SOFC-H$^+$ [40]

The electrochemical model is used to predict the cell potential and various losses at different current density.

2.8.1 Theoretical cell potential [36]

Theoretical cell potential or open-circuit potential (E^{OCV}) occurs from the difference potential between anode and cathode electrode. This is the maximum potential occurred in the SOFC. For SOFC-H$^+$, the open-circuit potential derived from Nernst equation is shown as Eq. (2.13).

$$E^{OCV} = E^{O} - \frac{RT}{2F}\ln\left(\frac{P_{H_2O(ca)}}{P_{H_2(an)}P_{O_2(ca)}^{0.5}}\right) \tag{2.13}$$

where E^0 is cell potential at atmospheric pressure.

2.8.2 Actual cell voltage [36]

The actual cell voltage (V) of a fuel cell is always lower than the theoretical cell potential due to three types of overpotential: activation overpotential, concentration overpotential, and ohmic overpotential. Thus, the actual cell voltage can be calculated as as Eq. (2.14)

$$V = E^{OCV} - \left(\eta_{act} + \eta_{ohm} + \eta_{conc}\right) \tag{2.14}$$

2.8.3 Activation overpotential (η_{act}) [41]

This overpotential is occurred from the electro chemical reaction at anode and cathode side and caused energy loss from electron movement that require high activation energy (E_a). The equations used for calculating the activation overpotential are shown below:

$$\eta_{act,electrode} = \frac{RT}{F}\sinh^{-1}\left(\frac{j}{2j_{0,electrode}}\right) \tag{2.15}$$

where $j_{0,electrode}$ is the exchange current density of each electrode which can be calculated through Eq. (2.16).

$$j_{0,electrode} = \frac{RT}{nF}k_{electrode}\exp\left(-\frac{E_{electrode}}{RT}\right) \tag{2.16}$$

2.8.4 Concentration overpotential (η_{conc}) [41]

This overpotential arises from concentration differences at the electrode surface, electrolyte, and three-phase boundary layers, resulting in mass transfer resistance and concentration overpotential. The concentration overpotential at anode and cathode side is expressed as Eqs. (2.17) and (2.18), respectively.

$$\eta_{conc,an} = \frac{RT}{2F}\ln\left(\frac{P_{H_{2(an)}}}{P^{\mathrm{I}}_{H_{2(an)}}}\right) \tag{2.17}$$

$$\eta_{conc,ca} = \frac{RT}{2F}\ln\left(\left(\frac{P_{O_{2(ca)}}}{P^{\mathrm{I}}_{O_{2(ca)}}}\right)^{0.5}\frac{P^{\mathrm{I}}_{H_2O_{(ca)}}}{P_{H_2O_{(ca)}}}\right) \tag{2.18}$$

while the partial pressure of H_2, H_2O and O_2 at three-phase boundary layers are shown in Eqs. (2.19)-(2.21).

$$P^{\mathrm{I}}_{H_2} = P - \left(P - P_{H_{2(an)}}\right)\exp\left(\frac{RT\tau_{an}}{2FD_{an,eff}P}j\right) \tag{2.19}$$

$$P_{O_2}^{\mathrm{I}} = P_{O_{2(ca)}} - \frac{RT\tau_{ca}}{2FD_{ca,eff}} j \quad (2.20)$$

$$P_{H_2O}^{\mathrm{I}} = P_{H_2O_{(ca)}} + \frac{RT\tau_{ca}}{4FD_{ca,eff}} j \quad (2.21)$$

where τ_{an} and τ_{ca} are the thickness of anode and cathode, respectively. $D_{an,eff}$ and $D_{ca,eff}$ are the effective gas diffusivity coefficients in the anode and cathode, respectively.

2.8.5 Ohmic overpotential (η_{ohm}) [41]

Ohmic overpotential caused from electrode resistance and proton transport resistance in electrolyte as Eq. (2.22).

$$\eta_{ohm} = jR_{ohm} \quad (2.22)$$

where R_{ohm} is the resistance of the cell. In general, R_{ohm} can be estimated from the effective distance between the electrolyte thickness (τ_{ele}) and electrolyte conductivity (σ_{ele}), as given Eq. (2.23).

$$R_{ohm} = \frac{\tau_{ele}}{\sigma_{ele}} \quad (2.23)$$

Since the $BaZr_{0.8}Y_{0.2}O_3$ (BZY) electrolyte is a mixed conductor, σ_{ele} represents the protonic conductivity as well as ionic conductivity as expressed in Eq. (2.24)

$$\sigma_{ele} = \sigma_{0,H^+} T^{-1} \exp\left(-\frac{E_{H^+}}{k_B T}\right) \quad (2.24)$$

where σ_{0,H^+} is the pre-factor obtained from fitting with the experimental data. E_{H^+} is the activation energy for the carrier of protons. The k_B is Boltzmann constant.

2.8.6 Characteristic performance curve of fuel cell [35]

Characteristic performance curve of solid oxide fuel cell shows the relationship between cell voltage and current density. The curve, as shown in Figure 2.4, is a specific characteristic of fuel cells. At no load or no current density, the fuel cell can achieve the maximum voltage or the theoretical voltage. However, when the current density is applied to the fuel cell, the actual cell voltage or operation voltage will suddenly drop due to three types of overpotential. In the first stage, as the current density increases, the cell voltage sharply decreases due to activation overpotential, requiring additional energy to overcome the activation energy. The second stage corresponds to ohmic overpotential caused by electrical resistance in the electrode and electrolyte. In the last stage, known as concentration overpotential, the voltage curve approaches zero due to inadequate gas diffusion to the porous zone and insufficient concentration gradient for the electrochemical reaction.

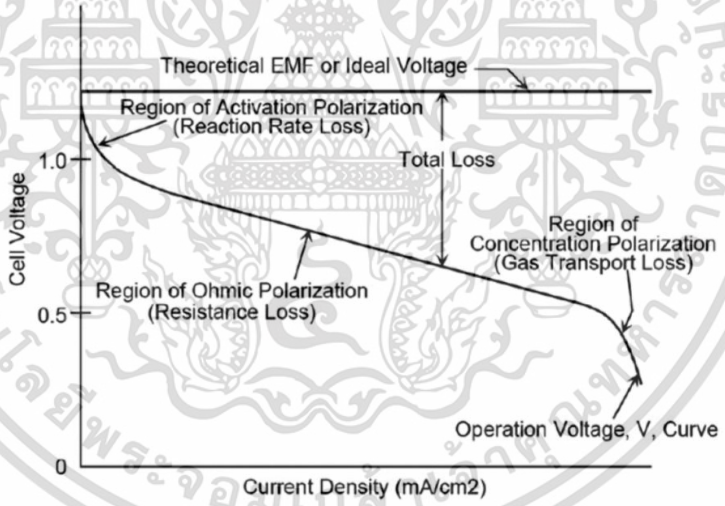

Figure 2.4 The polarization curve of fuel cell [42].

2.9 Absorption chiller [43]

The thermal driving source of absorption chiller system is low quality waste heat. (Temperature range 60 – 200 ℃) The working fluids are refrigerant and absorbent which are used to absorb vapor of refrigerant and separate from absorbent. The principal diagram is shown in Figure 2.5.

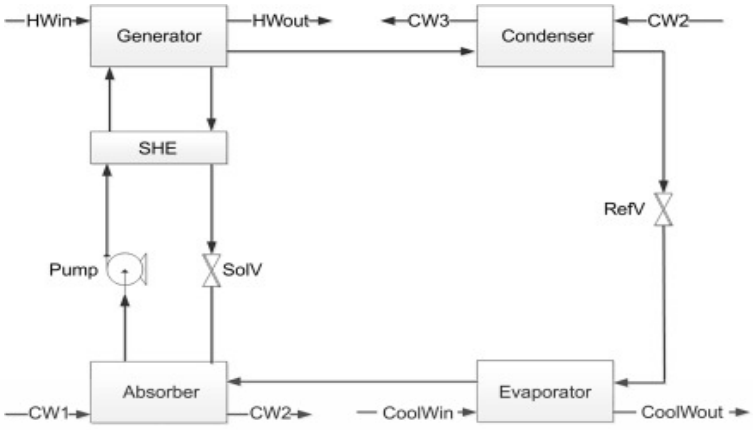

Figure 2.5 The single stage absorption chiller process [43].

The primary process begins with heating the solution in the desorber to produce superheated vapor refrigerant and a high concentration of absorbent. The vapor refrigerant is then sent to the condenser unit to condense and release heat to the surroundings. The saturated refrigerant liquid flows sequentially through the expansion valve and evaporator unit. The saturated refrigerant vapor is then recirculated back to the desorber unit to absorb with a high concentration of absorbent.

2.10 Trigeneration process [31]

The trigeneration process is consisted of heating, electricity, and cold production. It developed from a cogeneration system that implemented low grade waste heat to drive vapor absorption refrigeration system and enhanced overall system efficiency.

2.11 Exergy and thermodynamic analysis [2]

Thermodynamic analysis is a physics branch dealing with energy and its conversion into various forms, such as mechanical energy in internal combustion engines and electrical energy in fuel cells. Energy stored can be transformed into different forms, but there is always a loss during the transformation. When analyzing the thermodynamic efficiency of solid oxide fuel cells, both electrical and thermal efficiency are considered based on power generation and heat recovery. The calculation method involves mass and

energy balance within the system boundary, and it is generally defined as the ratio of energy output to energy input as expressed in Eq. (2.25)

$$\eta = \frac{\dot{E}_{output}}{\dot{E}_{input}} \tag{2.25}$$

For co-gasification of biomass and coal integrated with calcium looping carbon dioxide capture process, it defined thermal efficiency as output energy of hydrogen production to input energy of biomass feeding which can be calculated as Eq. (2.26).

$$\eta_{H_2}(\%) = \frac{m_{H_2} \times LHV_{H_2}}{m_{biomass} \times LHV_{biomass} + m_{coal} \times LHV_{coal}} \times 100 \tag{2.26}$$

For a SOFC-H^+, it defined thermal efficiency as electricity generation to input energy of hydrogen feeding, which can be computed as Eq. (2.27).

$$\eta_{SOFC} = \frac{(P_{SOFC} - W_{COMP_1} - W_{COMP_2})}{\left(\dot{n}_{H_2} \times LHV_{H_2}\right)_{anode,in}} \tag{2.27}$$

For vapor absorption refrigeration unit, thermal efficiency defined as cooling duty from evaporation unit to waste heat input from cogeneration process. It is called as coefficient of performance (COP), which can be expressed as Eq. (2.28).

$$COP = \frac{Cooling\ capacity}{Waste\ heat\ input} = \frac{Q_{evap}}{Q_{waste\ heat}} \tag{2.28}$$

For a trigeneration process, it can calculate energy efficiency from Eq. (2.29).

$$\eta_{Tri} = \frac{P_{SOFC-H^+} + Q_{waste\ heat} + Q_{evap} - W_{COMP_1} - W_{COMP_2}}{\left(\dot{n}_{H_2} \times LHV_{H_2}\right)_{anode,in}} \tag{2.29}$$

Exergy analysis is a thermodynamic method that enhances process efficiency by considering the second law of thermodynamics. It quantifies the maximum available

energy that can be extracted from the difference between the system and its surroundings. This extractable energy is useful for performing work. In a closed system, properties like enthalpy, entropy, volume, pressure, temperature, and chemical potential reach equilibrium with the system's surroundings. In an open system, where substances flow, the ability to do work depends on the enthalpy and entropy of the substances. The difference in extracted work is known as physical exergy and can be expressed mathematically as Eq. (2.30).

$$ex_{ph} = (h - h_0) - T_0(s - s_0) \tag{2.30}$$

From this condition, it considers only physical process and not chemical composition. If it considers the difference chemical composition and proportion between system and environment. It can calculate chemical exergy as Eq. (2.31).

$$ex_{ch} = \sum y_i ex_{ch,i} + RT_0 \sum y_i \ln y_i \tag{2.31}$$

When it considers another chemical exergy term and combine in physical exergy. Total exergy will be shown as Eq. (2.32)

$$ex_i = (h - h_0) - T_0(s - s_0) + \sum y_i ex_{ch,i} + RT_0 \sum y_i \ln y_i \tag{2.32}$$

In all processes, it has heat transfer, chemical reaction and has always entropy fluctuation. It affected enhanced system entropy. It will decrease chemical exergy at system outlet. Exergy analysis is quality of energy analysis that is based on the second law of thermodynamic rules. This phenomenon is called exergy destruction and can write as Eq. (2.33)

$$\dot{E}x_{des} = \sum_{in} \dot{n}_i ex_i + \dot{E}x_Q - \sum_{out} \dot{n}_i ex_i + \dot{E}x_W \tag{2.33}$$

2.12 Design of experiment [44]

A cost-effective experiment yields accurate data and serves as a reliable basis for decision-making. The quality of an experiment determines the realism of the data obtained and aids in determining whether further testing is necessary. Experimental design plays a crucial role in achieving these objectives by planning the study of factors and their impact

on the process or desired outcomes. Each experiment involves treatments, which are the variables of interest affecting the response variables. Treatment combinations, factors, response variables, and noise variables influence the response variable but are not the primary variables of interest. Environmental conditions significantly influence these factors.

2.12.1 Factorial design 2^3

Factorial design 2^3 is the experimental design consisting of three factors and each factor consisted of 2 levels: the number of experiments was obtained. A total of 8 trials were high and low, as shown in Table 2.1, where A, B and C were the experimental factors.

Table 2.1 Factorial design 2^3

Run	A	B	C	Combination
1	-	-	-	1
2	+	-	-	A
3	-	+	-	B
4	+	+	-	Ab
5	-	-	+	C
6	+	-	+	Ac
7	-	+	+	Bc
8	+	+	+	Abc

To determine the factor effect estimate, it can be calculated from the contrast of the cofactor experiment. For the definition of contrast, it is the difference between the sum of the responses of high values. (+) and the response of the low value (-) itself is shown in the Eqs (2.34) - (2.38).

Contrast = sum of responses of high (+1) – sum of responses of low (-1)

Contrast of main effect of A can write as example.

$$A = \frac{1}{8n}[a - 1 - b + ab - c + ac - bc + abc] \quad (2.34)$$

The interaction effect AB can be as

$$AB = \frac{1}{8n}[1 - a - b + ab + c - ac - bc + abc] \quad (2.35)$$

The interaction effect ABC can be as

$$ABC = \frac{1}{8n}[a - 1 + b - ab + c - ac - bc + abc] \quad (2.36)$$

It can write in general equation from as

$$AB...K = \frac{2}{n2^k}(Contrast_{AB..K}) \quad (2.37)$$

After that it will calculate to find the sum of squares.

$$SS_{AB..K} = \frac{1}{n2^k}(Contrast_{AB..K})^2 \quad (2.38)$$

Finally, all the values were put in the Analysis of Variance (ANOVA) table, found the F_0 values, analyzed which variables had a statistically significant effect, and plot graph of the residual values and observed values. The resulting residual should be distributed randomly because it represents the consistency of the data.

2.13 Literature reviews

Katsaros et al. [34] studied a novel tri-generation system using municipal solid waste gasification, SOFC, and ammonia-water absorption chiller. Aspen Plus simulator was used to model the system and analyze the impact of various operating parameters on overall performance. The results showed that lower air equivalent ratios and higher gasification temperatures improved system efficiency. The system's suitability for meeting electricity and cooling demands in hospital buildings was also investigated. Heat requirements could be met up to 55%. With a projected 20-year operation, the payback period was 4.5 years, and the net present value exceeded 5 million euros.

Somers et al. [45] developed a single- and double-effect water/lithium bromide absorption chiller designs involved numerical modeling in Aspen Plus. The model setup and calculation results were compared with experimental data from reference sources to assess accuracy. Error values for all parameters in the single-layer and double-layer systems, compared to experimental data, were found to be 3 percent and 5 percent, respectively.

Xiang et al. [46] established an electrochemical and thermodynamic model for coke-oven gas fueled SOFC integrated with anode off-gas recirculation and chemical looping combustion. Mathematical model created from original Aspen Plus process structure. The new configuration recycles waste gas for reaction and uses chemical looping combustion technology. Old configuration had high steam consumption and carbon dioxide emissions. The novel process achieves net electricity generation of 315.8 MW, improved exergy efficiency of 63.1%, and zero direct CO_2 emissions.

Arteaga-Pérez et al. [47] analyzed and developed a mathematical model for bagasse gasification unit integrated with SOFC to predict thermal and exergy efficiency. Applying Gibbs chemical equilibrium in gasifier and analyzing fuel cell fed with syngas. Model accuracy tested against laboratory experiments using prototype gas bubble fluidization reactor. Experimenting with bagasse and rice husk biomass, considering heat loss, tar formation, water gas shift, and hydrogen conversion. Optimal conditions found at 1023 K and air factor of 0.30, resulting in 35.20% exergy efficiency and 58.85% energy efficiency. The gasifier contributes 75-80% of total exergy destruction after system integration.

Mehrpooya et al. [48] investigated and analyzed 23 different biomass sources in the development of modeling and simulation for biomass gasification process. Proposed model based on Gibbs free energy minimization was used to examines the effect of operating conditions that include gasifier, air and steam temperature, air-to-fuel ratio, and steam-to-biomass ratio on hydrogen gas yield. The result indicated that gasification temperature and steam-biomass ratio significantly impacted on the syngas compositions and heating value. Biomass moisture has the most significant influence on syngas production efficiency. Results also indicated high exergy efficiency (around 90.0%) in the drying stage, with a notable exergy destruction rate compared to other stages.

Salman et al. [49] explored technical potential of integrating gasification processes with existing combined heat and power (CHP) plants for the production of dimethyl ether (DME) or methanol using refuse-derived fuel. Heat and mass balance integration methods were employed to develop and simulate polygeneration processes for heat, power, and biofuel production. Technical and economic indicators were analyzed and compared to evaluate the potential of integrating biofuel production processes. The integrated approach assumed that combined heat and electricity systems could provide the necessary heat for gasification and DME production. Additionally, waste heat from gasification could be utilized in the CHP system. Waste fuel was used as the feedstock for the gasification system instead of biomass fuel. The energetic efficiency of methanol production through process integration was found to be 67%, while DME production achieved 65% efficiency. These efficiencies were higher than those of standalone DME and methanol processes, which achieved efficiencies of 51% and 53%, respectively, but lower than the standalone CHP plant's efficiency of 81%. The performance of the polygeneration system depended on the size of the gasifier in combination with the CHP system, as well as the conversion value of the synthetic DME product, including the recycling of residual syngas back into the DME reactor or its combustion in the CHP system's boiler. Simulation results indicated that single-flow reaction systems yielded higher conversion percentages of DME compared to non-recycled synthetic gas recirculating systems.

Loha et al. [50] investigated the conversion of rice husk into syngas. Rice husk with known proximate and ultimate analysis was introduced into a fluidized bed gasifier at a temperature of 750°C and pressure of 1.05 bar, with a constant feed rate of 1 kg/hr. The steam-to-biomass ratio (S/B) was varied from 0.75 to 2.00. A comparison between the simulated results and experimental data that revealed that the model underestimated the experimental values for CO and CH_4, while overestimating the values of H_2 and CO_2. However, the observed trends in the changes of gas compositions with different steam-to-biomass ratios aligned with the experimental data.

Minutillo et al. [51] conducted an experiment using a downdraft gasifier operating at a temperature of 1173 K and an air to pellet pine wood ratio of 1.96. The comparison between the model and experimental data showed good agreement overall. However, the experimental values of CH_4 were lower than expected, potentially due to the experimental conditions not reaching chemical equilibrium. As a result, the model predicted higher CH_4 values compared to the experimental data.

Mota et al. [52] tested their experiment using the bubbling fluidized bed reactor that operated at temperature 750 °C with and oxygen carrier to carbon ratio of 1. Figure presents the model prediction of the simulation result and experimental result. The syngas composition prediction from mathematical model is good agreement with experimental data.

Atsonios et al. [53] This study proposed a novel approach to simulate the Calcium Looping (CaL) process using Computational Fluid Dynamics (CFD) and advanced thermodynamic models. They focused on the carbonator and calciner reactors of a pilot-scale Dual Fluidized Bed system. The CFD models were validated against experimental data, showing good agreement for pressure distribution, carbonator capture efficiency, and sorbent regeneration in the calciner. The Two-Fluid-Model (TFM) with advanced EMMS scheme accurately represents the carbonator behavior, including the dense bottom zone. Similar methods are applied to the calciner, revealing CO_2 distribution along the bubbling bed height. However, CO_2 entrapment due to bubbles in the emulsion phase reduces calcination reaction efficiency. Hydrodynamic results inform a kinetics-based process algorithm, emphasizing the importance of dividing the carbonator riser into two sections: a dense solid phase in the bottom zone and a dilute solid concentration in the upper freeboard region. Heat balance calculation shows significant heat flux density difference

between bottom zone and freeboard, suggesting the need for efficient heat removal in scaled-up reactors. A sensitivity analysis optimizes parameters for carbonation-calcination cycle, indicating that effective sorbent regeneration and high looping ratio improve carbonator CO_2 capture efficiency, while low CO_2 concentration in calciner enhances lime regeneration efficiency.

CHAPTER III

METHODLOGY

The contents in this chapter can be divided into two main parts. Section 3.1 describes about a coal/biomass co-gasification integrated with calcium looping carbon dioxide capture process for hydrogen production while Section 3.2 presented the details of a trigeneration process consisting of a proton conducting SOFC and LiBr absorption chiller.

3.1 Co-gasification of biomass and coal integrated with calcium looping carbon dioxide capture process

For hydrogen production through a coal/biomass co-gasification integrated with the calcium looping carbon dioxide capture process, coal and biomass are separately fed into the dryer units to remove moisture from the biomass. Then, the dried biomass and coal are decomposed before entering the gasifier unit. Steam as a gasifying agent which is pre-heated through the heated is supplied to the gasifier unit where it reacts with the mixture of coal and biomass. The gasification process occurs at temperatures above 600°C, facilitating reactions such as pyrolysis, oxidation, and reduction. The primary product is synthesis gas, composed of H_2, CO, CO_2, and CH_4, which is then cooled down in the cooler unit. The lower temperature syngas stream passes through a cyclone to separate ash before being directed to the carbonator unit. In the CO_2 capture process, the main product is $CaCO_3$, along with high purity hydrogen. The streams are separated to extract $CaCO_3$ from hydrogen, and the $CaCO_3$ is then sent to the regenerator unit for CO_2 desorption. The CO_2 is released from the $CaCO_3$ at temperatures above 900°C, while the hydrogen stream with moisture is condensed into liquid form at the condenser unit.

3.1.1 Detail of coal/biomass co-gasification

The assumptions used in the development of model of coal/biomass co-gasification process are listed below.

1. Steady state operation
2. Operated at Isothermal condition
3. No pressure drops in the process
4. Negligible heat loss
5. Reached chemical equilibrium
6. Provided gas product, consisting of H_2, CO, CO_2, CH_4 and H_2O
7. No tar formation

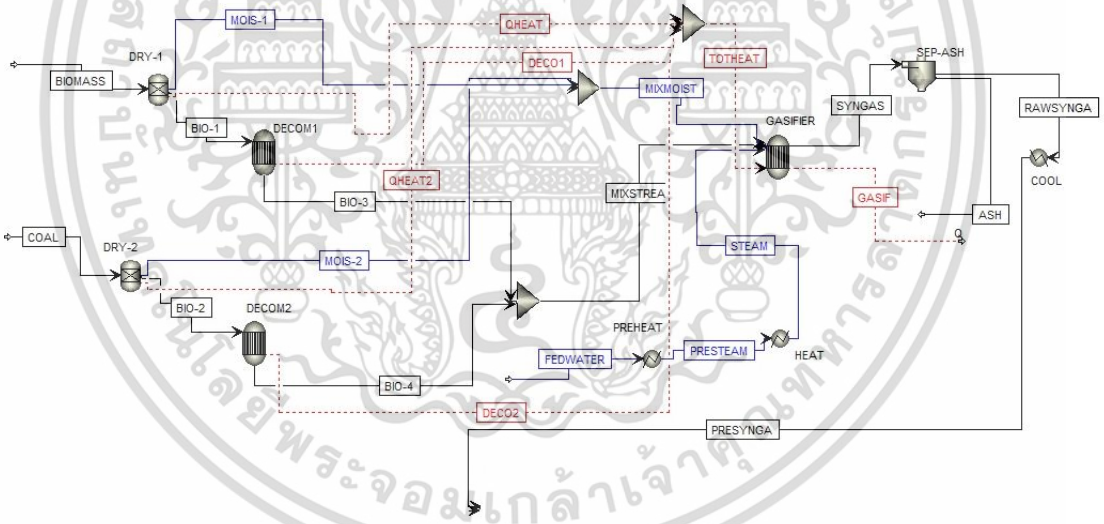

Figure 3.1 Process flow diagram of coal/biomass co-gasification process.

The flowsheet of coal/biomass co-gasification process developed and design in Aspen Plus simulator is shown in Figure 3.1. In this process, two dryers (DRY-1 and DRY-2), that are modeled by the Sep model, is utilized to remove moisture from biomass (BIOMASS stream) and coal (COAL stream) separately. It should be noted that the coal and biomass are fed separately to easily control the ratio of coal and biomass and calculate the conventional component through each decomposition reactor

independently. The dried biomass (BIO-1 stream) and dried coal (BIO-2 stream) are then directed to the decomposition reactors (DECOM1 and DECOM2), represented by the RYield reactor model. As both biomass and coal are non-conventional solid materials, they need to undergo decomposition in the reactor to yield conventional elements such as H_2, CO, CO_2, H_2O, sulfur, and ash. The gas composition is determined by employing ultimate and proximate analysis, written in FORTRAN, within the calculator block. and employing models such as HOCOALGEN and DCOALIGT to estimate the values of Enthalpy and biomass density, respectively. Subsequently, the output from each decomposition reactor is combined—BIO-3 stream for biomass and BIO-4 stream for coal and fed into the gasifier (GASIFIER) along with steam (STEAM). The gasifier, modeled by the RGibbs reactor model, calculates the gas composition at chemical equilibrium by employing the method of minimizing Gibb's free energy. The possible chemical reactions that occurred in the gasification process are listed in Eqs. (3.1)-(3.7). 'SYNGAS' stream as the gas product obtained from gasification is further delivered to a solid-gas separator (SEP-ASH), which is represented by the cyclone model, to remove ash (ASH) from syngas product. As a result, purified syngas (RAWSYNGA) can be provided. Before feeding into the chemical looping process, the purified syngas must be cooled (COOL) and thus, the suitable syngas (PRESYNGA) can be obtained. Table 3.1 shows the description of each module in the gasification process.

Partial oxidation reaction

$$C + O_2 \rightarrow CO_2 \tag{3.1}$$

$$H_2 + 0.5O_2 \rightarrow H_2O \tag{3.2}$$

Boudouard reaction

$$C + CO_2 \leftrightarrow 2CO \tag{3.3}$$

Water gas reaction

$$C + H_2O \leftrightarrow H_2 + CO \tag{3.4}$$

Water gas shift reaction

$$CO + H_2O \leftrightarrow H_2 + CO_2 \quad (3.5)$$

Methane formation

$$C + 2H_2 \rightarrow CH_4 \quad (3.6)$$

Steam methane reforming

$$CH_4 + H_2O \leftrightarrow CO + 3H_2 \quad (3.7)$$

Table 3.1 Description of each module in gasification process

• DECOM1 and DECOM2 (RYield): Heterogenous solid (BIOMASS and COAL) converted to elemental with specifying yield constant in calculator block. Heat released from decomposition reaction and defined as "DECO 1 and DECO 2".
• DRY-1 and DRY-2 (SEP): Moisture in biomass (BIO-1 and BIO-2) sent to separate in DRYER unit and utility energy is "QHEAT and QHEAT2". All outlet streams temperature is 200 °C.
• GASIFER (RGibbs): " BIO-3 and BIO-4" stream sent to react with gasifying agent (STEAM) for gasification reaction at temperature above 700 °C until reaching chemical equilibrium. Moreover, steam or moisture from dryer unit can react to GASIFIER.
• BALANCE (Q-Mixer): This block is used to calculate the energy balance of gasifier unit from all heat flux from all blocks.

3.1.2 Detail of calcium looping carbon dioxide capture process.

The assumptions of calcium looping carbon dioxide capture process used in the development of model are listed below.

1. Steady state operation
2. Operated at isothermal condition
3. No pressure drops in process
4. Negligible heat loss

5. Reached chemical equilibrium
6. Provided gas product, consisting of H_2, CO, CO_2, and H_2O

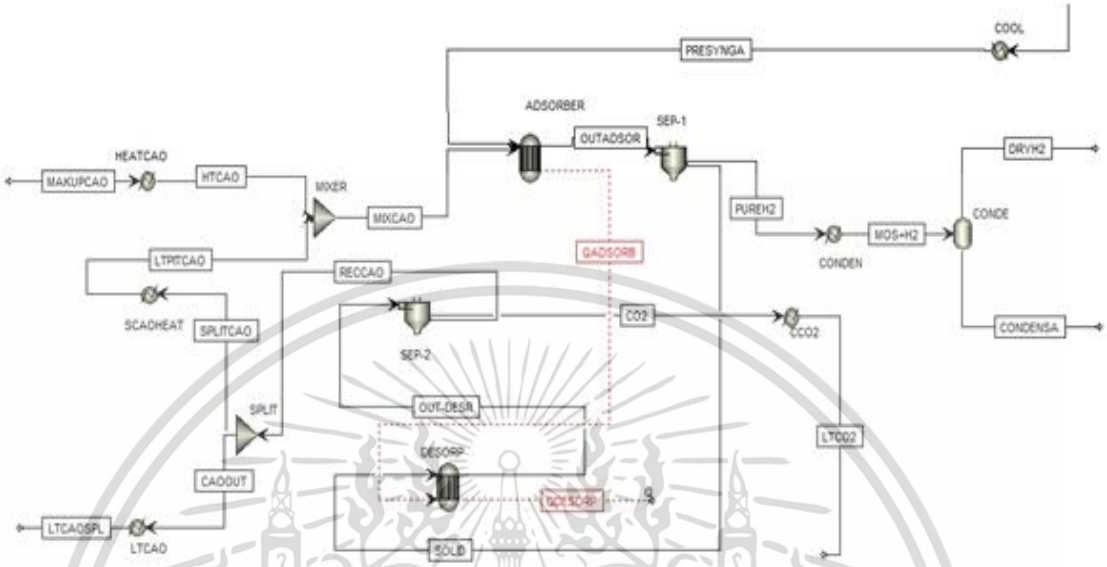

Figure 3.2 Process flow diagram of calcium looping carbon dioxide capture process.

In Figure 3.2, the syngas stream (PRESYNGA stream) is directed to the adsorption unit (ADSORBER) as modelled by RGibbs model, which simulates the carbonator reactor for simultaneous CO_2 capture and water gas shift reaction. In this process, CaO adsorbent (MIXCAO stream: the mixture of fresh CaO and recycled CaO streams) is utilized to adsorb CO_2 through carbonation reaction (Eq. (3.8)) and promote the production of high purity hydrogen by shifting the chemical equilibrium forward. The water gas shift reaction (Eq. (3.5)) further enhances the forward shift of the chemical equilibrium, resulting in high purity hydrogen during the CO_2 capture process. Subsequently, the mixture stream (OUTADSOR) is passed through a cyclone separator (SEP1) to separate the solid and gas components using the split stream principle. The products obtained are a stream of high purity hydrogen and a mixture of solid particles comprising $CaCO_3$, ASH, and CaO, which are recycled back to the desorption unit (DESORP) which is represented by the RGibbs model. DESORP is responsible for regenerating $CaCO_3$ by facilitating the reversible backward shift of the chemical equilibrium of calcination reaction (Eq. (3.9) to CaO and CO_2. The separated cyclone stream yields high purity CO_2 and CaO, with CaO being purged from the process at a

rate of 1%. Table 3.2 shows descriptions of each model in calcium looping carbon dioxide capture process.

Carbonation reaction

$$CaO + CO_2 \rightarrow CaCO_3 \quad (3.8)$$

Calcination reaction

$$CaCO_3 \rightarrow CaO + CO_2 \quad (3.9)$$

Table 3.2 Description of each module in calcium looping carbon dioxide capture process.

• ADSORBER (RGibbs): This reactor is set up in minimum Gibbs free energy of chemical equilibrium condition and operates at operating temperature 400 – 650 °C. CaO reacts with CO_2 in this unit and form to be $CaCO_3$. Mixture gas and $CaCO_3$ are sent to separate in cyclone unit.
• SEP-1 and SEP-2 (SSplit): These units split mixture stream to be solid and gas stream in unit operation.
• DESORP (RGibbs): In this block, it assumes to be minimum Gibbs free energy of chemical equilibrium condition and operate at temperature 900 °C. $CaCO_3$ sent to heater and desorb CO_2 at calciner reactor.

Table 3.3 Proximate analysis, ultimate analysis and lower heating values of rice husk [50] , pellet pine wood [51] and lignite coal [52]

Fuel type	Proximate analysis (wt.%)				Ultimate analysis (wt.%)					LHV (kJ/g)
	FC	VM	MC	Ash	C	H	N	O	S	
Rice husk [50]	18.68	56.46	12.20	19.52	39.44	3.22	0.08	37.74	0.01	13.52
Pine wood [51]	16.50	83.30	10.00	0.20	50.50	5.90	0.30	43.00	0.20	17.30
Lignite coal [52]	33.60	28.82	31.20	6.38	47.83	6.67	0.52	37.95	0.65	19.29

*Noted: FC = Fixed Carbon, VM = Volatile Matter, MC = Moisture Content

3.1.3 Details of coal/biomass co-gasification integrated calcium looping carbon dioxide capture process.

Figure 3.3 demonstrates a diagram of a coal/biomass co-gasification integrated with calcium looping process. The diagram depicts material streams with black lines, energy streams with red dash lines, and water/steam streams with blue lines. The chosen raw material for hydrogen production is a mixture of pellet pine wood and lignite coal. Table 3.3 shows proximate and ultimate analysis of pellet pine wood and lignite coal. The process consists of two main sections: gasification and the purification of hydrogen using the calcium looping process, as described in Sections 3.1.1 and 3.1.2, respectively. Table 3.4 shows the description of each module in biomass and coal integrated with calcium looping carbon dioxide capture process. In addition, Table 3.5 lists input parameters of each stream and unit operation used at reference condition in the simulation.

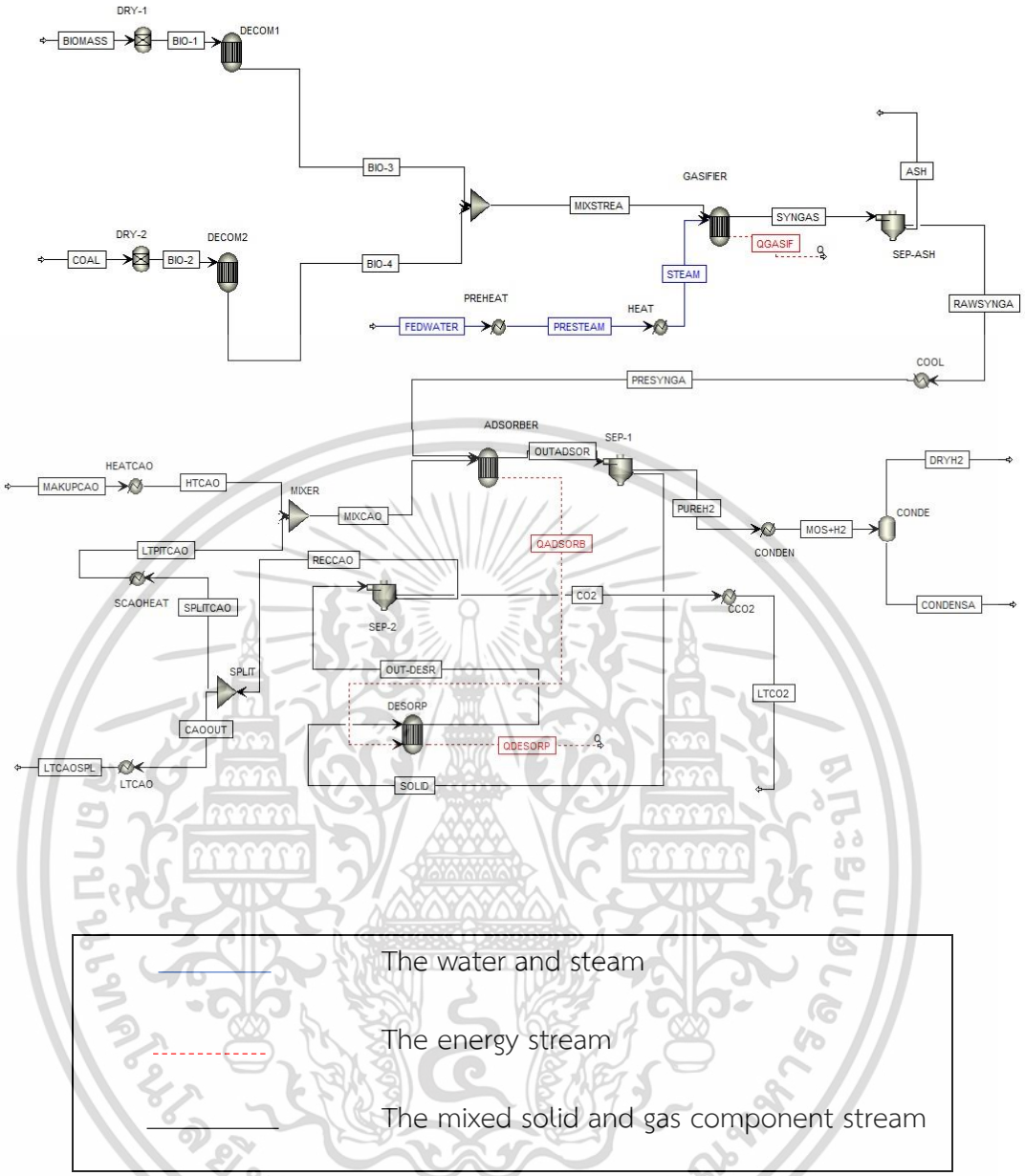

Figure 3.3 The schematic process flow diagram of co-gasification of biomass and coal integrated with calcium looping carbon dioxide capture process.

Table 3.4 Description of each module in coal/biomass co-gasification integrated with calcium looping carbon dioxide capture process.

Name of unit operation	Type of model	Description
DRY-1	SEP	The phase separator uses to split moisture from biomass.
DRY-2		The phase separator uses to split moisture from coal.
DECOM1	RYield	Yield reactor will decompose biomass to elements. This model reactor is suitable with available product yield.
DECOM2		Yield reactor will decompose coal to elements. This model reactor is suitable with available product yield
GASIFIER	RGibbs	The chemical equilibrium reactor is used to calculate the gas composition through the minimization of Gibbs free energy.
ABSORP		The chemical equilibrium reactor occurs the carbonation.
DESORP		The chemical equilibrium reactor occurs the calcination reaction
SEP-ASH	SSplit	This unit can specify value for perfect separation mixture stream to two streams or more. In this work, it uses to be cyclone separator for ash and raw syngas from gasifier unit.
SEP-1		This unit can specify value for perfect separation mixture stream to two streams or more. In this work, it uses to be cyclone separator for calcium carbonate and purified hydrogen from adsorber unit.
SEP-2		This unit can specify value for perfect separation mixture stream to two streams or more. In this work, it uses to be cyclone separator for calcium oxide and carbon dioxide from desorber unit.

Table 3.5 Input parameters of each stream and unit operation used at reference condition in the simulation.

Parameters	Value
Atmospheric condition (atm)	1
Biomass flow rate (kg/hr)	1000
Coal flow rate (kg/hr)	1000
Coal : Biomass	1:1
Steam flow rate (kg/hr)	2000
Steam Temperature (°C)	800
Calcium oxidie (kg/hr)	2000
Gasifier temperature (°C)	700
Carbonator temperature (°C)	450
Regenerator temperature (°C)	950

3.1.4 Model validation of co-gasification of biomass and coal and calcium looping carbon dioxide capture process

In this study, the simulated results of coal/biomass co-gasification integrated with calcium looping carbon dioxide capture process are validated with experimental data to ensure that the proposed model can provide the adequate results. However, there is no experiment reported on the integrated process of coal/biomass co-gasification integrated with calcium looping carbon dioxide capture process, the model validations of gasification and carbon dioxide capture process are performed separately. Table 3.6 summarizes the details of each literature used in the model validation.

For the coal/biomass co-gasification process, there are three publications used for model validation as follows:

(1) Loha et al. [50] set up the experiment set up to investigate the conversion of rice husk into syngas. Their experiments were conducted using a fluidized bed gasifier. Rice husk, with proximate and ultimate analysis data presented in Table 3.3,

was fed into the gasifier at a rate of 1 kg/hr. The gasification process was carried out at a temperature of 750 °C and pressure 1.05 bar.

(2) Minutillo et al. [51] done experiment in downdraft gasifier at temperature 1173 K and air to pellet pine wood ratio of 1.96.

(3) Mota et al. [52] performed the experiment of coal gasification process. In their experiment, the bubbling fluidized bed reactor was operated at a temperature of 750 °C with and oxygen carrier to carbon ratio of 1.

For the CO_2 capture process, the simulated results are compared with the experimental results of Atsonios et al. [53].

Table 3.6 Details, in terms of experiment set up, operating condition and reactor configuration, of each publication used in the model validation.

Configurations	Reactor	biomass/ adsorbent	Operating condition	Reference
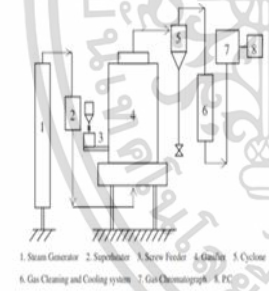	Fluidized bed biomass gasifier	Rice husk	Gasification temperature = 750 °C, Steam to biomass = 0.75 – 2.0	[50]
	Down draft gasifier	Pellet pine wood	Temperature = 1173 K, Air to biomass mass ratio = 1.96	[51]

Table 3.6 Details, in terms of experiment set up, operating condition and reactor configuration, of each publication used in the model validation. (Continue)

	Bubbling bed gasifier	Lignite coal	Temperature = 1023 K, Oxygen to coal ratio = 0.8-1.6	[52].
	Circulating fluidized bed reactor	Calcium oxide	Carbonator and Calciner temperature = 650 °C and 900 °C	[53]

3.1.5 Study on coal/biomass co-gasification integrated with calcium looping carbon dioxide capture process

In coal/biomass co-gasification integrated with calcium looping carbon dioxide capture process, there are many operating parameters that affect hydrogen production. The parameters considered in this study are listed below:

- Gasifier temperature is the operating temperature of gasifier unit that run at high temperature in a range of 500 – 1,000 °C [50, 52] because gasification reaction is exothermic reaction and reversible chemical equilibrium reaction.
- Steam to feed (S/F) mass ratio is an important parameter in steam gasification process. It is noted that feed considered in this work is the summation of coal and biomass. The expression of S/F mass ratio is shown in Eq. (3.10). In this work, S/F mass ratios are adjusted in a range of 1 – 10.

$$\frac{\mathrm{S}}{\mathrm{F}} = \frac{\dot{m}_{\mathrm{steam}}}{\dot{m}_{\mathrm{biomass}} + \dot{m}_{\mathrm{coal}}} \qquad (3.10)$$

- CaO to feed (CaO/F) mass ratio which is a significant factor on CO_2 capture process can be expressed in Eq. (3.11). This work focuses on the value of CaO/F between 1 and 6.

$$\frac{\mathrm{CaO}}{\mathrm{F}} = \frac{\dot{m}_{\mathrm{CaO}}}{\dot{m}_{\mathrm{biomass}} + \dot{m}_{\mathrm{coal}}} \quad (3.11)$$

- Carbonator temperature is the operating temperature of a carbonator reactor. This unit operation is used to capture CO_2 in syngas. From the literature survey, the carbonator temperature is in a of range 400 – 1,000 °C.
- Calciner temperature is the operating temperature of regenerator reactor. $CaCO_3$ formed through carbonator reaction can convert back to CaO in a regenerator reactor. The desorption process is an endothermic reaction which can be operated in a range of 400 – 1,400 °C.

3.1.6 Design experiment and analysis of variance for process optimization in the integrated co-gasification of biomass and coal and calcium looping carbon dioxide capture process

Factorial designs are commonly employed in experiments where multiple factors need to be examined together to understand their combined effects on a response variable. The 2^k factorial design is valuable in initial experimental stages with numerous factors [44]. In this study, a 2^2 factorial design is utilized to analyze the main effects and interactions of parameters associated with the H_2 mole fraction in the gasification process and the CO_2 capture efficiency in the calcium looping process, which consists of two sections. The first section focuses on optimization of the co-gasification process, with three parameters: gasification temperature (A), S/F mass ratio (B), and coal/biomass (C/B) mass ratio. Each parameter is investigated at two levels, as shown in Table 3.7. Since this work focused on co-gasification of coal and biomass, the optimal ratio of coal and biomass mixed in feed should be determined. C/B mass ratio can be represented as Eq. (3.12).

$$\frac{\mathrm{C}}{\mathrm{B}} = \frac{\dot{m}_{\mathrm{coal}}}{\dot{m}_{\mathrm{biomass}}} \quad (3.12)$$

Table 3.7 2^3 factorial experimental design analysis of co-gasification biomass and coal with Aspen Plus V10

Run	Gasification temperature (°C) (A)	S/F mass ratio (-) (B)	C/B mass ratio (-) (C)
1	-	-	-
2	-	-	+
3	-	+	-
4	+	-	+
5	+	+	+
6	+	-	-
7	-	+	+
8	+	+	-

In the second section focused on carbon dioxide capture process, there are two levels of following parameters: carbonator temperature (D) and CaO/F mass ratio (E) were investigated. Table 3.8 shows the experimental design analysis of carbon dioxide capture process.

Table 3.8 2^2 factorial experimental design analysis of carbon dioxide capture process with Aspen Plus V10

Run	Carbonator temperature (°C) (D)	CaO/F mass ratio (-) (E)
1	+	-
2	-	+
3	+	+
4	-	-

3.1.7 Energy analysis of coal/biomass co-gasification integrated with calcium looping carbon dioxide capture process

In thermal efficiency analysis method, it needs to calculate heat and mass balance before step analyze thermodynamic efficiency of co-gasification of biomass and coal integrated with calcium looping carbon dioxide capture process. Thermal efficiency can calculate the energy output of hydrogen to total energy input from heat utility in all reactors as Eq. (3.13).

$$\eta_{H_2}(\%) = \frac{m_{H_2} \times LHV_{H_2}}{m_{biomass} \times LHV_{biomass} + m_{coal} \times LHV_{coal} + \dot{m}_{steam} h_{steam}} \times 100 \qquad (3.13)$$

where m_{H_2}, $m_{biomass}$, m_{coal} and $\dot{m}_{steam}$ are mass flow rate of hydrogen, biomass, coal and steam. LHV_{H_2}, $LHV_{biomass}$, and LHV_{coal} are lower heating value of hydrogen, biomass, and coal, respectively. It is noted that h_{steam} refers to specific enthalpy of steam at 800 °C (= 3,663.84 kJ/kg).

3.2 Trigeneration process consisting of SOFC-H^+ and LiBr absorption chiller

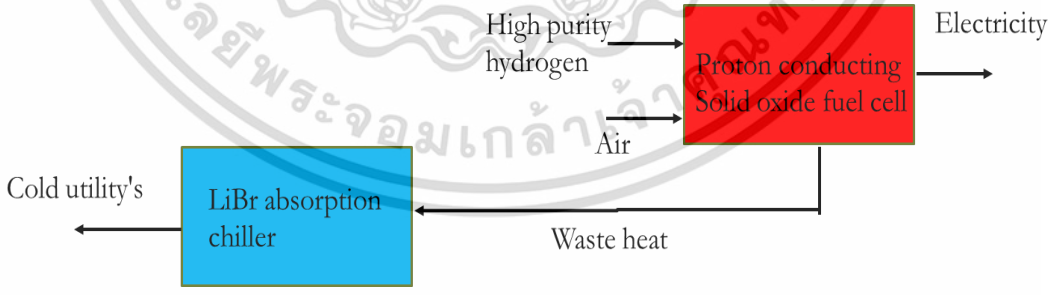

Figure 3.4 Block flow diagram of trigeneration process consisting of SOFC-H^+ and LiBr absorption chiller.

Figure 3.4 shows the diagram of trigeneration process consisting of SOFC-H^+ and a LiBr absorption chiller to generate power, heat, and cooling. The process begins by

supplying pure hydrogen and air at atmospheric conditions to compressor and preheater for providing the streams at desired temperature and pressure. Within the SOFC-H^+, electrochemical reactions take place and thus, steam, high-temperature gas (exhaust), and electricity are produced. The exhaust stream passes through a heat exchanger for heat recovery and preheating of the incoming stream. The enthalpy in the exhaust stream is utilized to generate hot water for the thermal-driven absorption chiller unit. The working fluid in the process is a weak LiBr solution from the absorber, which is pumped to recover heat in the solution heat exchanger unit. The mixture then undergoes separation of vapor and high-concentration solution at the flash vessel. The vapor refrigerant and high-concentration solution are separated and recycled within the process cycle. The vapor refrigerant flows through the condenser unit, where it condenses back into high-pressure liquid refrigerant. The liquid refrigerant expands through an expansion valve, transforming into low-pressure liquid refrigerant. The low-pressure saturated liquid refrigerant enters the evaporator, where it evaporates into vapor. The high-concentration LiBr solution is recycled back to the solution heat exchanger, transferring energy to the cold heat exchanger. The vapor refrigerants are then mixed with the LiBr weak solution at the absorber unit, completing the closed-loop thermodynamic cycle.

3.2.1 Detail model of SOFC-H^+

The assumptions of SOFC-H^+ operation used in the development of model are listed below.

1. Steady state operation
2. Operated at isothermal condition
3. No pressure drops in process
4. Negligible heat loss
5. Used Peng-Robinson property model in the simulation

Figure 3.5 illustrates schematic diagram of the SOFC-H^+ developed and designed through Aspen Plus V10. The PUREH2 stream is introduced to the anode

(ANODE) in which a Sep model is used. Subsequently, the PUREH2 stream is divided into two streams: FEEDHYD and SPLITH2. The molar flow rate of H_2 in the FEEDHYD stream (H_2^i) must be known to determine the molar flow rate of hydrogen used in the electrochemical reaction ($\dot{n}_{H_{2,ele}}$) which is related to the fuel utilization (U_f) as expressed in Eq. (3.14). On the other hand, $\dot{n}_{H_{2,ele}}$ can be determined when the molar flow rate of O_2 fed into the SOFC (O_2^i) is given as Eq. (3.15).

$$\dot{n}_{H_{2,ele}} = U_f(H_2^i) \tag{3.14}$$

$$\dot{n}_{H_{2,ele}} = 2U_f(O_2^i) \tag{3.15}$$

Both equations are written in the context of a calculator block executed at the anode side (Sep model) to define the amount of hydrogen used in the electrochemical reaction. Then , the current density (j), which represents the current (I) divided by the cell area (A), can be calculated from the fuel utilization or the molar flow rate of hydrogen consumed in the electrochemical reaction, as shown in Eq. (3.16)

$$j = \frac{I}{A} = 2\frac{U_f(H_2^i)F}{A} = 2\frac{\dot{n}_{H_{2,ele}}F}{A} \tag{3.16}$$

The FEEDHYD stream then enters a compressor and passes through two heater exchangers to increase its pressure and temperature. The resulting stream, known as FEDH2P, is directed to the cathode side of the SOFC-H^+ unit (CATHODE). Simultaneously, the PREAIR stream undergoes compression and heating through a compressor and two heat exchangers before being supplied to the cathode side. At the cathode side, the electrochemical reaction between H_2 and O_2 takes place to generate power and exhaust gas (EX-CATH). To assess the electrical performance, appropriate calculations are performed, the electrochemical model of SOFC-H^+ proposed in Section 2.8, it is written in the calculator block implemented in Aspen Plus simulator. Table 3.9 shows the description of each model in SOFC-H^+ while the cell dimension, material properties and operating condition used in the simulation of SOFC-H^+ are listed in Table 3. 10.

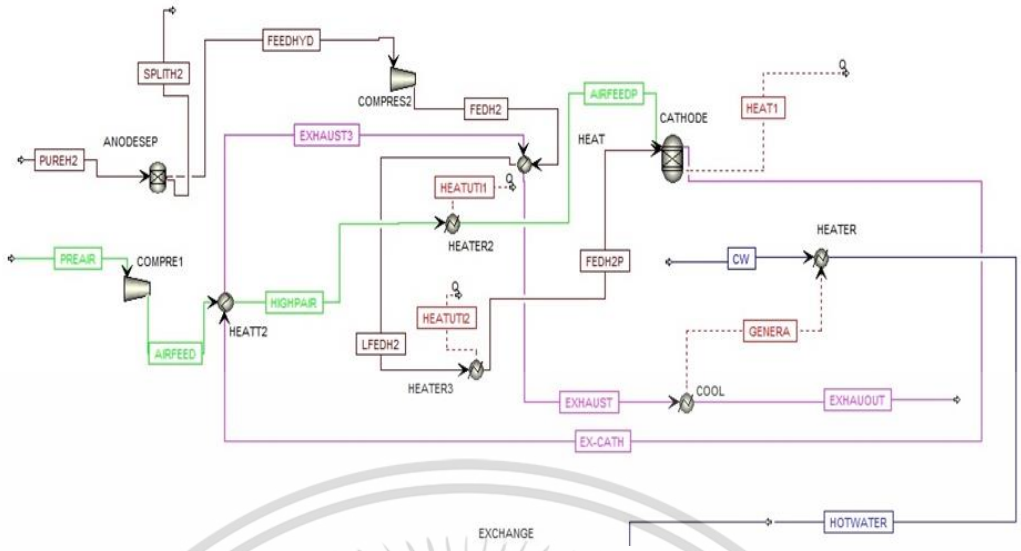

Figure 3.5 Schematic diagram of the SOFC-H^+ implemented by Aspen Plus V10.

Table 3.9 Description of each model in SOFC-H^+

• ANODESEP (Sep): This unit use to split hydrogen component in PUREH2 stream to SPLITH2 and FEEDH2 by specify fuel utilization factor. The equation was written in calculator block.
• CATHODE (RGibbs): This block assumes to be minimum Gibbs free energy at chemical and set up to occur electrochemical reaction in this unit.

Table 3.10 The cell dimension, material properties and operating condition used in the simulation

Parameters	Value
Operating conditions of SOFC-H^+	
Active area of cell (m^2)	0.04142
Number of cells	1,000
Operating temperature (°C)	550
Operating pressure (bar)	1
Fuel utilization factor	0.8
Anode stream inlet composition	97% H_2, 3% H_2O
Cathode stream inlet composition	79% N_2, 21% O_2
Anode	
Anode thickness (μm)	550
Porosity	0.3
Pre-exponential for H_2 oxidation (A/m^2) [54]	8.817×10^9
Activation energy (J/mol) [55]	1.2×10^5
Anode diffusion coefficient (m^2/s) [56]	8.98×10^{-5}
Cathode	
Cathode thickness (μm)	40
Porosity	0.3
Pre-exponential for O_2 oxidation (A/m^2) [54]	9.57×10^8
Activation energy (J/mol) [55]	1.0×10^5
Cathode diffusion coefficient (m^2/s) [56]	6.31×10^{-6}

Parameters	Value
Operating conditions of SOFC-H$^+$	
Active area of cell (m^2)	0.04142
Number of cells	1,000
Operating temperature (°C)	550
Operating pressure (bar)	1
Fuel utilization factor	0.8
Anode stream inlet composition	97% H_2, 3% H_2O
Cathode stream inlet composition	79% N_2, 21% O_2
Electrolyte	
Electrolyte thickness (μm)	15
Pre-factor of proton conductivity ($S{\cdot}m^{-1}{}^{o}C$) [54]	2.5719×10^4
Activation energy for proton carrier (eV) [54]	0.38

3.2.2 Detail model of LiBr absorption chiller

The assumptions of single stage LiBr absorption chiller used in the simulation are shown below:

1. The process is steady state operation.
2. The process is isothermal condition.
3. The fluid thermodynamic property is based on ELECNRTL property method.
4. There is no pressure drops in the process.

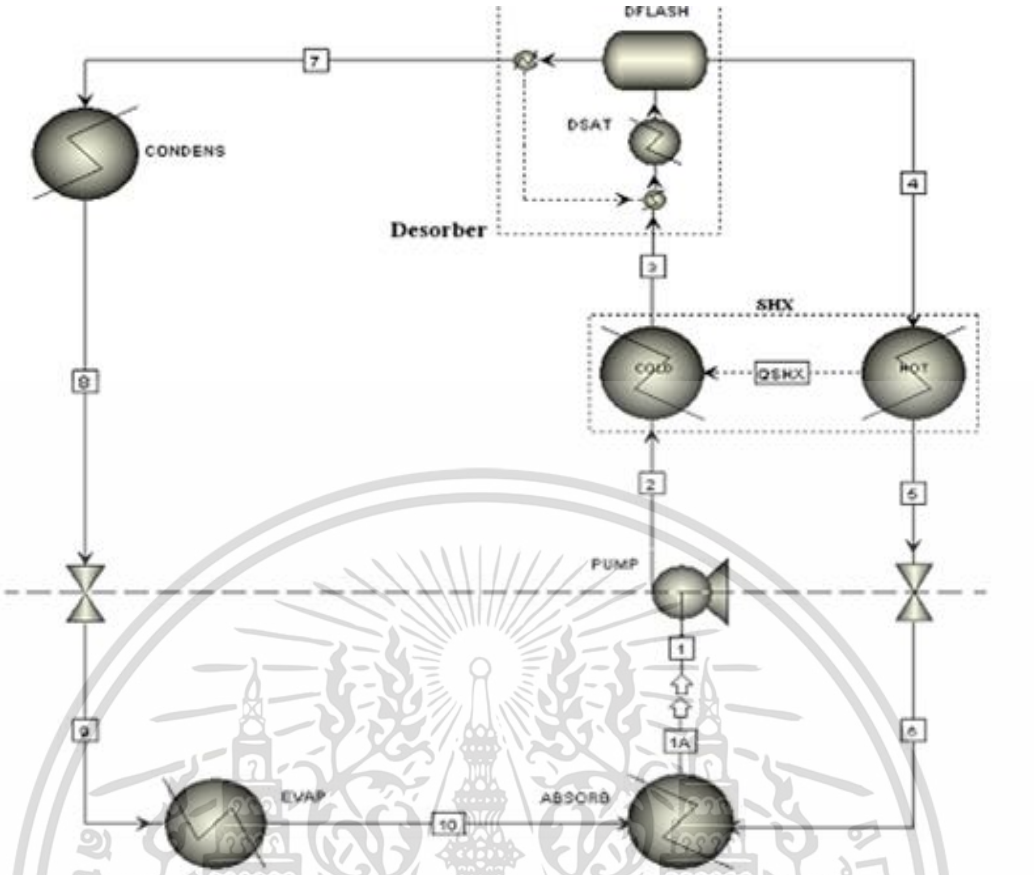

Figure 3.6 Schematic diagram of the LiBr absorption chiller implemented by Aspen Plus V10.

As schematic diagram shown in Figure 3.6, the LiBr absorption chiller employs LiBr as the absorbent and water as the refrigerant. The key components of the system include the generator, absorber, condenser, evaporator, solution heat exchanger, expansion valve, and pumps. Waste heat is supplied to the generator, which separates the vapor refrigerant and liquid solution. The vapor refrigerant is directed to the condenser, where it releases heat to the ambient heat sink. The liquid refrigerant passes through the expansion valve, causing partial vaporization in the evaporator unit. The solution flows to the absorber, where it rejects heat. A solution heat exchanger is incorporated between the generator, pump, and expansion valve to increase the temperature from state 2 to state 3. The desorber, represented by a module in ASPEN PLUS, functions to change pressure, heat, and mix components. Its main purpose is to separate the vapor of the refrigerant and absorbent from state 3 to state 4 and state 7. The saturated vapor of the refrigerant from state 7 then proceeds to the condenser,

where heat is removed, and the vapor condenses into the liquid phase (state 8). The low-pressure saturated liquid refrigerant passes through an expansion valve, reducing the pressure from state 8 to state 9. The low-pressure saturated liquid refrigerant enters the evaporator and fully evaporates into vapor (state 10). The high concentration of LiBr is recycled back to the solution heat exchanger, transferring energy to the cold heat exchanger from state 4 to state 5. The concentrated LiBr solution undergoes expansion through an expansion valve from state 5 to state 6. Finally, the low concentration LiBr solution from state 6 mixes with the refrigerant from state 10 in the absorber. The state assumption of each point was specified as Table 3.11. and Table 3.12 shows the description of each model in LiBr absorption chiller.

Table 3.11 State assumption of single effect LiBr absorption chiller

State point	Assumption
1	Vapor fraction is 0
2	Determined by pump
3	Determined by solution heat exchanger
4 and 7	Saturated liquid and Saturated vapor; the mass flow rate ratio at point 4 and 7 is determined by temperature and waste heat
5	Determined by solution heat exchanger
6	Determined by expansion valve model
8	Vapor fraction is 0
9	Determined by expansion valve model

Table 3.12 Description of each module in LiBr absorption chiller

ABSORB (Heater): The absorber was modeled as a heater block with two inlets, the exit of the evaporator and the exit of the solution valve. Vapor quality at the absorber exit is assumed to be saturated liquid.
PUMP: Pumps are used between states 1 and 2 and boost to high pressure.
DESORPBER (Flash2): The modeling of components has been relatively straightforward, as they all involved simple processes such as pressure changes, heat addition or rejection, mixing, or a combi nation of those.
EVAP (Heater): Modeling the evaporators is similar to modeling the condensers. The inputs to the model were a vapor quality of one at the exit.
CONDENS (Heater): The condensers were modeled as heater blocks, which introduces a new assumption, that heat is being added at constant temperature. The only user-input necessary is a vapor quality of zero at the exit.
VALVE: The other pressure changes devices that require to be modeled the cycle are valves.
HOT (Heater) A solution heat exchanger (SHX) is used once in the single effect and exchange heat between Weak LiBr solution and low temperature and Strong LiBr solution and high temperature.
COLD (Heater) A solution heat exchanger (SHX) is used once in the single effect and exchange heat between Weak LiBr solution and low temperature and Strong LiBr solution and high temperature.

3.2.3 Detail model of trigeneration process consisting of SOFC-H^+ and LiBr absorption chiller

The details of each process that include SOFC-H^+ and LiBr absorption chiller are described in Sections 3.2.1 and 3.2.2. After the electrochemical reaction

accomplishes in the SOFC-H^+, the high-temperature EX-CATH stream is further utilized in two heat exchangers to increase the temperature of the AIRFEED and FEDH2 streams, while a cooler is employed to recover waste heat for the driving of the absorption chiller. The EXHAUST stream is cooled to ambient temperature. Lastly, the waste heat in the GENERA stream is directed to the generator in the LiBr absorption chiller unit. In the LiBr absorption chiller, the LiBr solution is used as the solution while water is used as the refrigerant. A heat source provided for the absorption chiller is HOTWATER and WASTEHEAT stream are utilized as heat sources for the absorption chiller process. The generator unit (DESORBER) receives the waste heat from the SOFC-H^+ unit and the LIBRSOL3 stream. There are two streams; REFRIG and LIBRSTRO emerged from the DESORBER. The REFRIG stream is sent to the condenser unit (CONDEN) for condensing and removing heat.

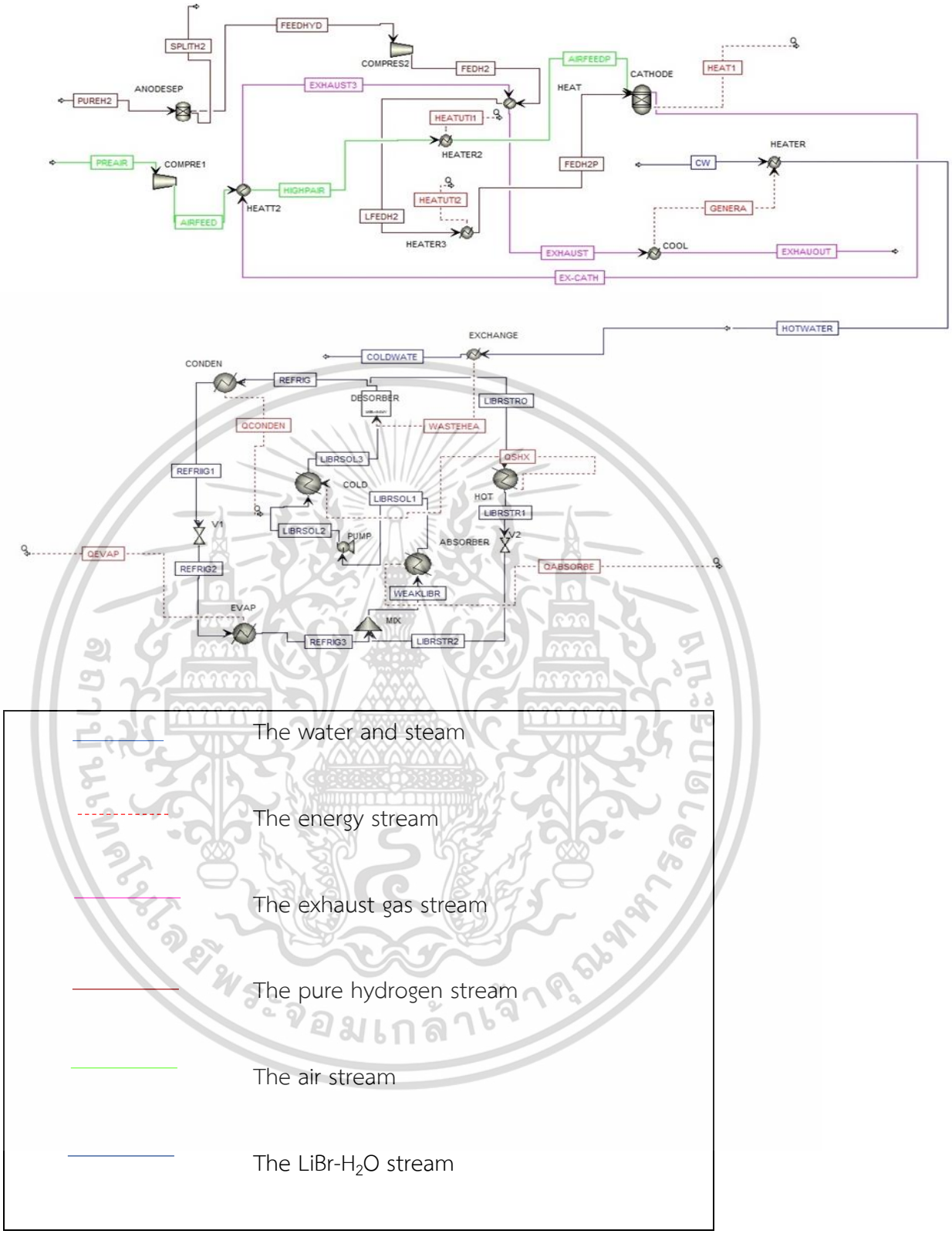

Figure 3.7 Schematic diagram of the trigeneration based on the SOFC^{+}H and LiBr absorption chiller implemented by Aspen Plus V10.

In case of the LIBRSTRO stream as a rich liquid solution, it goes back to exchange heat at the heat exchanger (HOT) and flows through the expansion valve (V2). The LIBRSTR2 stream as a strong LiBr solution, is mixed with the REFRIG3 stream (water) at the absorber unit (ABSORBER). The LIBRSOL1 stream (diluted LiBr solution) is pumped and calculated by specifying the outlet pressure and pump efficiency. Subsequently, the LIBRSOL2 stream is delivered to the heat exchanger (COLD) to increase temperature, following which the high-temperature weak solution, the LIBRSOL3 stream, is provided. At the exit of the condenser unit, the REFRIG1 stream, which is a saturated liquid refrigerant, is sent to the expansion valve (V1) to reduce pressure, as well as its temperature. The REFRIG2 stream (low-pressure saturated liquid refrigerant) enters the evaporator, and then, the saturated vapor, as the REFRIG3 stream, is obtained. This cycle constitutes the VARS.

3.2.4 Model validation of SOFC-H^+ and LiBr absorption chiller

Since no previous publications reported on a trigeneration process, consisting of SOFC-H^+ and LiBr absorption chiller, the model validations of both units are performed separately.

In this work, the simulation result obtained from the SOFC-H^+ model is validated with the experiment result of Zhang et al. [54] and Lei et al. [63]. The first researcher studied the SOFC-H^+, operating in the temperature range of 550 to 700 ^{o}C. The SOFC-H^+ is fabricated with thicknesses of anode, cathode and electrolyte as 550, 40 and 15 μm. For the second, they used the SOFC-H^+ that has the thicknesses of electrode and electrolyte as 0.33 mm and 15 μm. In their work, the operating condition of SOFC-H^+ is at 650 ^{o}C and 1 bar.

The validation of the LiBr absorption chiller model developed in Aspen Plus has already been proposed in Somers et al. [45]. In their research, the simulation result obtained from Aspen Plus is validated with the Engineering Equation Solver (EES) model of Herold et al. [57]. EES database is referred from ASHARE Handbook (HVAC application heating ventilating and air-conditioning applications) [55]. It is noted that the EES model is more detailed than the experiment.

3.2.5 Study on trigeneration process consisting of SOFC-H^+ and LiBr absorption chiller

This work performs the sensitivity analysis to investigate the effect of operating condition in SOFC-H^+ and LiBr absorption chiller on system efficiency. From literature review, the parameters of SOFC-H^+ are operating temperature, and pressure, fuel utilization factor and air to fuel ratio. The parameters of LiBr absorption chiller are temperature of condenser, generator, evaporator and hot water mass flowrate and temperature. The response parameters of SOFC-H^+ and LiBr absorption chiller are electrical efficiency, thermal efficiency, and COP respectively.

Details of operational range used in the sensitivity analysis are shown below:

- SOFC-H^+ operating temperature is the main important parameter that affects to system performance. Since the open-circuit voltage and all voltage losses are influenced by temperature. The operating temperature of SOFC-H^+ is considered in the range of 550 – 750 °C.
- SOFC-H^+ operating pressure is another parameter that affect to open-circuit voltage and voltage loss. In this work, the operating pressure of SOFC-H^+ varies from 1 to 10 bar.
- Fuel utilization factor defines the fuel consumption to provide electricity. In this work, the fuel utilization factor is adjusted from 0.8 to 0.95.
- Air to fuel molar ratio is inlet molar flow rate of air stream to inlet molar flow rate of fuel stream that is calculated based on stoichiometry and it affects on heating value of exhaust gas. Moreover, this parameter is significant on absorption chiller performance. In this work, the air to fuel molar ratio is investigated between 1 and 6.
- Hot water mass flow rate in generator unit influences absorption chiller performance in terms of coefficient of performance (COP). Since it is a heat source for thermal driven process. In this work, hot water mass flow rate is studied between 0.1 and 2 kg/sec.
- The importance of hot water temperature in generator unit is similar to hot water mass flow rate. In this work, the operational range of hot water temperature is 80 – 125 °C.

- Generator temperature has an impact on LiBr concentration solution which drives the thermodynamic cycles. Additionally, difference LiBr concentration can increase cooling duty in system. The generator temperature varies in a range of 90 – 110 °C.
- Evaporator temperature influences LiBr concentration solution. Difference concentration between flash separator and absorber unit can increase COP. The range of evaporator temperature used in this work is 1 – 10 °C.

3.2.6 Design experiment and analysis of variance for process optimization for maximization electricity , overall efficiency and COP

In this section, the effects of operating conditions in SOFC-H^+ and LiBr absorption chiller on all performances are studied based on a method of DOE. Since this work focuses on the integrated system of SOFC-H^+ and LiBr absorption chiller, DOE is separately performed.

The parameters selected to perform the optimization of the SOFC-H^+ performance are (A) A/F molar ratio and (B) operating pressure. The full factorial design of 2 factors with 2 levels can provide 4 experimental runs as listed in Table 3.13.

Table 3.13 2^3 factorial experimental design analysis of the SOFC-H^+ with Aspen Plus V10

Run	Air to fuel mole ratio (-) [A]	Operating Pressure (bar) [B]
1	2	10
2	2.33	1
3	2.33	10
4	2	1

For the LiBr absorption chiller, the process parameters as (D) evaporator temperature (E) generator temperature (F) hot water mass flow rate and (G) hot water

temperature inlet are selected. The full factorial design of 4 factors with 2 levels leads to 16 experimental runs with a single replicate as shown in Table 3.14.

Table 3.14 2^3 factorial experimental design analysis of the LiBr absorption chiller with Aspen Plus V10

Run	Generator temperature (°C) [D]	Evaporator temperature (°C) [E]	Hot water mass flowrate (kg/sec) [F]	Inlet hot temperature (°C) [G]
1	90	1	0.04	100
2	100	10	0.01	90

Table 3.14 2^3 factorial experimental design analysis of the LiBr absorption chiller with Aspen Plus V10 (Continue)

Run	Generator temperature (°C) [D]	Evaporator temperature (°C) [E]	Hot water mass flowrate (kg/sec) [F]	Inlet hot temperature (°C) [G]
3	90	10	0.04	100
4	100	10	0.04	100
5	90	1	0.01	90
6	100	1	0.01	90
7	90	1	0.01	100
8	100	1	0.04	90
9	100	10	0.04	90
10	90	1	0.04	90
11	90	10	0.01	90
12	90	10	0.01	100
13	90	10	0.04	90
14	100	10	0.01	100
15	100	1	0.04	100
16	100	1	0.01	100

3.2.7 Energy and analysis of trigeneration process consisting of SOFC-H^+ and LiBr absorption chiller

Energy and exergy analysis are employed to evaluate the overall performance of the system, while thermal analysis demonstrates that the process does not require the use of hot and cold utilities. By deriving the general mass and energy equations of the process, the thermal efficiency, which represents the ratio of energy output to energy input, can be determined. This expression can be used to evaluate the overall efficiency of SOFC-H^+ and calculate from Eq. (3.17).

$$\eta_{overall} = \frac{P_{SOFC} + Q_{waste\ heat} - W_{COMP_1} - W_{COMP_2}}{\left(\dot{n}_{H_2} \times LHV_{H_2}\right)_{anode,in}} \tag{3.17}$$

The electrical efficiency can calculate based on Eq. (3.18)

$$\eta_{electrical} = \frac{P_{SOFC} - W_{COMP_1} - W_{COMP_2}}{\left(\dot{n}_{H_2} \times LHV_{H_2}\right)_{anode,in}} \tag{3.18}$$

where P_{SOFC} = Power density (W/m^2)

W_{COMP} = Compressor consumption (kW)

$Q_{\mathrm{waste\ heat}}$ = Waste heat recovery from process (kW)

$\dot{n}_{\mathrm{H_2}}$ = Molar flow rate of hydrogen (kmol/hr)

$LHV_{\mathrm{H_2}}$ = Lower heating value of hydrogen (kJ/kg)

For the absorption cycle, coefficient of performance (COP) is defined as cooling capacity or useful effect to heat input. In the trigeneration process, it is the ratio of heat duty of evaporator to enthalpy of hot water as Eq. (3.19).

$$COP = \frac{Cooling\ capacity}{Waste\ heat\ input} = \frac{Q_{evap}}{Q_{waste\ heat}} \tag{3.19}$$

where Q_{evap} = Heat required for the evaporator (kW)

Exergy analysis serves as a technique to assess the effectiveness of energy conversion, offering insights beyond what can be obtained through energy analysis

alone. While energy analysis focuses on calculating system efficiency based on the first law of thermodynamics, exergy analysis considers the second law of thermodynamics. In the context of the trigeneration system utilizing SOFC-H^+ and LiBr absorption chiller, the analysis assumes steady-state and isothermal conditions.

The input exergy of SOFC-H^+ which is modified from Gwak et al. [33] can be calculated as Eq (3.20).

$$Ex_{in,SOFC} = Ex_{in,fuel} + Ex_{in,Air} \tag{3.20}$$

From exergy balance, the exergy efficiency of the combined heat and power of SOFC-H^+ can be rearranged as output to input Eq. (3.21).[59]

$$\varepsilon_{CHP} = \frac{W_{net,SOFC-H^+} - W_{COMP_1} - W_{COMP_2} + Q_{waste\ heat}\left(1 - \frac{T_o}{T_{exchanger}}\right) - Q_{hot\ utility}\left(\frac{T_o}{T_{heater}} - 1\right)}{Ex_{in,fuel} + Ex_{in,Air}} \tag{3.21}$$

where ε_{CHP} = Exergy efficiency of the integrated system (%)

$W_{net,SOFC-H^+}$ = SOFC-H^+ Power generation (kW)

W_{COMP} = Compressor consumption (kW)

T_o = Reference temperature at 298.15 K (K)

$T_{exchanger}$ = Operating temperature of exchanger (K)

T_{heater} = Operating temperature of heater (K)

$Q_{waste\ heat}$ = Waste heat recovery from process (kW)

$Q_{hot\ utility}$ = Heat required for the hot utility (kW)

$Ex_{in,fuel}$ = Exergy flow rate inlet of fuel (W)

$Ex_{in,Air}$ = Exergy flow rate inlet of air (W)

The exergy efficiency of absorption chiller which is written as Eq. (3.22) [60].

$$\varepsilon_{Absorption\ chiller} = \frac{Q_{evap}\left(1-\frac{T_o}{T_{evap}}\right)}{Q_{gen}\left(1-\frac{T_o}{T_{gen}}\right)} \quad (3.22)$$

where $\varepsilon_{Absorption\ chiller}$ = Exergy efficiency of the absorption chiller (%)

T_{evap} = Operating temperature of evaporator (K)

T_{gen} = Operating temperature of generator (K)

Q_{evap} = Heat duty of evaporator (kW)

Q_{gen} = Heat duty of generator(kW)

Finally, the exergy efficiency of the integration between cooling, heat, and power of SOFC-H^+ can be specified as Eq. (3.23) [60].

$$\varepsilon_{CCHP} = \frac{W_{net,SOFC-H^+} - W_{COMP_1} - W_{COMP_2} + Q_{evap}\left(\frac{T_o}{T_{evap}}-1\right) - Q_{hot\ utility}\left(\frac{T_o}{T_{heater}}-1\right)}{Ex_{in,fuel} + Ex_{in,Air}} \quad (3.23)$$

where ε_{CCHP} is exergy efficiency of the integrated combined cooling heating and power system or trigeneration (%).

CHAPTER IV

CO-GASIFICATION OF COAL AND BIOMASS INTEGRATED WITH CALCIUM LOOPING CARBON DIOXIDE CAPTURE PROCESS

This chapter presents the performance analysis and optimization of coal/biomass co-gasification integrated with calcium looping carbon dioxide capture process. Section 4.1 shows the comparison between model prediction and experimental results extracted from the literature. Further, the verified models are used to investigate the effects of the operating conditions in the gasifier (i.e., gasifier temperature and steam to feed (S/F) mass ratio) and adsorber (i.e., CaO to feed (CaO/F) mass ratio, carbonator temperature and regenerator temperature) on hydrogen production. The results of both processes are discussed in Section 4.2 and 4.3, respectively. Further, Section 4.4 shows the optimization of both processes to determine the optimal condition that maximizes hydrogen production. Finally, the energy analysis is examined and discussed in Section 4.5.

4.1 Model validation

4.1.1 Syngas production through biomass gasification

This part presents the comparison results of syngas production obtained, the simulation results and experimental data. Three different experiment data are used to verify the proposed model. Firsty, Loha C. et al. [50] used rice husk (1 kg/hr) as feedstock where the circulating fluidized bed gasifier operated at temperature of 750 ^{o}C and pressure of 1.05 bar. Secondly, Minutillo, et al. [51], considered pellet pine wood as biomass, performed the down draft gasifier, operating at temperature of 1173 K and air to biomass ratio of 1.96. Finally, the experiment in coal gasification of Mota et al. [52] is considered. The bubbling fluidized bed gasifier was operated at operating temperature 750 ^{o}C and oxygen carrier to carbon 1. The model validation between simulation results and three experimental results that include Loha et al. [50], Minutillo

et al. [51] and Mota et al. [52] is shown in Figure 4.1. All results have the same trends and consistency with experiments. The experimental results indicate that the observed values of CH_4 are lower than expected. This discrepancy can be attributed to the experimental conditions, which might not have reached chemical equilibrium during testing. As a result, the model's predicted values of CH_4 are higher than the experimental data due to the assumption of equilibrium conditions in the model.

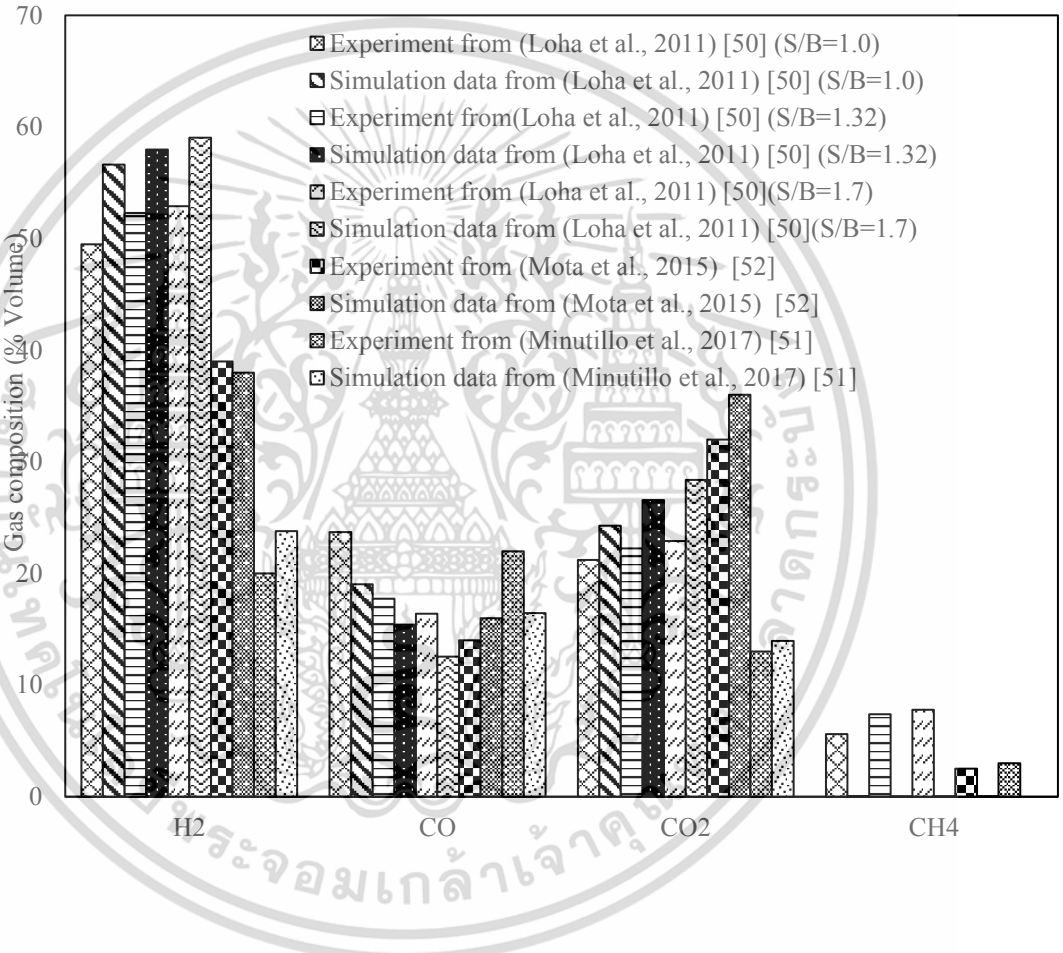

Figure 4.1 Comparison of syngas composition obtained from the model prediction and experimental data of Loha et al. [50], Minutillo et al. [51] and Mota et al. [52].

4.1.2 CO_2 capture efficiency of carbon dioxide capture process

In the CO_2 capture process, the simulated results obtained are compared with the experimental findings conducted by Atsonios et al. [53]. Their experimental studied the CO_2 adsorption and desorption operations, carried out in a 10 kW dual fluidized

bed (DFB) reactor at temperatures ranging from 600 to 700 °C, while the regenerator temperature exceeded 850 °C. Table 4.1 provides a comprehensive comparison of the dry gas product composition at the outlet stream of the cyclone separator unit, incorporating both the experimental data from Atsonios et al. [53] and the simulated results. This demonstrates a strong agreement between the model predictions and the experimental results of Atsonios et al. [53]. The predicted CO_2 mole fraction value and CO_2 capture efficiency align closely with the experimental results.

Table 4.1 Comparison of dry gas product composition at outlet stream of cyclone separator unit and CO_2 efficiency obtained from the model prediction and experimental data of Atsonios et al. [53]

Parameters	This study	Atsonios et al. [53]
Wet gas composition (mol fraction) CO_2, out	0.00456	0.018
CO_2 capture efficiency	88.06	85.57

4.2 Operating condition in gasification process

When the impact of operating conditions in gasification process is considered, the calcium looping carbon dioxide capture process is operated by using a carbonator temperature of 450 °C and a regenerator temperature of 950 °C with CaO/F mass ratio of 1.

4.2.1 Effect of gasifier temperature on syngas composition

In order to investigate the variations of gasifier temperature on syngas composition, the gasifier is operated at pressure of 1 atm. Mass flow rates of biomass, coal and steam are equally 1,000 kg/hr. This corresponds to coal to biomass (C/B) mass ratio of 1 and steam to feed (S/F) mass ratio of 1. Figure 4.2 illustrates the impact of gasifier temperature, varying between 500 and 1,000 °C, on syngas composition (based on a dry basis). The simulation results reveal that the mole fraction of H_2 increases as

the gasifier temperature rises from 500 to 700 °C. However, beyond 700 °C, the mole fraction of H_2 is steady due to limitations imposed by the chemical equilibrium. In contrast, the mole fractions of CO_2 and CH_4 decrease as the gasifier temperature increases. This phenomenon can be attributed to endothermic reactions such as the Boudouard reaction (Eq. (3.3)), water gas reaction (Eq. (3.5)), and steam methane reforming (Eq. (3.7)), which favor the production of H_2 when the gasifier operates at higher temperatures. Consequently, CO, CO_2, and CH_4 undergo conversion to a greater extent, yielding more H_2. Based on the simulation results, the optimal gasifier temperature is determined to be 700 °C.

4.2.2 Effect of S/F mass ratio on syngas composition

Figure 4.3 shows the influence of the S/F mass ratio on the syngas composition (on a dry basis). In this study, the S/F mass ratio is adjusted in a range of 0 to 10 while gasifier temperature of 700 °C and gasifier pressure of 1 atm are specified. From the simulation result, it is found that the mole fraction of H_2 increases significantly when the S/F mass ratio increases from 0 to 2. However, when the S/F mass ratio is higher than 2, the mole fraction of H_2 is stable. This behavior can be attributed to the introduction of more steam into the gasifier, which promotes water gas, water gas shift and steam reforming reactions (Eq. (3.7)) forward. Consequently, a decrease in the quantities of CH_4 and CO can be observed. With the gasifier operating at a temperature of 700 °C, a pressure of 1 atm, and an S/F mass ratio of 2, the gas product consists of approximately 65% H_2, 10% CO, 24% CO_2, and 0.06% CH_4. Notably, the syngas product consistently exhibits high levels of CO_2, necessitating the use of a CO_2 removal unit to enhance the quality of the syngas.

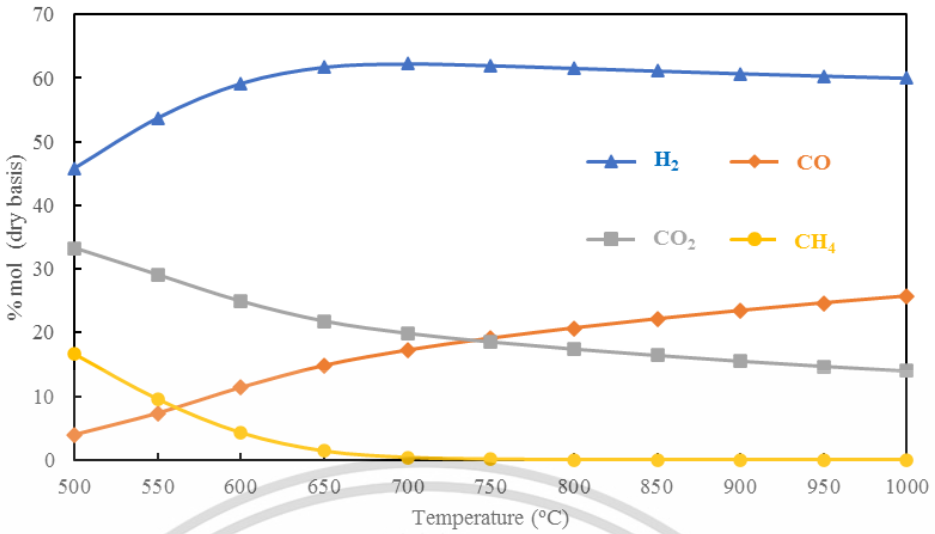

Figure 4.2 Effect of gasifier temperature on syngas composition at pressure of 1 atm, biomass mass flow rate of 1,000 kg/hr, coal mass flow rate of 1,000 kg/hr and S/F ratio of 1.

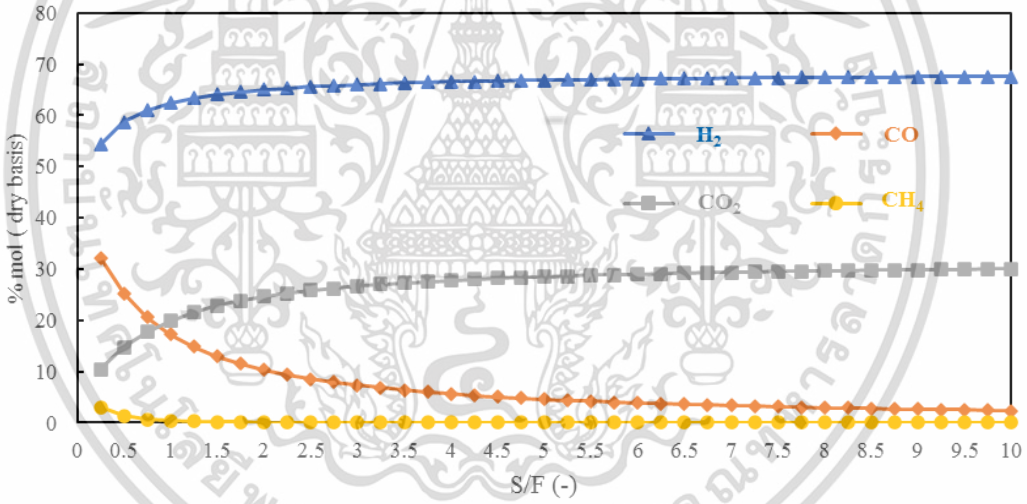

Figure 4.3 Effect of S/F mass ratio on syngas composition at gasifier temperature of 700 °C, gasifier pressure of 1 atm, biomass mass flow rate of 1,000 kg/hr and coal mass flow rate of 1,000 kg/hr.

4.3 Operating conditions in calcium looping carbon dioxide capture process.

In this section, the operating conditions in gasifier are specified at temperature of 700 °C, pressure of 1 atm and S/F mass ratio of 1 in which biomass and coal mass flow rates are equally as 1,000 kg/hr.

4.3.1 Effect of CaO/F mass ratio on syngas composition

Figure 4.4 shows the influence of varying CaO/F mass ratio from 0 to 6 on syngas composition**.** At a carbonator temperature of 450 °C, an increase in the CaO/F mass ratio from 0 to 2 demonstrates a significant enhancement in H_2 concentration within the gas product. Once the CaO/F ratio exceeds 2, the H_2 quantity experiences a slight decline and reaches a steady value. Conversely, the amount of CO, CO_2, and CH_4 exhibits substantial decreases with an increase in the CaO/F mass ratio. This behavior can be attributed to the adsorption of CO_2 on CaO as the absorbent, resulting in higher H_2 content and reduced levels of CO_2 through the carbonation reaction. As CO_2 is removed from the system, the quantities of CO and CH_4 decrease due to the shift of the water gas shift and steam methane reforming reactions towards the product side. Since a CaO/F mass ratio greater than 2 does not have any impact on H_2 production, a suitable CaO/F mass ratio is determined to be 2.

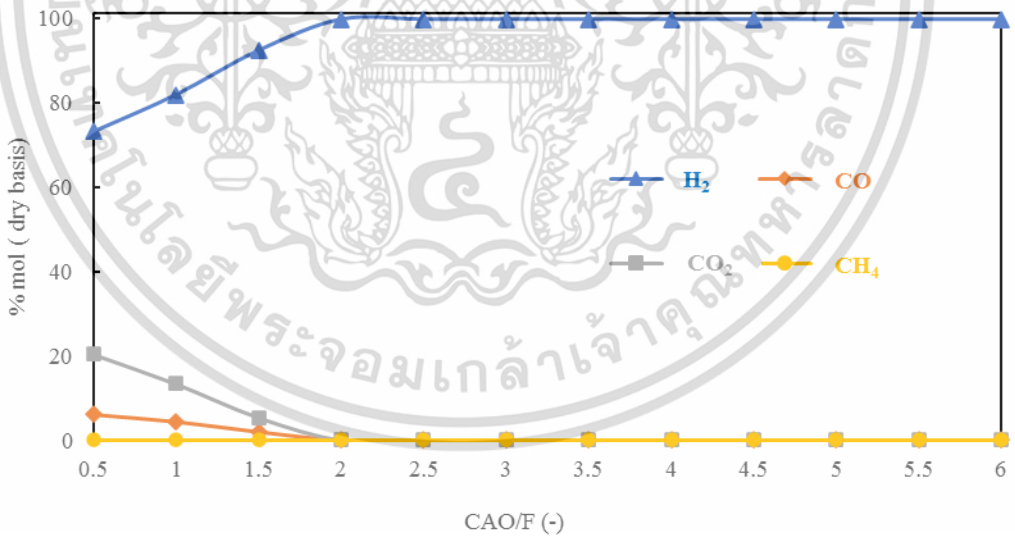

Figure 4.4 Effect of CaO/F mass ratio on syngas composition at carbonator temperature of 450 °C and regenerator temperature of 950 °C

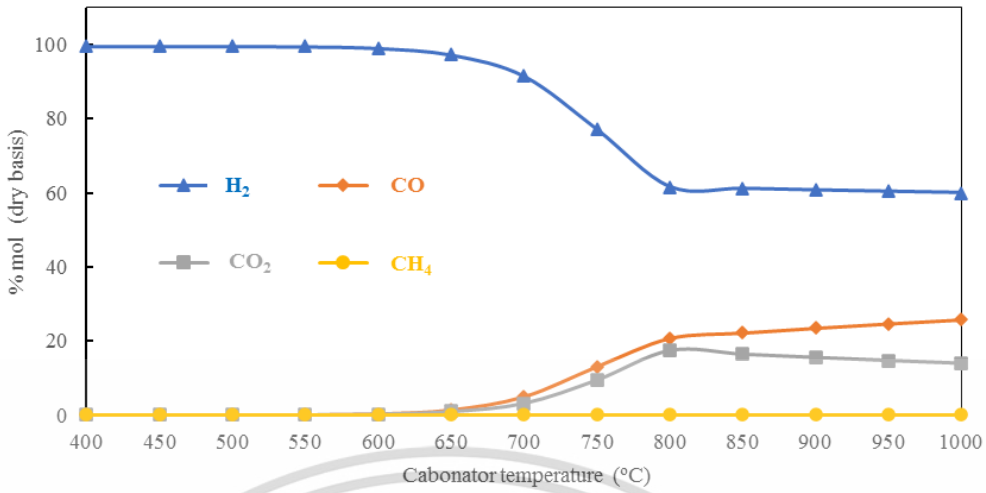

Figure 4.5 Effect of carbonator temperature on syngas composition at CaO/F mass ratio of 2 and regenerator temperature of 950 °C.

4.3.2 Effect of carbonator temperature on syngas composition

In this study, the temperature of carbonator is increased from 400 to 800 °C. The syngas composition as a function carbonator temperature is depicted in Figure 4.5. The simulation results indicate a significant decrease in H_2 mole fraction when the carbonator is operated at temperatures above 650 °C. At these higher temperatures, the presence of CO and CO_2 becomes evident. This behavior can be attributed to the nature of the carbonator reaction, which is an exothermic reaction that favors lower temperature operation. As the carbonator temperature increases, the chemical equilibrium shifts backward, resulting in the desorption of CO_2 from $CaCO_3$. Additionally, at higher carbonator temperatures, the reversed water gas shift reaction can occur, leading to a reduction in the amounts of CO_2 and H_2.

However, it should be noted that the ranges of appropriate carbonation temperature (450-550°C) obtained from this work may be lower than that from other literatures. This is mainly cause by the occurrence of water gas shit and carbonation reactions in the calcium looping carbon dioxide capture process. When the PRESYNGA stream, consisting of H_2, CO, CO_2 and high amount of H_2O, is fed into the adsorption process, water gas shift reaction can occur and thus, CO_2 and H_2 can be produced. In the adsorption process, CO_2 not only from the PRESYNGA stream but also produced from the water gas shift reaction are adsorbed into CaO through the carbonation

reaction. When two reactions occur in a single unit, overall reaction temperature can be reduced [64].

4.3.3 Effect of regenerator temperature on CO_2 removal

Figure 4.6 illustrates the relationship between the amount of CO_2 and regenerator temperature, ranging from 400 to 1,400 °C, with a CaO/F mass ratio of 2 and a carbonator temperature of 600 °C. The simulation results indicate that the desorption of CO_2 in the regeneration process initiates at temperatures between 900 and 1,000 °C, as evidenced by the increase in CO_2 production at these temperatures. However, once the temperature exceeds 950 °C, the concentration of CO_2 reaches a constant level. Based on this study, the optimal regenerator temperature is determined to be 950 °C.

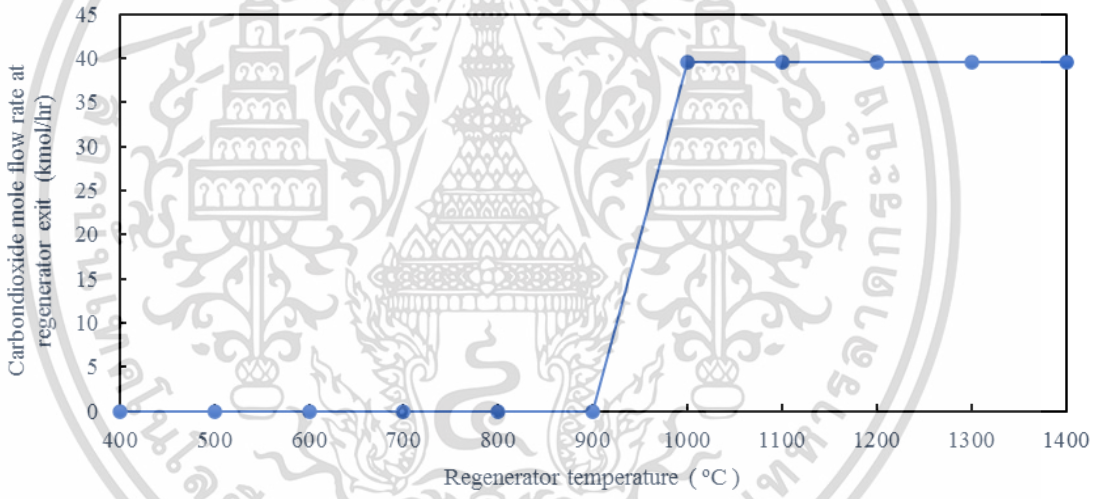

Figure 4.6 Effect of regenerator temperature on CO_2 mole fraction at CaO/F mass ratio of 2 and carbonator temperature of 600 °C.

4.4 Optimization of coal/biomass co-gasification integrated with calcium looping carbon dioxide capture process

The study presented in Section 4.2 and 4.3 based on the sensitivity analysis, the trends of the results and the importance of each operating condition are known. Then, the optimal operating conditions for the gasification and calcium looping process are determined using the Design of Experiments (DOE) method.

4.4.1 Coal/biomass co-gasification process

Based on the findings presented in Section 4.2, both gasifier temperature and S/F mass ratio have significant influences on H_2 production. Besides that, the proportion of coal in biomass or coal to biomass (C/B) mass ratio is also an important parameter. Therefore, the selected parameters in co-gasification of biomass and coal consist of (A) gasifier temperature, (B) S/F mass ratio, (C) C/B mass ratio. In this part, the full factorial design of 3 factors with 2 levels is considered and thus, there are 8 numbers of experiment. The response results from the 2^3 factorial experimental design analysis with a single replicate are also shown in Table 4.2. The ANOVA statistical analysis of the results obtaining with a confidence level of 95% or p-value equals to 0.05 were summarized in Table 4.3

Table 4.2 The response results from the 2^3 factorial experimental design analysis of co-gasification biomass and coal with Aspen Plus simulator version 10

Run	Gasifier Temperature (°C)	S/F mass ratio	C/B mass ratio	H_2 content (%vol., dry basis)
1	700	1	0.50:0.50	61.12
2	700	1	0.75:0.25	61.96
3	700	2	0.50:0.50	64.09
4	750	1	0.75:0.25	61.81
5	750	2	0.75:0.25	64.68
6	750	1	0.50:0.50	61.04
7	700	2	0.75:0.25	65.09
8	750	2	0.50:0.50	64.09

Code variable:

−1 (Low) Gasifier temperature = 700 °C, S/F mass ratio = 1, and C/B mass ratio = 0.50:0.50.

+1 (High) Gasifier temperature = 750 °C, S/F mass ratio = 2, and C/B mass ratio = 0.75:0.25

From the analysis of variance (ANOVA) presented in Table 4.3, it is evident that the (B) S/F mass ratio and (C) C/B mass ratio are significant variables, as indicated by their p-values being less than 0.05. Figure 4.7 illustrates the impact of S/F and C/B mass ratio on the H_2 content (%vol., dry basis). The results demonstrate that increasing the S/F mass ratio from 1 to 2 positively affects the %vol. of H_2, as depicted in Figure 4.7. This can be attributed to the presence of steam in the feed, which promotes forward reactions such as the water gas shift (Eq. (3.5)) and steam methane reforming (Eq. (3.7)). Regarding the C/B mass ratio, the findings indicate that higher C/B mass ratios lead to increased H_2 composition. This can be attributed to the lower carbon content in biomass compared to coal, as a higher proportion of biomass reduces CO production [61-62]. From response surface shown in Figure 4.8, it is found that the maximum H_2 content in co-gasification process is 65 %vol. at C/B ratio of 0.75:0.25, S/F mass ratio of 2 and gasifier temperature of 700 °C.

Table 4.3 Analysis of variance (ANOVA) for the regression model of H_2 content (%vol., dry basis)

Source	Sum of Squares	df	Mean Square	F-value	p-value	
Model	19.34	2	9.67	494.63	< 0.0001	significant
B-S/F	18.05	1	18.05	923.32	< 0.0001	
C-C/B	1.29	1	1.29	65.95	0.0005	
Residual	0.0978	5	0.0196			
Cor Total	19.44	7				
Std. Dev.	0.1398		R^2	0.995		
Mean	62.98		Adjusted R^2	0.993		
C.V. %	0.222		Predicted R^2	0.987		
			Adeq Precision	44.464		

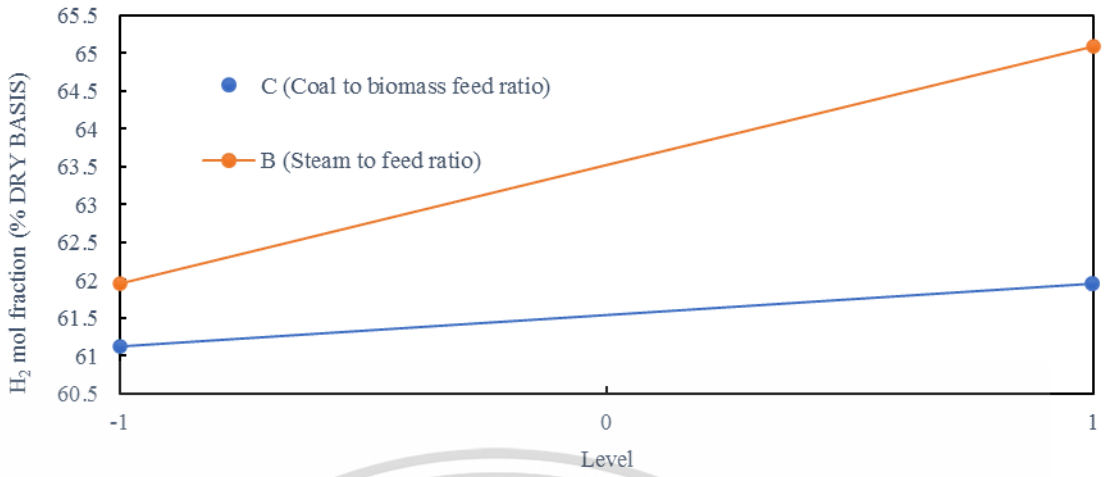

Figure 4.7 Effect of S/F and C/B mass ratio on H_2 content (%vol., dry basis).

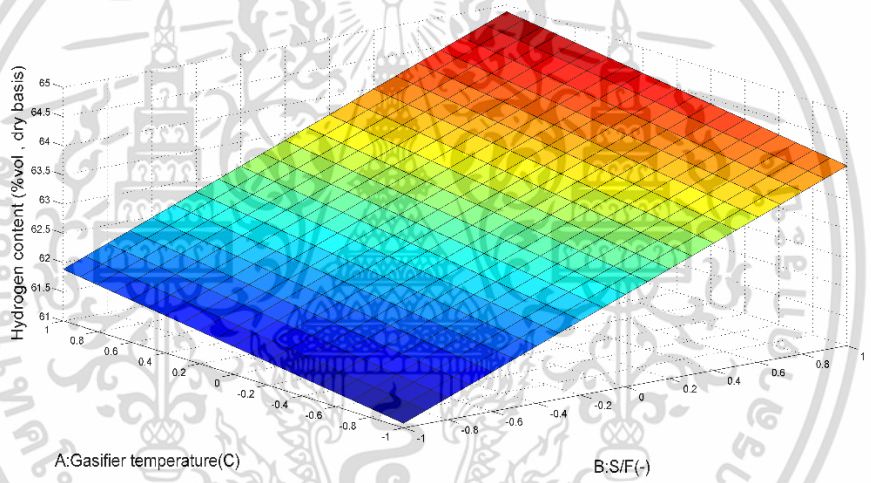

Figure 4.8 Response surface plot of H_2 content (%vol., dry basis) in co-gasification process

4.4.2 Calcium looping carbon dioxide capture process

For the analysis of calcium looping carbon dioxide capture process presented in Section 4.3, the selected process parameters are (D) carbonator temperature and (E) CaO/F mass ratio. The full factorial design 2 factors with 2 levels and the number of experiments is 4 experimental runs with a single replicate were shown in Table 4.4. The ANOVA statistical analysis of the results obtaining with a confidence level of 95% are summarized in Table 4.5

Table 4.4 The response results from the 2^2 factorial experimental design analysis of carbon dioxide capture process with Aspen Plus simulator version 10

Run	Carbonator temperature (°C)	CaO/F mass ratio	CO_2 capture (%)	H_2 content (%vol., dry basis)
1	550	1	79.87	98.47
2	450	3	99.99	99.59
3	550	3	99.65	99.53
4	450	1	78.42	99.01

Code variable:

−1 (Low) Carbonator temperature = 450 °C, CaO/F mass ratio = 1

+1 (High) Carbonator temperature = 550 °C, CaO/F mass ratio = 3

Table 4.5 ANOVA for the regression model of % CO_2 capture in calcium looping process

Source	Sum of Squares	df	Mean Square	F-value	p-value	
Model	427.22	1	427.22	769.02	0.0013	significant
E-CaO/F	427.22	1	427.22	769.02	0.0013	
Residual	1.11	2	0.555			
Cor Total	3151.42	3				

Std. Dev.	0.745	R^2	0.997
Mean	89.49	Adjusted R^2	0.996
C.V. %	0.832	Predicted R^2	0.9896
		Adeq Precision	39.217

Based on the results obtained from the ANOVA analysis presented in Table 4.5, it is evident that the only significant variable affecting $\%CO_2$ capture is the CaO/F mass ratio. Figure 4.9 illustrates the effect of CaO/F mass ratio on $\%CO_2$ capture, showing a substantial improvement from approximately 78% to 100% when the CaO/F mass ratio is increased from 1 to 3. Considering the response surface shown in Figure 4.10, the maximum $\%CO_2$ capture of 99.99% can be achieved with a CaO/F mass ratio of 3 and a carbonator temperature of 450 °C. Under these optimal conditions, a maximum %vol. of H_2 of 99.59% can be achieved.

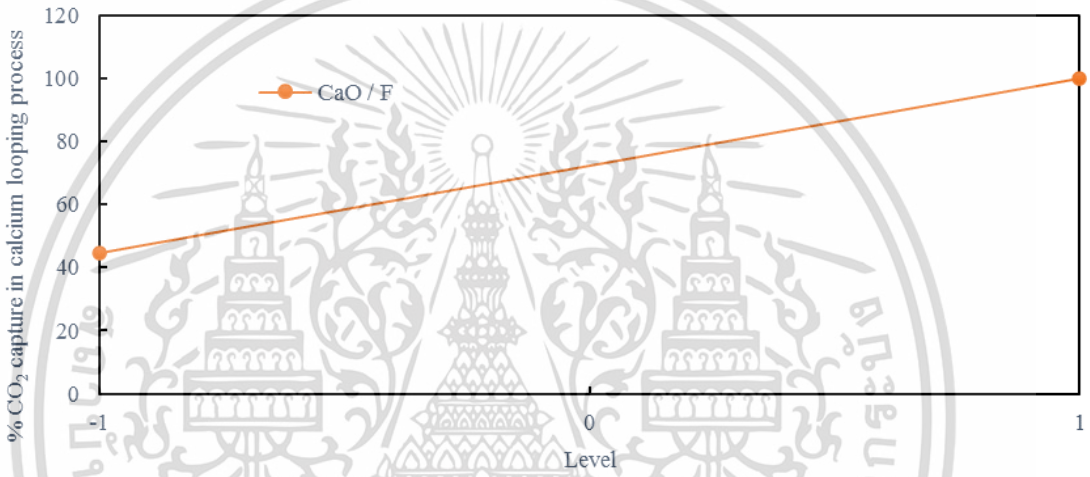

Figure 4.9 Effect of CaO/F mass ratio on $\%CO_2$ capture in calcium looping process.

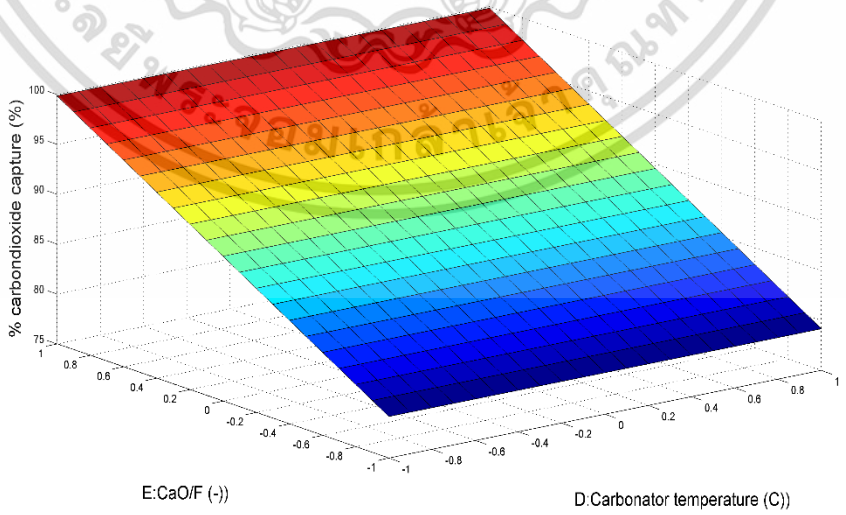

Figure 4.10 Response surface plot of $\%CO_2$ capture in calcium looping process.

Table 4.6 summarizes the optimal operating conditions of coal/biomass gasification integrated with calcium looping process. The results reveal that the maximum H_2 content of 99.59 %vol. can be obtained when co-gasification is operated at gasifier temperature of 700 °C, S/F mass ratio of 2 and C/B mass ratio of 0.75:0.25 while the CO_2 capture process should be operated at carbonator temperature of 450 °C and regenerator temperature of 950 °C with CaO/F mass ratio of 3.

Table 4.6 Optimization of coal/biomass co-gasification integrated with calcium looping carbon dioxide capture process

Parameter	Value
Operation in coal/biomass co-gasification	
Gasifier Temperature (°C)	700
Biomass mass flowrate (kg/hr)	500
Coal mass flowrate (kg/hr)	1,500
S/F mass ratio	2
C/B mass ratio	0.75:0.25
Operation in calcium looping carbon dioxide capture process	
Carbonator temperature (°C)	450
Regenerator temperature (°C)	950
CaO/F mass ratio	3
Results	
Hydrogen yield (g hydrogen/kg biomass feeding)	92.38
Hydrogen production (kg/hr)	184.75
Hydrogen mole fraction (% dry basis)	99.59
CO_2 capture efficiency (%)	99.99

4.5 Energy analysis of coal/biomass co-gasification integrated with calcium looping carbon dioxide capture process

In the co-gasification of coal and biomass integrated with the calcium looping carbon dioxide capture process, the utilization of heat utility is crucial to facilitate various unit operations such as the gasifier, calciner, and carbonator units. Therefore, it becomes necessary to analyze the thermodynamic efficiency of this integrated process. This analysis involves evaluating the efficiency by considering the optimal operating conditions obtained from the previous section, which includes the hydrogen energy output, total energy input, and the input of the mixed feedstock. By applying relevant equations, the thermodynamic efficiency of the co-gasification process can be determined as Eq. (4.1).

$$\eta_{H_2}(\%) = \frac{m_{H_2} \times LHV_{H_2}}{m_{biomass} \times LHV_{biomass} + m_{coal} \times LHV_{coal} + \dot{m}_{\text{steam}} h_{\text{steam}}} \times 100 \qquad (4.1)$$

where η_{H_2} is thermal efficiency of process (%)

LHV_{H_2} is lower heating value of hydrogen (kJ/kg)

m_{H_2} is hydrogen mass flowrate (kg/hr)

$LHV_{biomass}$ is Lower heating value of biomass (kJ/kg)

$m_{biomass}$ is biomass mass flowrate (kg/hr)

$\dot{m}_{\text{steam}}$ is steam mass flow rate (kg/hr)

h_{steam} is specific enthalpy of steam at 800 °C = 3,663.84 kJ/kg.

Under the optimal operating conditions, the heat duty of each unit in the process are shown in Table 4.7. From the results listed in Table 4.6, the energy efficiency of this system is 42.86%.

Table 4.7 The heat duty of each unit in the co-gasification of biomass and coal integrated with the calcium looping carbon dioxide capture process

Heat duty of each unit (kW)	Values
Gasifier unit (kW)	3,332.32
Regenerator unit (kW)	3,207
Carbonator unit (kW)	-3,023.59

CHAPTER V

TRIGENERATION PROCESS CONSISTING OF PROTON CONDUCTING SOLID OXIDE FUEL CELL AND LIBR ABSORPTION CHILLER

This chapter presents the performance analysis and optimization of a trigeneration process consisting of a proton conducting solid oxide fuel cell (SOFC-H^+) and a LiBr absorption chiller. The first section (Section 5.1) shows the comparison results obtained from the simulation of SOFC-H^+ and LiBr absorption chiller with the experimental data extracted from the literature. Section 5.2 presents the performance analysis of SOFC-H^+ with wider range of operating conditions, such as temperature and pressure of SOFC-H^+, fuel utilization and air and fuel molar flow rates. Further, the sensitivity analysis of LiBr absorption chiller is described in Section 5.3. When the effects of each parameter in both SOFC-H^+ and LiBr absorption chiller are considered, the optimization of integrated process is performed. The results are shown in Section 5.4. Finally, the exergy efficiency of trigeneration process consisting of SOFC-H^+ and LiBr absorption chiller is determined.

5.1 Model validation

5.1.1 SOFC-H^+ model

In this work, the simulation result obtained from the SOFC-H^+ model is validated with the experiment result of Zhang et al. [54] and Lei et al. [63]. The model validation is performed under the operation of SOFC-H^+ within a temperature range of 550 to 700 °C. The fabrication of SOFC-H^+ used in Zhang et al. [54] was the thicknesses of anode, cathode and electrolyte are 550, 40 and 15 μm. While the thickness of electrode and electrolyte used in Lei et al. [60] are 0.33 mm and 15 μm. Figures 5.1(a) and (b) present a comparison of cell voltage and power density between the simulation and experimental results. The model predictions align well with the experimental data within a current density range of 0 to 1.2 A/cm^2.

Notably, Figure 5.1(a) shows a decrease in cell voltage with increasing the current density. The decrement of cell voltage can be attributed to the three voltage losses that increase simultaneously. It can be observed that the activation overpotential is important at low current density due to the occurrences of the oxidation and reduction reactions at the electrodes. As the current density reaches a moderate level, the ohmic overpotential becomes significant due to the transferring of proton and electron from the anode to the cathode. Lastly, the concentration overpotential, resulting from the difference in gas concentration at the electrode-electrolyte interface and bulk, becomes more prominent at high current density. As seen in Figure 5.1(a), it can be observed that the cell voltage continuously decreases, approaching zero at maximum current density. In contrast to cell voltage, power density initially increases to a maximum value and then slightly decreases at high current density (Figure 5.1(b)). This behavior can be attributed to the higher cell voltage observed at low current density, which enhances power density. However, at higher current density, the sharp drop in cell voltage results in a reduction of power density

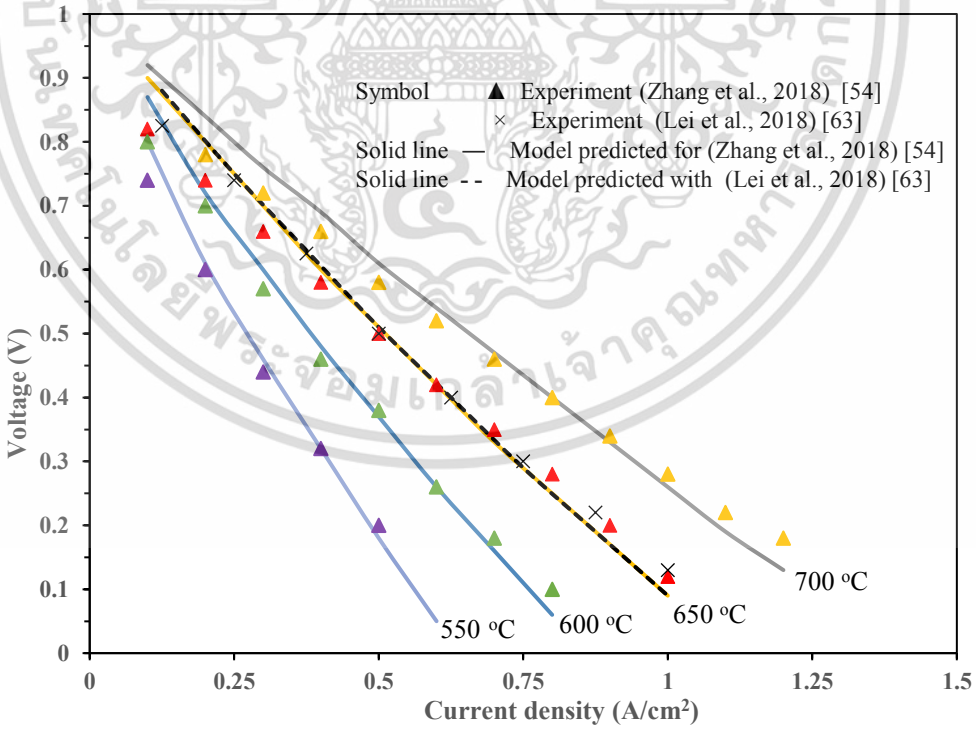

(a)

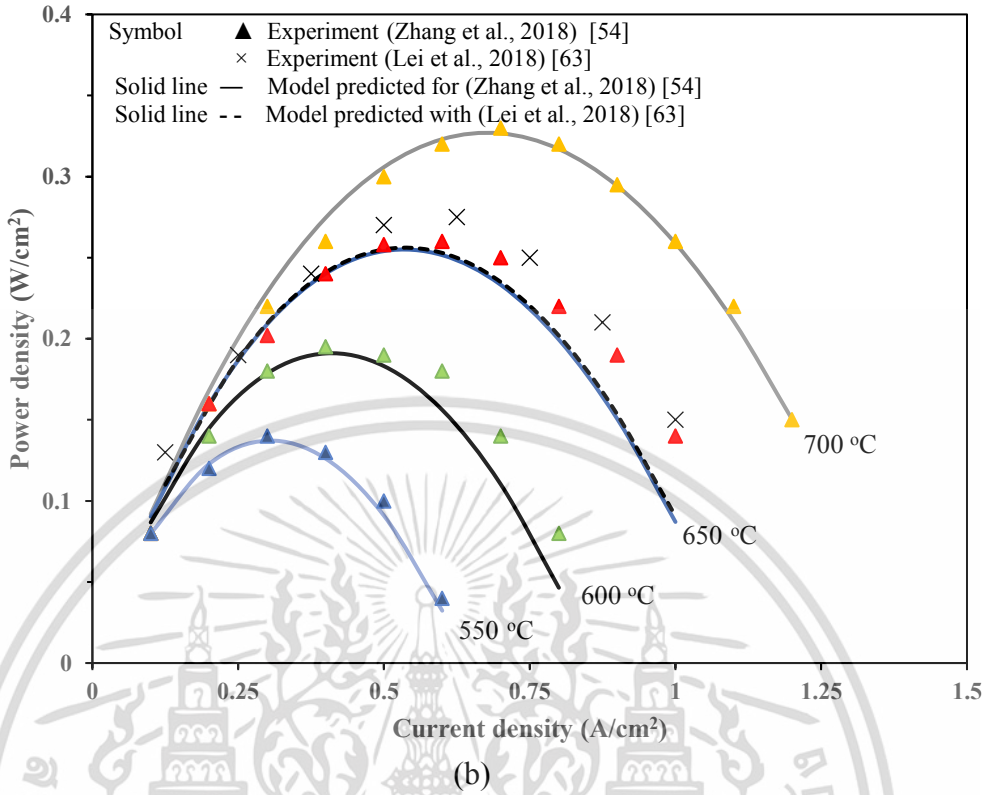

Figure 5.1 The comparison results of (a) cell voltage and (b) power density obtained from the SOFC-H^+ model and experiment results of Zhang et al. [54] and Lei et al. [63].

5.1.2 LiBr absorption model

The validation of the LiBr absorption chiller model developed in Aspen Plus has already been proposed in Somers et al. [45]. In their research, the simulation result obtained from Aspen Plus is validated with the Engineering Equation Solver (EES) model of Herold et al. [57]. EES database is referred from ASHARE Handbook (HVAC application heating ventilating and air-conditioning applications) [58]. It is noted that the EES model is more detailed than the experiment and thus, the comparison results obtained from EES and Aspen Plus can be accepted. From the results proposed in Somers et al. [45], it is found that the difference in results obtained from EES and Aspen Plus is only 3% for single stage LiBr absorption chiller.

5.2 Operating conditions in SOFC-H^+

In this section, a sensitivity analysis is conducted to examine the impact of various operating conditions of SOFC-H^+, that include operating pressure, operating temperature, fuel utilization, and air-to-fuel (A/F) molar ratio, on the system efficiency. In the base case condition, the SOFC-H^+ operates at 550 ℃ and 1 bar with fuel utilization of 0.8. The molar flow rate of air and fuel (or hydrogen) are 2.78 and 1 kmol/hr respectively. Thus, air-to-fuel (A/F) molar ratio equal to 2.78.

5.2.1 Effect of SOFC-H^+ operating pressure

Figures 5.2 and 5.3 show the influence of SOFC-H^+ pressure, varying in a range of 1 to 10 bar, on the electrical performance of SOFC-H^+. The results reveal that increasing the operating pressure has little effects on all voltage losses, cell voltage, and power density. Theoretically, the SOFC-H^+, operating at high pressure can improve the open-circuit voltage. Additionally, the concentration overpotential can be decreased (Figure 5.2) due to the enhancement of gas diffusion at the three-phase boundary layers. According to the obtained results, it can be observed that an increase in SOFC-H^+ pressure leads to a higher cell voltage, subsequently resulting in an increase in power density (Figure 5.3). However, the impact of pressure variation on the electrical performance is relatively small. The operation of the system at higher pressures can affect the power consumption of the compressor, which in turn influences fixed costs, operating costs, and overall electrical efficiency.

5.2.2 Effect of SOFC-H^+ operating temperature

Figures 5.4 and 5.5 depict the impact of SOFC-H^+ temperature, that is adjusted between 550 and 700 °C, on cell voltage, all voltage losses, and power density. The simulation results indicate reductions in activation and ohmic overpotential and a slight increase in concentration overpotential with increasing SOFC-H^+ temperature (Figure 5.4). Consequently, the improvement of cell voltage and power density can be

observed as seen in Figure 5.5. When the SOFC-H^+ is operated at higher temperature, the higher electrochemical reaction rate is facilitated by the Arrhenius law, resulting in a decrease in activation overpotential. Furthermore, a reduction in ohmic overpotential can be attributed to the higher protonic conductivity achieved at elevated temperatures in the SOFC-H^+ system. However, it is noteworthy that the rate of increase in cell voltage and power density tends to diminish at high temperatures, as the SOFC-H^+ exhibits optimal proton conductivity at intermediate temperature operation.

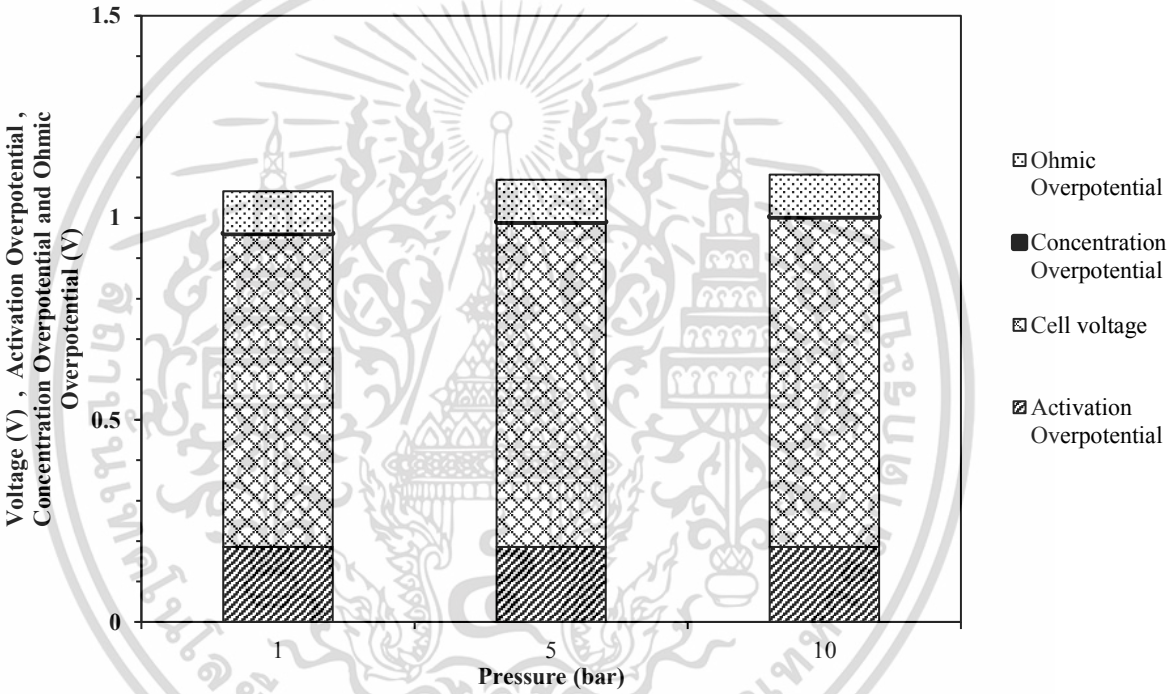

Figure 5.2 Effect of SOFC-H^+ operating pressure on all voltage losses at SOFC-H^+ temperature of 550 °C, fuel utilization of 0.8 and A/F ratio 2.78.

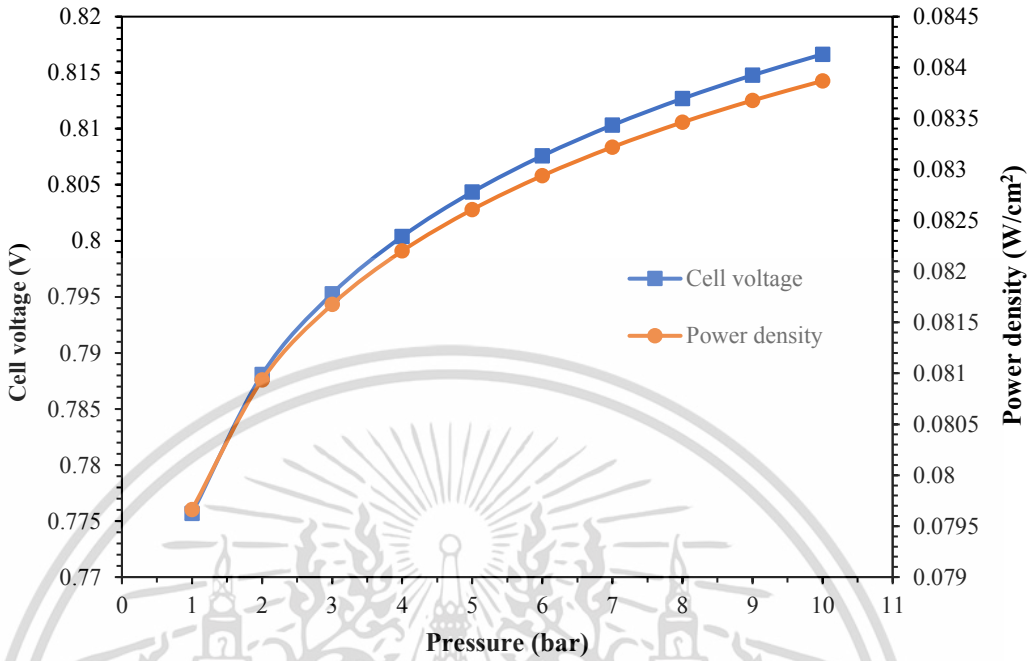

Figure 5.3 Effect of SOFC-H$^+$ pressure on cell voltage and power density at SOFC-H$^+$ temperature of 550 °C, fuel utilization of 0.8 and A/F ratio 2.78.

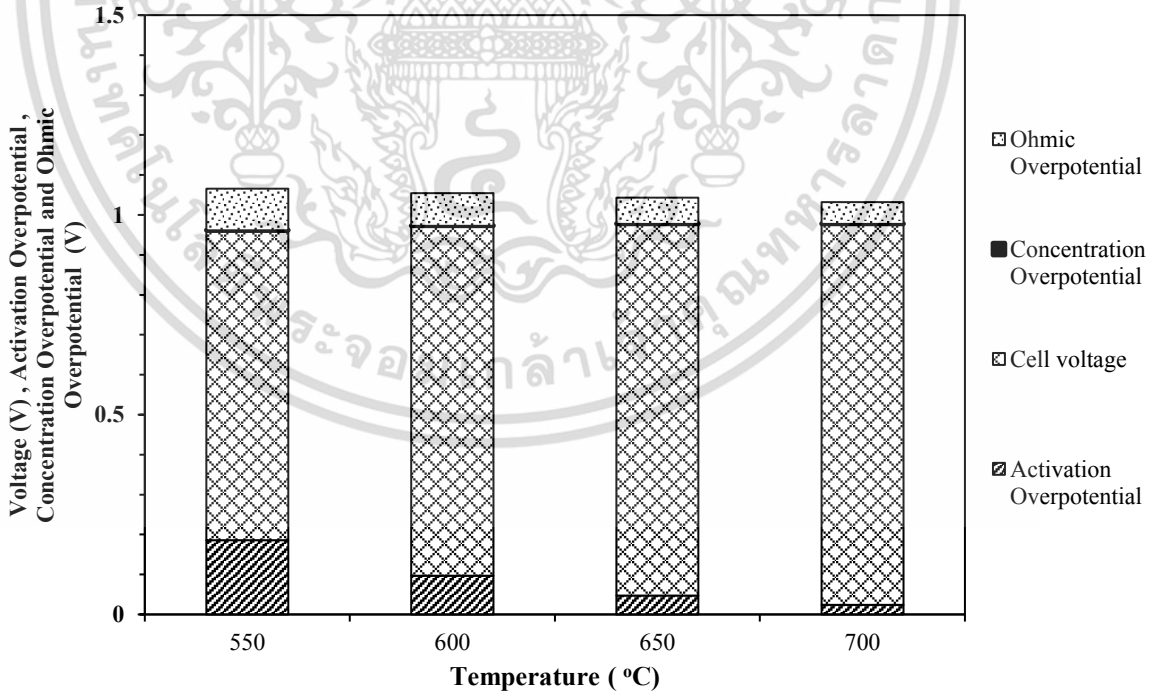

Figure 5.4 Effect of SOFC-H$^+$ operating temperature on all voltage loss at SOFC-H$^+$ pressure of 1 bar, fuel utilization of 0.8 and A/F ratio 2.78.

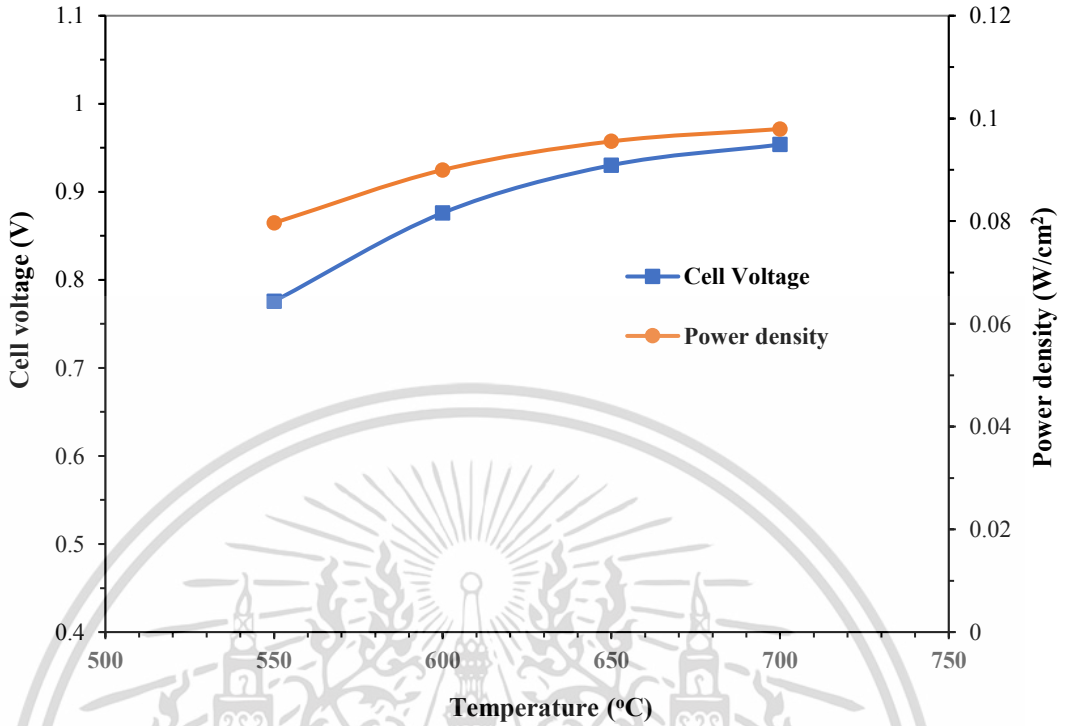

Figure 5.5 Effect of SOFC-H^+ temperature on cell voltage and power density at SOFC-H^+ pressure of 1 bar, fuel utilization of 0.8 and A/F ratio 2.78.

5.2.3 Effect of fuel utilization

In this section, the effect of fuel utilization on SOFC-H^+ electrical performance is examined. Fuel utilization is changed between 0.80 and 0.95. Due to no steam formation at the anode side in SOFC-H^+, more complete fuel utilization is possible without the problem of rapid drop in cell voltage at high current density. Fuel utilization indicates the consumption of fuel to produce electricity (current density). Therefore, increasing fuel utilization corresponds to a higher consumption of fuel for the electrochemical reaction, resulting in an increase in current density. From the simulation result demonstrated in Figure 5.7, it is found that the SOFC-H^+ operated with a fuel utilization range of 0.8 to 0.85 leads to an increase in current density, rising from 0.080 to 0.122 A/cm². The SOFC-H^+ operated at higher current density results in higher voltage losses and thus, the cell voltage is reduced (Figure 5.6). However, the simulation results reveal an improvement in power density, which increases from 0.079 to 0.089 W/cm².

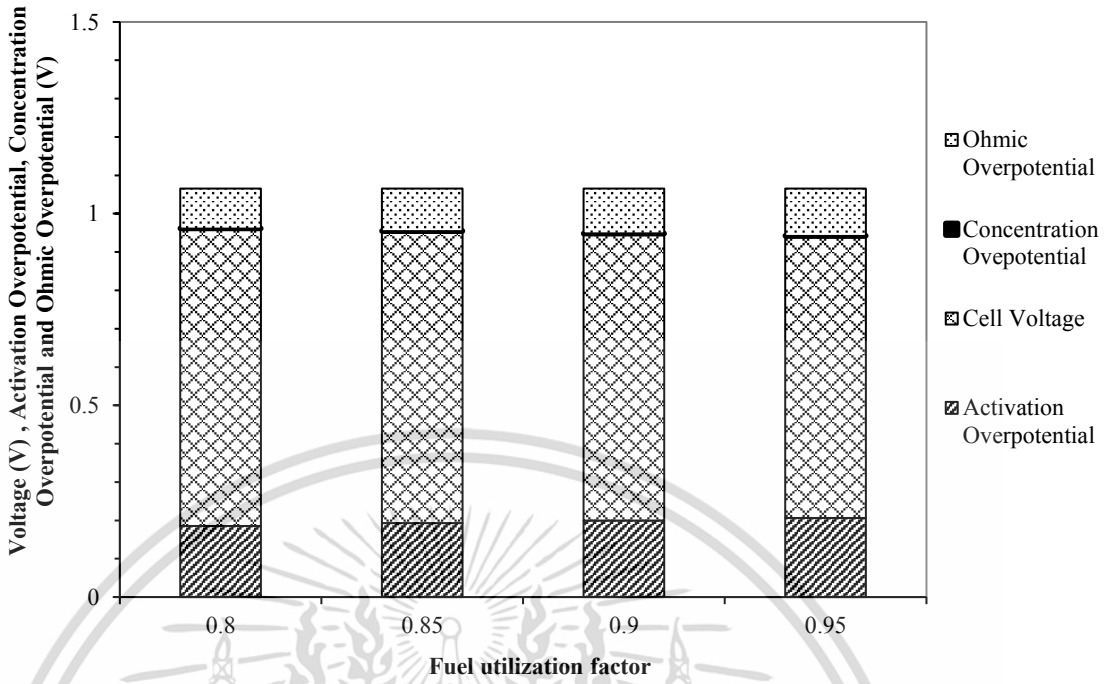

Figure 5.6 Effect of fuel utilization on all voltage loss at SOFC-H^+ temperature of 550 °C, SOFC-H^+ pressure of 1 bar and A/F ratio 2.78.

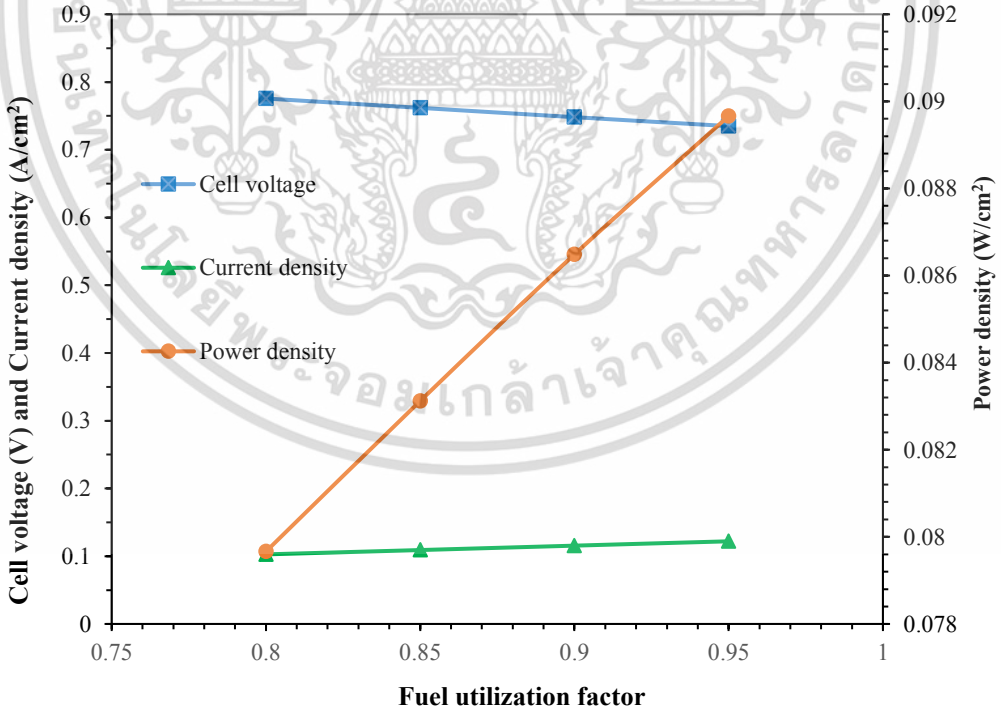

Figure 5.7 Effect of fuel utilization on current density, cell voltage and power density at SOFC-H^+ temperature of 550 °C, SOFC-H^+ pressure of 1 bar and A/F ratio 2.78.

5.2.4 Effect of air and fuel molar flow rate

This section presents the performance analysis of the SOFC-H^+ system, considering the electricity generation and the specific enthalpy of the exhaust gas at different A/F molar ratios. The A/F molar ratio can be adjusted by modifying the fuel or air molar flow rates. The simulation results, depicted in Figure 5.8, indicate that the variation in air flow rate has a minimal impact on cell voltage. This suggests that the A/F molar ratio does not significantly affect the cell voltage when adjusting the air flow rate. Conversely, increasing the fuel molar flow rate has a substantial effect, leading to a significant decrease in cell voltage. When the fuel utilization of 0.8 and the air molar flow rate of 1 kmol/hr are held constant, the results show that increasing the fuel molar flow rate results in a higher amount of fuel available for the electrochemical reaction. This leads to an improved current density, as illustrated in Figure 5.9. From the simulation results, it is found that increasing the fuel molar flow rate from 1 to 6 kmol/hr enhances the current density from 0.10 to 0.62 A/cm^2. However, a higher current density also leads to an increase in all overpotentials, resulting in a deterioration of the cell voltage from 0.78 to 0.06 V. Additionally, the power density initially increases and reaches a maximum value of 0.14 W/cm^2 at a fuel molar flow rate of 3 kmol/hr. Subsequently, it slightly decreases to 0.04 W/cm^2 at 6 kmol/hr.

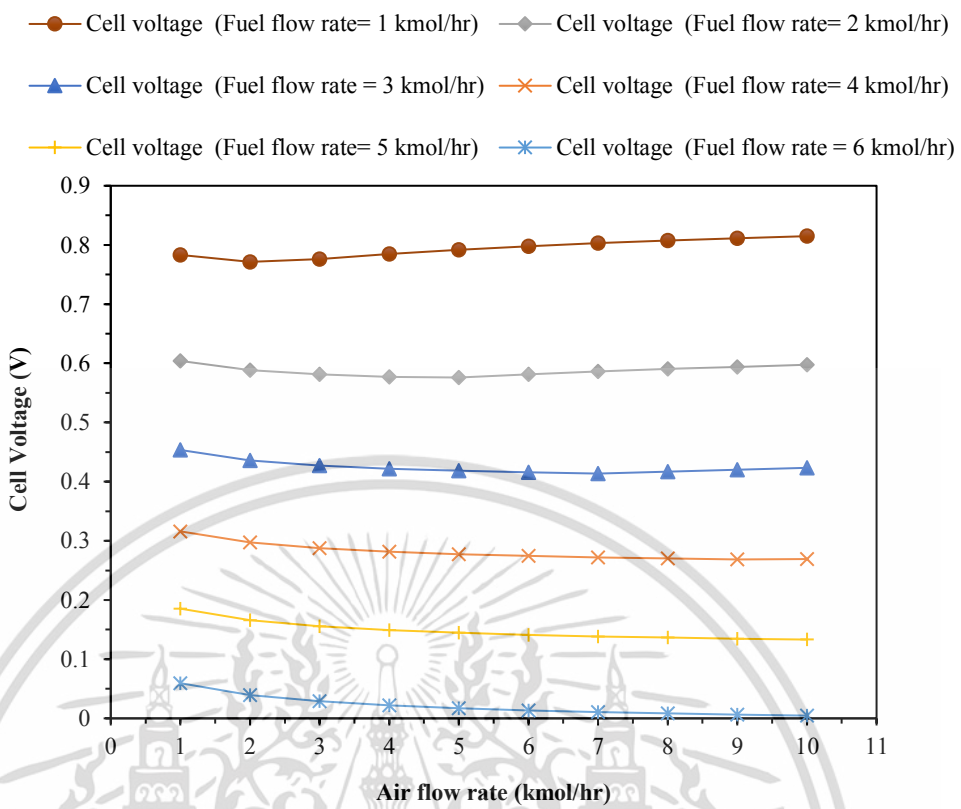

Figure 5.8 Effect of air and fuel molar flow rate on cell voltage at SOFC-H^+ temperature of 550 °C, SOFC-H^+ pressure of 1 bar, fuel utilization of 0.8

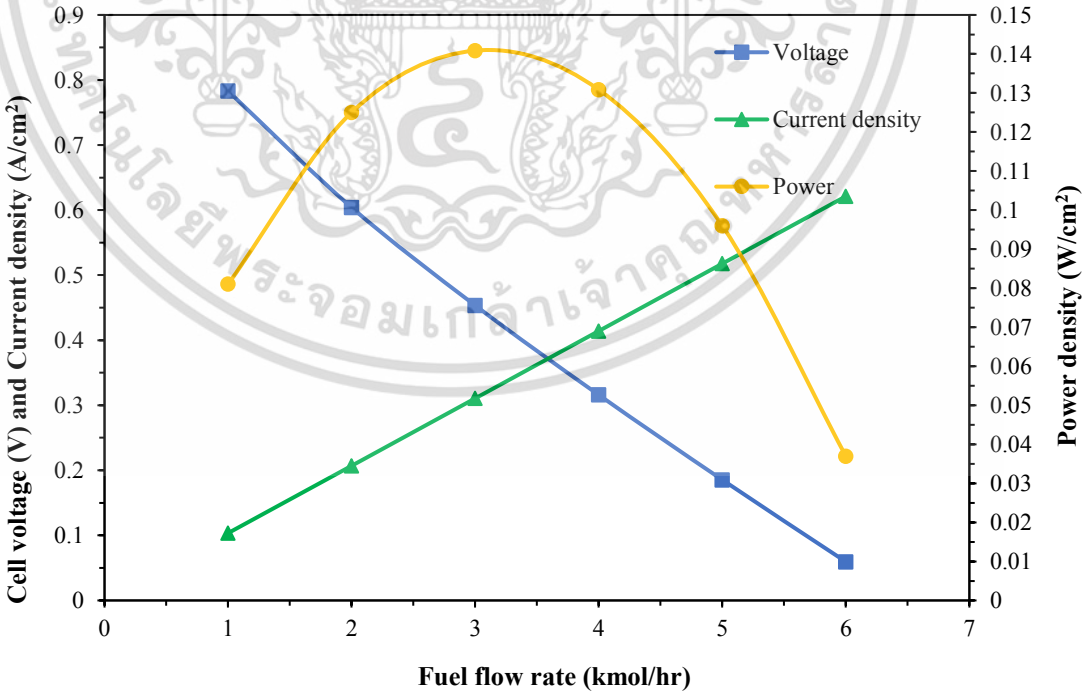

Figure 5.9 Effect of fuel molar flow rate on current density and power density at SOFC-H^+ temperature of 550 °C, SOFC-H^+ pressure of 1 bar, fuel utilization of 0.8

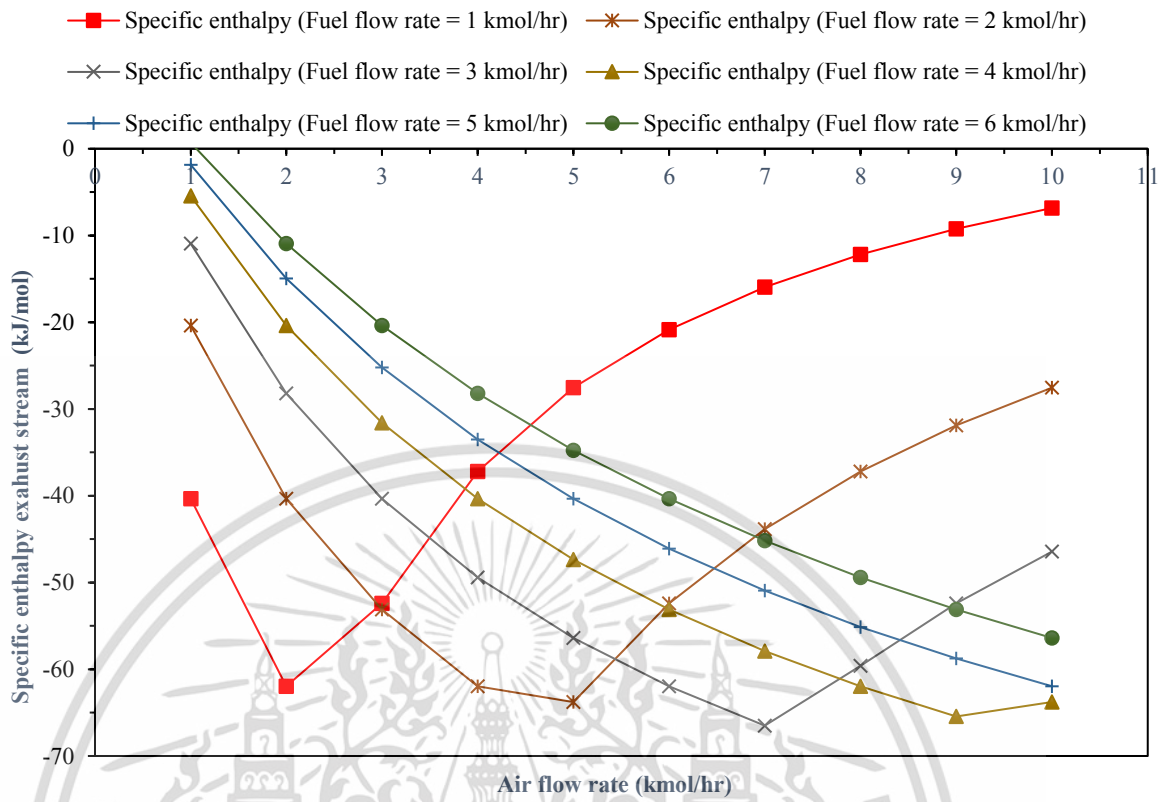

Figure 5.10 Effect of air and fuel molar flow rates on specific enthalpy of exhaust stream at SOFC-H^+ temperature of 550 °C, SOFC-H^+ pressure of 1 bar, fuel utilization of 0.8

Apart from the electrochemical performance, the specific enthalpy of the exhaust stream is also considered. Since the exhaust stream at the outlet of the SOFC-H^+ unit is utilized in the heat exchanger unit to recover waste heat energy for driving the absorption chiller. Figure 5.10 illustrates the impact of air and fuel molar flow rates on the specific enthalpy of the exhaust stream. The simulation results demonstrate that the maximum specific enthalpy can be achieved under specific A/F molar ratios. These optimal ratios are observed at an A/F molar ratio of 2 (with air flow rate of 2 kmol/hr and fuel flow rate of 1 kmol/hr), 2.33 (with air flow rate of 7 kmol/hr and fuel flow rate of 3 kmol/hr), and 2.5 (with air flow rate of 5 kmol/hr and fuel flow rate of 2 kmol/hr). The exhaust gas obtained from these ratios exhibits a specific enthalpy ranging from 61 to 66 kJ/mol. Considering that the A/F molar ratio significantly impacts both electrical and energy efficiencies, it is crucial to carefully determine the

appropriate A/F molar ratio through optimization processes to maximize system performance.

5.3 Operation conditions in the LiBr absorption chiller

This section focuses on LiBr absorption chiller performance. The parameters considered are hot water mass flow rate, hot water and steam inlet temperature, evaporator temperature and generator temperature on the COP value.

5.3.1 Effect of hot water mass flow rate and inlet temperature

Figures 5.11(a) and (b) depict the variations of the Coefficient of Performance (COP) with respect to several key parameters, including hot water mass flow rate and hot water and steam inlet temperature. Once the exhaust gas from the SOFC-H^+ unit is directed to the heat exchanger for waste heat recovery, it enables the production of hot water, which is subsequently utilized to drive the LiBr-H_2O absorption chiller .In the case where the mass flow rate of hot water (at 70°C and 1 bar) is increased from 0.3 to 2.0 kg/sec, the COP exhibits a continuous improvement from 0.3 to 0.67. This implies that a higher flow rate of hot water positively influences the efficiency of the LiBr-H_2O absorption chiller, leading to an enhanced COP value. as seen in Figure 5.11(a). Like the effect of mass flow rate, increasing inlet temperature which is varied from 80 to 125 °C (mass flow rate of 1 kg/sec) can enhance the COP as shown in Figure 5.11(b). This is because the temperature is a driving force for heat transfer of heat and steam to generator in LiBr-H_2O absorption chiller [30-31].

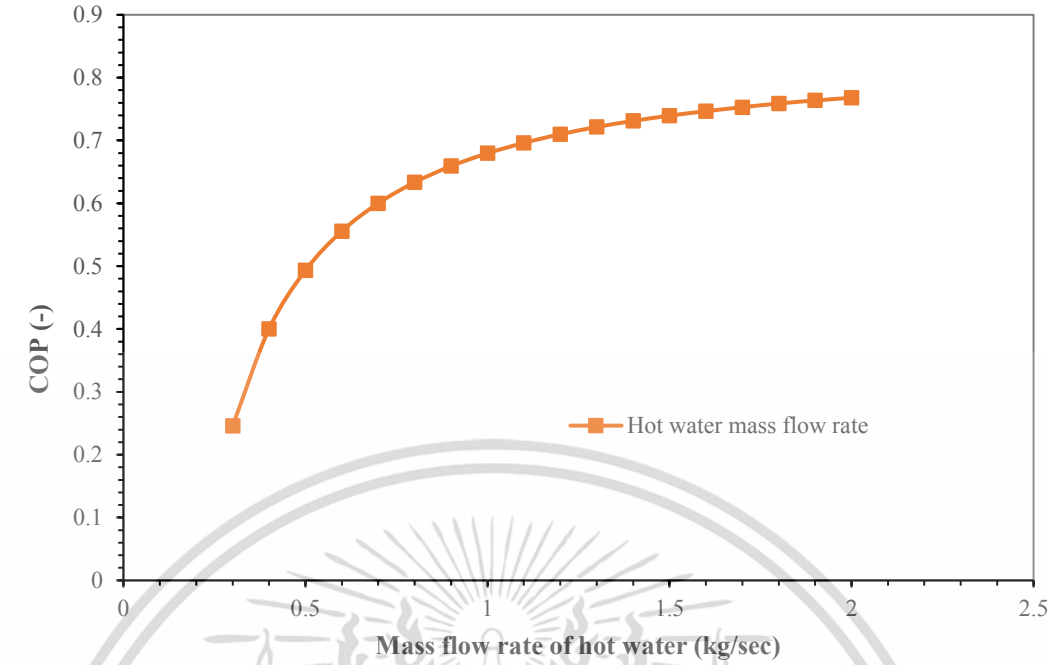

(a)

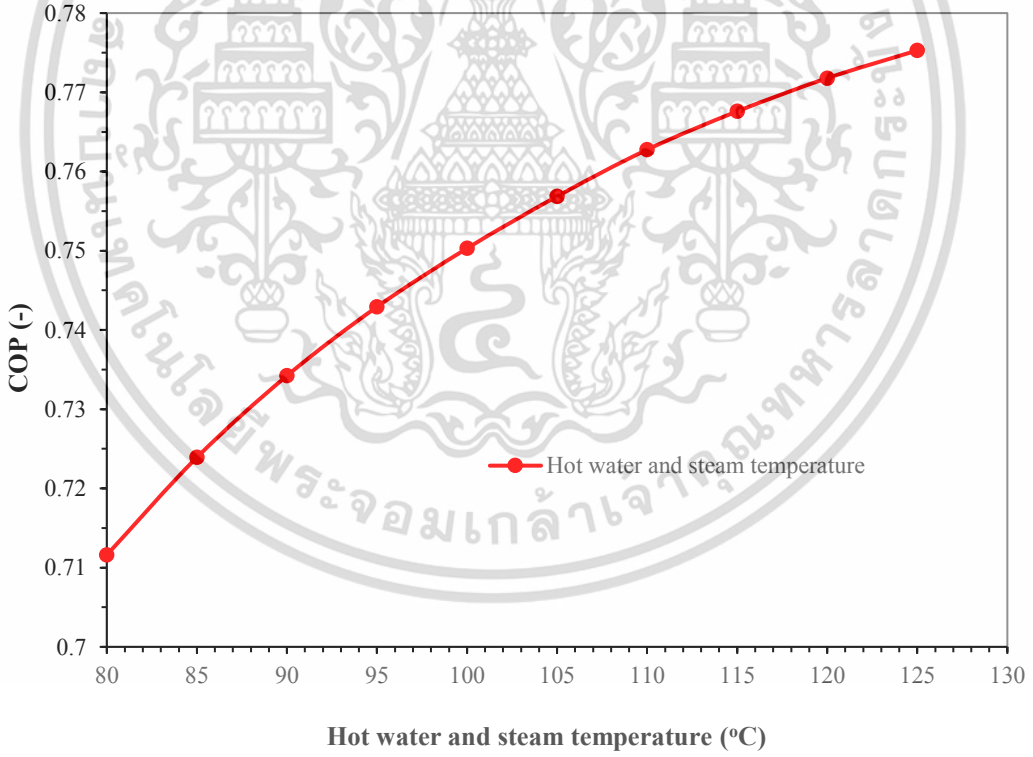

(b)

Figure 5.11 Effect of (a) hot water mass flow rate, (b) hot water inlet temperature on LiBr-H_2O absorption chiller performance.

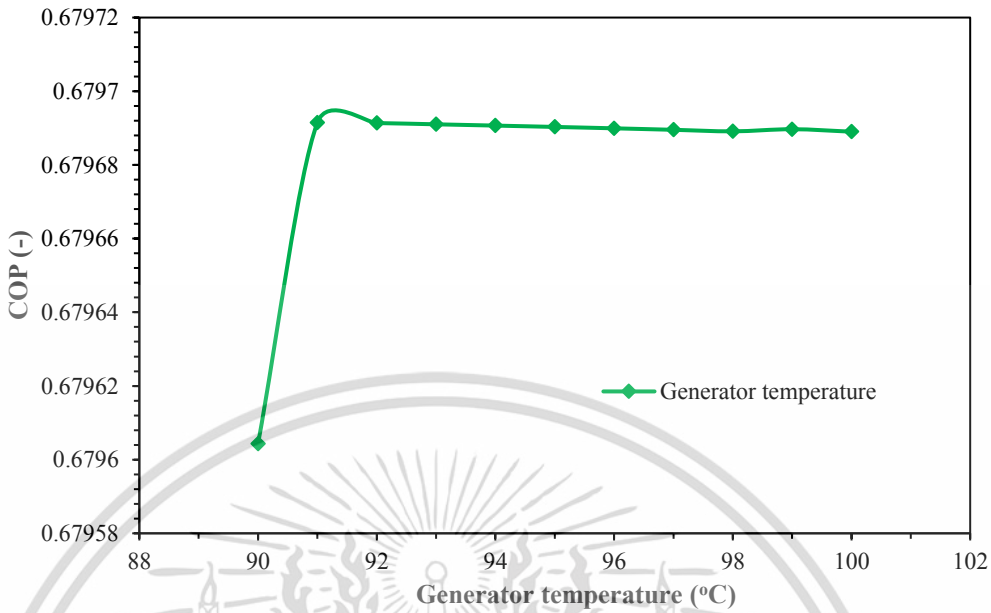

Figure 5.12 Effect of generator temperature on LiBr-H_2O absorption chiller performance.

5.3.2 Effect of generator temperature

Next, the investigation of COP at different generator temperatures between 90 -100 °C is shown in Figure 5.12. The generator unit serves as the heat source in the thermodynamic cycle of the absorption refrigeration system. The simulation results reveal that increasing the generator temperature leads to higher values of the Coefficient of Performance (COP) for the refrigeration system. This indicates that the efficiency of the absorption refrigeration system can be improved by raising the generator temperature.

5.3.3 Effect of evaporator temperature

Finally, the influence of evaporator temperature on COP is investigated as demonstrated in Figure 5.13. The evaporator unit plays a crucial role in generating cooling load, where air or water can pass through a coil to be cooled down for air conditioning purposes. In the case of the LiBr-H_2O system, maintaining the evaporator temperature above 0°C is essential to prevent water from freezing. The simulation results demonstrate that an increase in the evaporator temperature leads to an

enhancement in the COP performance of the absorption refrigeration system. Specifically, when the evaporator temperature varies within the range of 1-10°C, the COP can be improved by approximately 0.72%. This indicates that optimizing the evaporator temperature can positively impact the overall efficiency of the absorption refrigeration system.

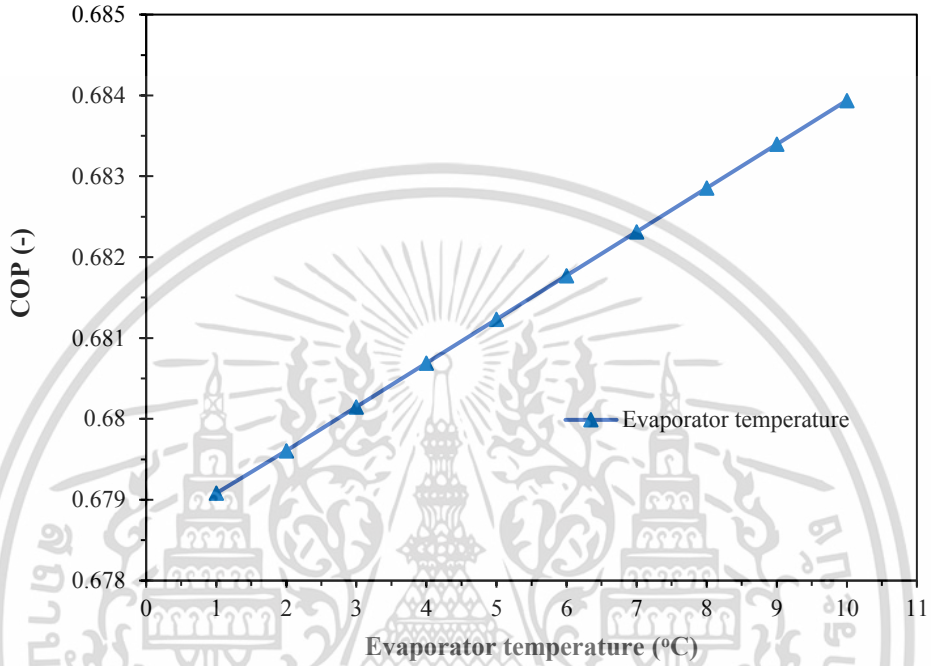

Figure 5.13 Effect of evaporator temperature on LiBr-H_2O absorption chiller performance.

5.4 Optimization trigeneration process consisting of proton conducting SOFC-H and LiBr absorption chiller

In this section, the effects of operating conditions in SOFC-H^+ and LiBr absorption chiller on all performances are studied based on a method of DOE. Since this work focuses on the integrated system of SOFC-H^+ and LiBr absorption chiller, DOE is separately performed.

5.4.1 SOFC-H^+ operation

Based on the simulation results presented in Section 5.2, it is evident that increasing the temperature and fuel utilization enhances the performance of the SOFC-

H^+. The optimal operating conditions are determined as 700 °C for temperature and 0.8 for fuel utilization. However, the effects of A/F molar ratio and pressure on the performance are not clearly defined. Therefore, the parameters selected for investigation on electrical efficiency (Eq. (3.18)) and overall efficiency (Eq. (3.17)) consist of (A) A/F molar ratio and (B) operating pressure. From the investigation in Section 5.2, the operating pressure in a range of 1 and 10 bar is determined while the selection of A/F molar ratio is between 2 and 2.33 to satisfy the maximum specific enthalpy flow. It is noted that A/F molar ratio of 2 refers to air flow rate of 2 kmol/hr and fuel flow rate of 1 kmol/hr whereas A/F molar ratio of 2.33 means that the air flow rate is 7 kmol/hr and fuel flow rate is 3 kmol/hr. To determine the optimal value of A/F molar ratio and SOFC pressure, a full factorial design is employed, considering 2 factors with 2 levels, resulting in a total of 4 experimental runs as listed in Table 5.1. The results of electrical efficiency and overall efficiency are based on the energy input, energy output, electrical efficiency, overall system efficiency, waste heat, and heat utility consumption which is provided in Table 5.2.

Table 5.1 The response results from the 2^2 factorial experimental design of integrated system when the results of SOFC-H^+ are simulated through Aspen Plus V10

Run	A/F molar ratio (-) [A]	Operating pressure (bar) [B]	Electrical efficiency (%)	Overall system efficiency (%)
1	2	10	61.58	93.34
2	2.33	1	58.17	73.61
3	2.33	10	46.38	77.30
4	2	1	73.74	89.61

Code variable:

-1 (Low) A/F molar ratio = 2.00 and Operating pressure = 1

+1 (High) A/F molar ratio = 2.33 and Operating pressure = 10

Table 5.2 Summary of power generation, waste heat, compressor consumption energy input, and heat utility consumption

Air to fuel mole ratio	Pressure	Power generation	Waste heat	Input energy based on LHV H_2	Compressor consumption	Heat Utility (Preheat feed)
(-)	(bar)	(kW)	(kW)	(kW)	(kW)	(kW)
2	10	40.70	18.76	52.52	8.3564	2.08
2.33	1	109.40	43.35	188.06	0	14.31
2.33	10	116.48	65.45	188.06	29.2497	7.31
2	1	38.73	12.432	52.52	0	4.10

The ANOVA statistical analysis of the results obtaining with a confidence level of 95% or p-value equals to 0.05 are summarized in Tables 5.3 and 5.4. The analysis reveals that the variations in A/F molar ratio and pressure have significant impacts on both electrical efficiency and overall system efficiency, supported by the p-values being less than 0.05.

Table 5.3 The analysis of variance (ANOVA) when the response variable is electrical efficiency (%)

Source	Sum of Squares	df	Mean Square	F-value	p-value
Model	380.10	2	190.05	5298.97	0.0097
A	143.38	1	143.38	3997.56	0.0101
B	236.73	1	236.73	6600.37	0.0078
Residual	0.0359	1	0.0359		
Cor Total	380.14	3			
Std. Dev.	0.1894		R^2	0.9999	
Mean	59.97		Adjusted R^2	0.9997	
C.V. %	0.3158		Predicted R^2	0.9985	
			Adeq. Precision	166.8184	

Table 5.4 The analysis of variance (ANOVA) when the response variable is overall efficiency (%)

Source	Sum of Squares	df	Mean Square	F-value	p-value
Model	270.47	2	135.23	2.132E+05	0.0015
A	13.76	1	13.76	21684.95	0.0043
B	256.71	1	256.71	4.046E+05	0.0010
Residual	0.0006	1	0.0006		
Cor Total	270.47	3			
Std. Dev.	0.0252		R^2	0.9999	
Mean	83.47		Adjusted R^2	0.9999	
C.V. %	0.0302		Predicted R^2	0.9999	
			Adeq. Precision	904.5496	

Figures 5.14 and 5.15 illustrate the electrical efficiency and system efficiency as functions of A/F molar ratio and pressure. The results demonstrate a negative effect on electrical efficiency when pressure is increased from 1 to 10 bar, as well as when the A/F ratio is increased from 2 to 2.33. This decline in electrical efficiency is primarily attributed to the increased power consumption of the compressor at higher pressures and A/F ratios. The response surface plot depicted in Figure 5.16 indicates that the maximum electrical efficiency of the SOFC-H^+ system reaches 73.74% when operated at 1 bar with an A/F molar ratio of 2. Regarding the overall system efficiency (Figure 5.17), the analysis shows that an increase in the A/F molar ratio (A) results in a decrease in the overall system efficiency. Although raising the A/F molar ratio can enhance thermal and electrical energy outputs, it also necessitates higher compressor power consumption, thus leading to a reduction in overall system efficiency. The response surface plot displayed in Figure 5.17 reveals that the maximum overall system efficiency for the SOFC-H^+ system is achieved at 93.34% when the operating pressure and A/F molar ratio are set to 10 and 2, respectively.

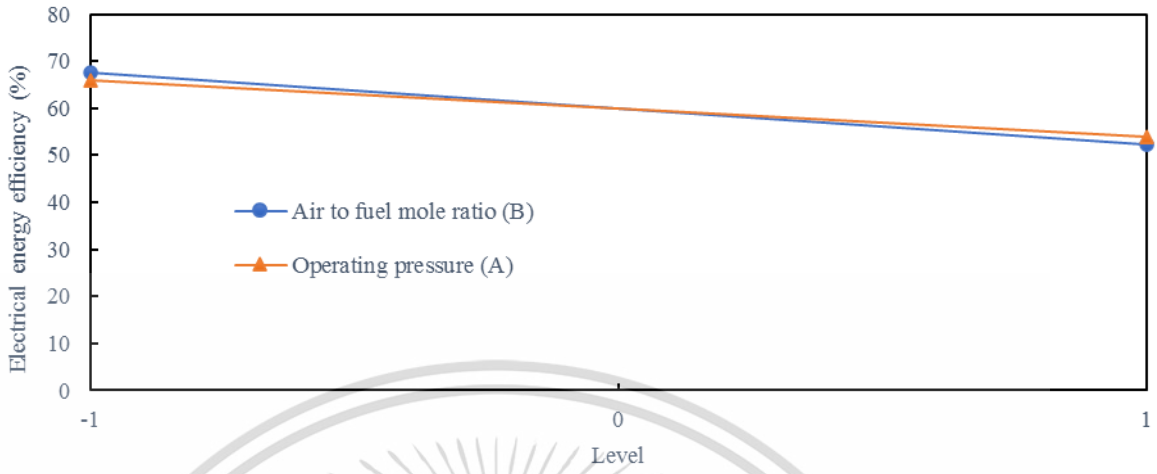

Figure 5.14 Effect of main factor on electricity energy efficicency of SOFC-H$^+$.

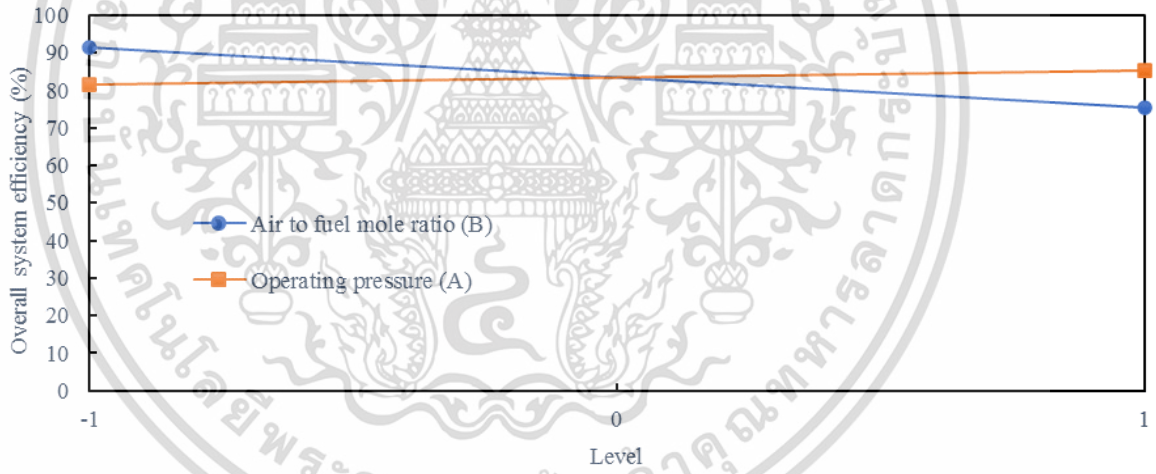

Figure 5.15 Effect of main factor on on overall system efficicency of SOFC-H$^+$.

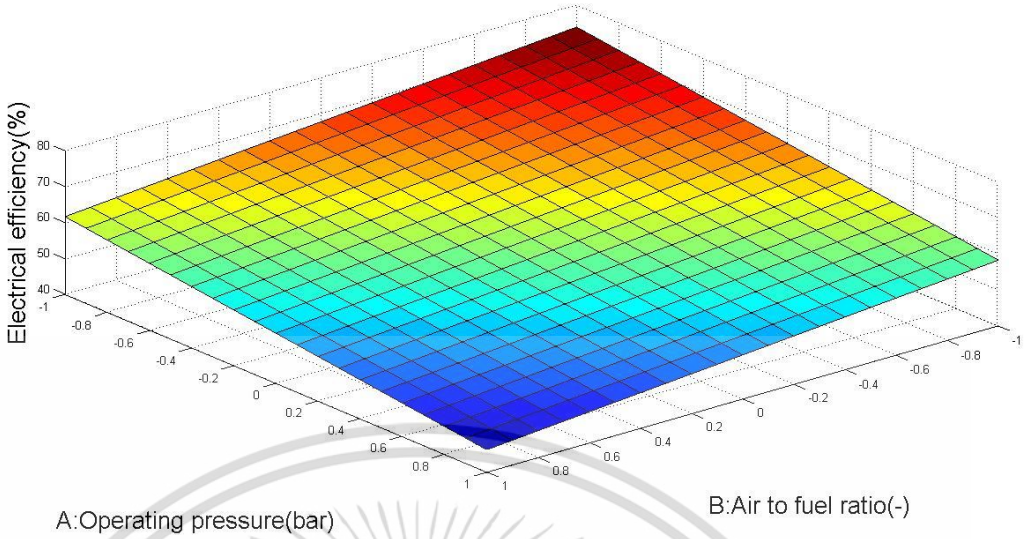

Figure 5.16 Response surface plot of each factor on electrical energy efficiency.

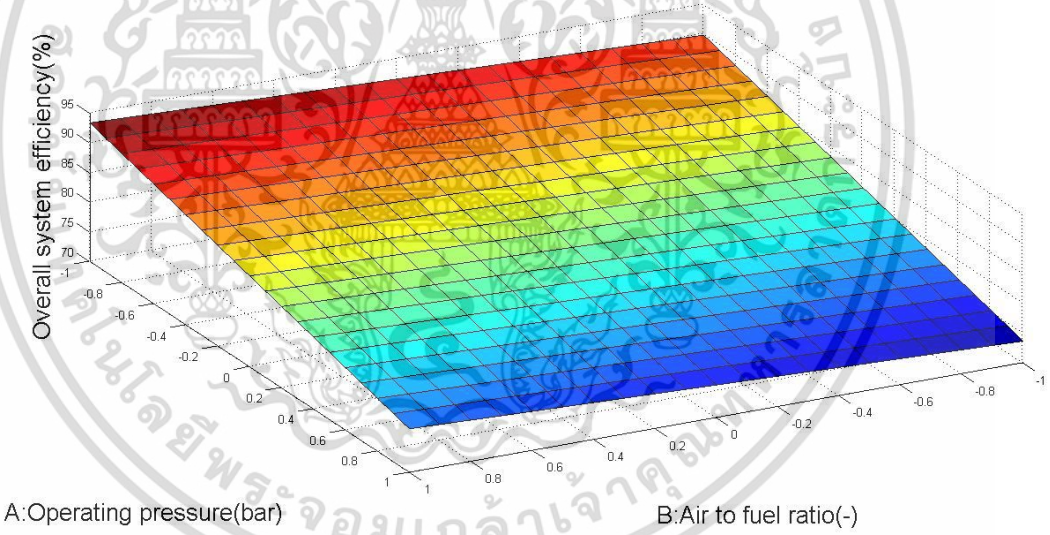

Figure 5.17 Response surface plot of each factor on overall system efficiency.

5.4.2 LiBr absorption chiller operation

For the LiBr absorption chiller, the process parameters as (D) evaporator temperature (E) generator temperature (F) hot water mass flow rate and (G) hot water temperature inlet are selected. The full factorial design of 4 factors with 2 levels leads to 16 experimental runs with a single replicate as shown in Table 5.5

Table 5.5 The response results from the 2^4 factorial experimental design of integrated system when the results of LiBr absorption chiller are simulated through Aspen Plus V10

Run	Generator temperature (°C) [D]	Evaporator temperature (°C) [E]	Hot water mass flow rate (kg/sec) [F]	Inlet hot temperature (°C) [G]	COP (-)
1	90	1	0.04	100	0.7238
2	100	10	0.01	90	0.2191
3	90	10	0.04	100	0.7288
4	100	10	0.04	100	0.7288
5	90	1	0.01	90	0.2180
6	100	1	0.01	90	0.2178
7	90	1	0.01	100	0.3042
8	100	1	0.04	90	0.7028
9	100	10	0.04	90	0.7077
10	90	1	0.04	90	0.7027
11	90	10	0.01	90	0.2196
12	90	10	0.01	100	0.3064
13	90	10	0.04	90	0.7077
14	100	10	0.01	100	0.3062
15	100	1	0.04	100	0.7238
16	100	1	0.01	100	0.3042

Code variable: -1 (Low): Generator temperature = 90 °C, Evaporator temperature = 1 °C, Hot water mass flow rater = 0.01 kg/sec, Inlet hot water temperature = 90 °C

+1(High): Generator temperature = 100 °C, Evaporator temperature = 10 °C, Hot water mass flow rater = 0.04 kg/sec, Inlet hot water temperature = 100°C

Table 5.6 The analysis of variance (ANOVA) when the response variable is COP

Source	Sum of Squares	df	Mean Square	F-value	p-value
Model	0.8398	3	0.2799	59986.08	< 0.0001
F	0.8239	1	0.8239	1.766E+05	< 0.0001
G	0.0116	1	0.0116	2485.69	< 0.0001
FG	0.0043	1	0.0043	919.41	< 0.0001
Residual	0.0001	12	4.66E-06		
Cor Total	0.8398	15			
Std. Dev.	0.0022		R^2	0.999	
Mean	0.4889		Adjusted R^2	0.999	
C.V. %	0.4419		Predicted R^2	0.999	
			Adeq. Precision	470.0390	

Table 5.6 presents a summary of the ANOVA statistical analysis conducted with a confidence level of 95%. In terms of the COP response, the linear model includes the hot water temperature and mass flow rate as significant variables, along with the interaction between hot water temperature and mass flow rate, indicated by a p-value of less than 0.05. This suggests that these variables have a significant impact on the COP value. The response surface plot depicted in Figure 5.18 demonstrates that the hot water temperature has a greater influence on COP compared to the mass flow rate. Increasing the hot water temperature from 90°C to 100°C and the mass flow rate

from 0.01 to 0.04 kg/s results in an increase in the COP value from 0.26 to 0.71. Furthermore, Figure 5.19 illustrates that the LiBr absorption chiller achieves a COP of 0.7238 under specific operating conditions. These conditions include a generator temperature of 90°C, an evaporator temperature of 1°C, a hot water mass flow rate of 0.04 kg/s, and an inlet hot water temperature of 100°C.

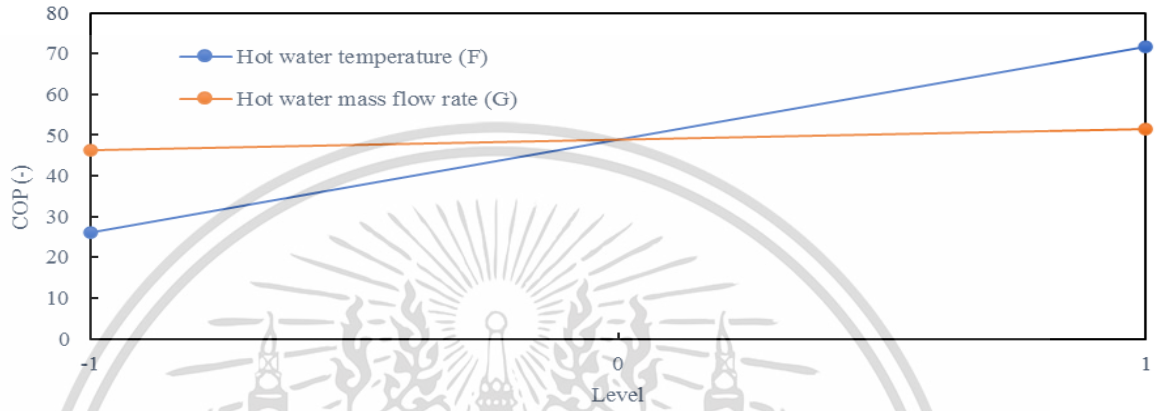

Figure 5.18 Effect of main factor on COP.

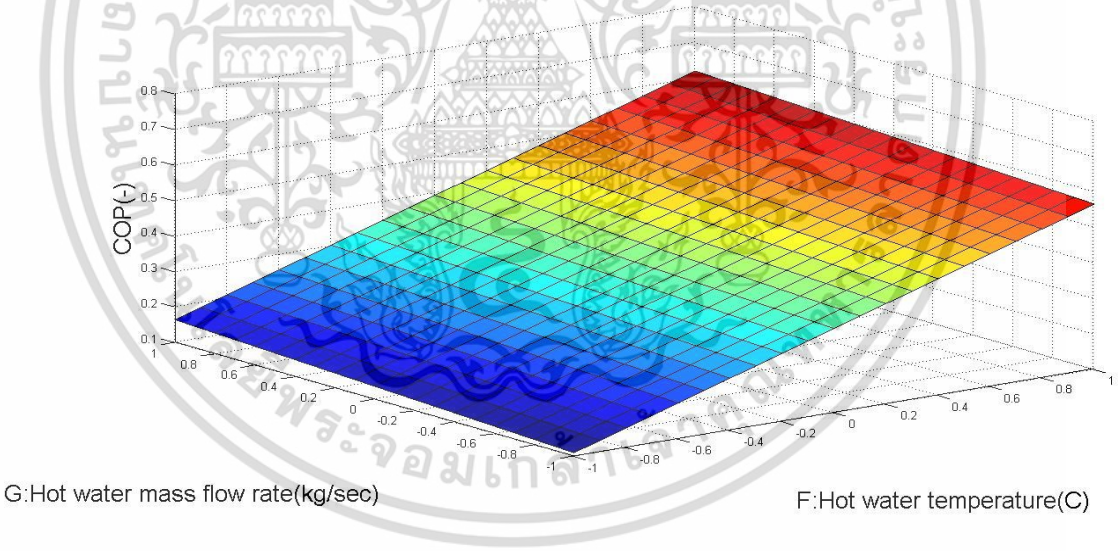

Figure 5.19 Response surface plot of each factor on COP.

From the optimization, the maximum electrical efficiency of SOFC-H^+ (73.74%) can be provided when the SOFC-H^+ is operated at 1 bar with A/F molar ratio of 2. Considering the overall system efficiency, the results indicate that the SOFC-H^+ operated at A/F molar ratio of 2 and pressure of 10 bar can provide the overall efficiency of 93.34%.

For LiBr absorption chiller, sensitivity analysis was conducted to investigate the effect of operating parameters on the COP value of the LiBr absorption chiller. It was found that increasing the hot water mass flow rate, hot water temperature, generator temperature, and evaporator temperature significantly influenced the COP value. The optimization results indicated that the absorption chiller achieved a COP of 0.7238 when operated with a generator temperature of 90°C, an evaporator temperature of 1°C, a hot water mass flow rate of 0.04 kg/sec, and an inlet hot water temperature of 100°C. Table 5.7 shows summary of the optimal operating conditions used in the trigeneration process and results obtained from the study.

Table 5.7 Summary of parameters in the trigeneration process consisting of proton-conducting SOFC and LiBr absorption chiller

Parameter	Values
SOFC-H^+	
Air mass flow rate (kg/hr)	2
Hydrogen mass flow rate (kg/hr)	1
Fuel utilization (-)	0.8
Operating pressure (bar)	10
Operating temperature(°C)	700
Power generation of SOFC-H^+ (kW)	40.70
Compressor power consumption (kW)	8.36
Heat duty of waste heat stream (kJ/hr)	18.76
Heat duty of preheater unit (kJ/hr)	2.08
Electrical efficiency (%)	61.58
Overall efficiency (%)	93.34
LiBr absorption chiller	
Generator temperature of (°C)	90
Evaporator temperature of (°C)	1
Inlet hot water temperature (°C)	100
Hot water mass flow rate (kg/sec)	0.04
COP (-)	0.7238

5.5 Energy and Exergy analysis

In the trigeneration process consisting of SOFC-H^+ and LiBr absorption chiller, it needs to use heat and cold utility in each unit such as preheat feed input stream therefore thermodynamic efficiency is important to indicate the thermal performance of SOFC-H^+ and LiBr absorption chiller. Table 5.8 lists the exergy efficiency of each unit used in trigeneration process and overview process operated under the optimal operating conditions. Finally, Figure 5.20 shows the energy and exergy efficiencies of the SOFC-H^+ unit, SOFC-H^+-CHP system, absorption chiller, and trigeneration process were analyzed. Based on the simulation results, it was found that the SOFC-H^+-CHP system exhibited the highest energy and exergy efficiencies, achieving values of 87.34% and 56.93% respectively. The trigeneration process ranked second with energy and exergy efficiencies of 79.31% and 56.06% respectively.

Table 5.8 The exergy efficiency of each unit used in trigeneration process and overview process.

Equipment	Exergy outlet (kW)	Exergy inlet (kW)	Exergy efficiency (%)
Absorber	6.425	5.864	91.27
Generator	7.138	6.339	88.80
LiBr absorption chiller	0.8502	4.647	18.29
SOFC-H^+ CHP	36.706	63.56	57.74
SOFC-H^+	35.88	63.56	55.97

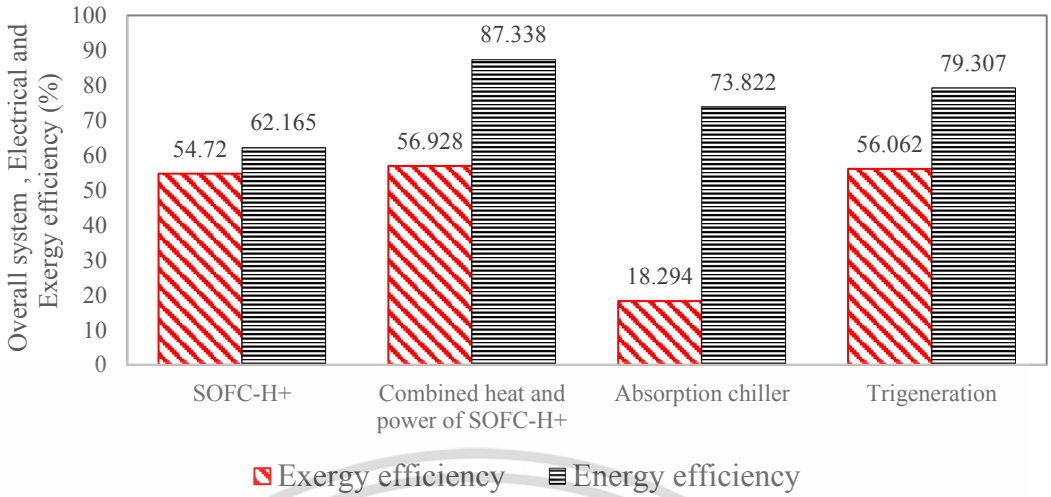

Figure 5.20 Energy and exergy efficiencies of the SOFC-H^+ unit, SOFC-H^+-CHP, absorption chiller and trigeneration process.

CHAPTER VI

CONCLUSION

6.1 Conclusion

This work presents the performance analysis and optimization of two integrated processes that include (1) co-gasification of coal and biomass integrated with calcium looping carbon dioxide capture process, and (2) trigeneration process consisting of SOFC-H^+ and LiBr absorption chiller. The performance analysis was performed through the simulation by using Aspen Plus simulator version 10. When the trend of results was known, the optimization was performed by using Design Expert version 11. Findings of this study obtained from each part can be concluded as follows:

6.1.1 Co-gasification of coal and biomass integrated with calcium looping carbon dioxide capture process

In this part, the co-gasification of biomass and coal integrated with the calcium looping carbon dioxide capture process was investigated to produce purified hydrogen. In the gasification process, the influences of the gasifier temperature and S/F mass on the production of hydrogen were investigated. The simulation results indicated that the mole fraction of hydrogen can be enhanced with increasing gasifier temperature and S/F mass ratio. In the case of carbon dioxide capture process, the amount and purity of hydrogen were considered with wider range of CaO/F mass ratio, carbonator temperature, and regenerator temperature. From the simulation, it was found that the operating conditions in adsorber must be carefully determined to provide suitable hydrogen production.

When the optimization was performed, the results revealed that the optimal operating conditions of co-gasification were at a gasifier temperature of 700 °C with an S/F mass ratio of 2 and a C/B mass ratio of 0.75:0.25, while the optimal operating conditions of carbon dioxide capture process were at a carbonator temperature of 450 °C, a regenerator temperature of 950 °C with a CaO/F mass ratio of 3. Under these

operating conditions, the maximum amount of hydrogen of 99.59 %vol. and carbon dioxide capture efficiency of 99.99% can be provided. Considering the energy analysis, the results indicated that the energy efficiency of the co-gasification process is 42.86%

6.1.2 Trigeneration process consisting of SOFC-H^+ and LiBr absorption chiller

In this part, the performance analysis and optimization of the trigeneration process consisting of the SOFC-H^+ and the Li-Br absorption chiller was presented. The impact of the operating conditions of the SOFC-H^+ (i.e., operating pressure, operating temperature, fuel utilization and A/F molar ratio) on system efficiency were examined. The power density of SOFC-H^+ can be improved with increasing pressure and temperature of the SOFC-H^+ and fuel utilization. However, an enhancement of fuel utilization causes a decrease in cell voltage. The sensitivity analysis confirmed that the optimal operating conditions of SOFC-H^+ were at 700°C with fuel utilization of 0.8 while optimal operating conditions of other parameters, that include pressure and A/F molar ratio, must be carefully selected to compromise cell voltage and power density. When the optimization was performed, the results indicated that at an A/F molar ratio of 2 and pressure of 10 bar are the optimal values. Under these optimal operating conditions, an overall efficiency of 93.34% can be obtained.

For the LiBr absorption chiller, the variations of the hot water mass flow rate, hot water and steam inlet temperature, evaporator temperature and generator temperature on the COP value were considered. The sensitivity analysis of LiBr absorption chiller revealed that increasing the hot water mass flow rate, hot water temperature, generator temperature and evaporator temperature cause an increase in COP. When the optimization was performed, it was found that the absorption chiller should be operated at a generator temperature of 90 °C, an evaporator temperature of 1 °C, a hot water mass flow rate of 0.04 kg/sec and an inlet hot water temperature of 100 °C. Under these optimal operating conditions, a COP of 0.7238 can be provided. Considering energy and exergy analysis, the revealed that the SOFC-H^+-CHP has the highest energy (87.34%) and exergy (56.93%) efficiencies, followed by the trigeneration process, providing the energy (79.31%) and exergy (56.06%) efficiencies.

6.2 Recommendations

- Carbon foot print analysis of both integrated processes should be considered.
- Heat exchanger network should be performed to improve energy efficiency of both integrated processes.
- In a gasification process, tar formation should be included.
- In a SOFC-H^+, the internal current, cross-over issue and current leakage should be included in the electrochemical model.
- From a study on trigeneration process, it can develop and extend to polygeneration process.

REFERENCES

[1] Singh, S. B., & De, M. (2020). Thermally exfoliated graphene oxide for hydrogen storage. Materials Chemistry and Physics, 239, 122102.

[2] Prestipino, M., Piccolo, A., Polito, M. F., & Galvagno, A. (2022). Combined Bio-Hydrogen, Heat, and Power Production Based on Residual Biomass Gasification: Energy, Exergy, and Renewability Assessment of an Alternative Process Configuration. Energies, 15(15), 5524.

[3] Ulejczyk, B., Jóźwik, P., Nogal, Ł., Młotek, M., & Krawczyk, K. (2022). Efficient Conversion of Ethanol to Hydrogen in a Hybrid Plasma-Catalytic Reactor. Energies, 15(9), 3050.

[4] Matus, E., Sukhova, O., Ismagilov, I., Kerzhentsev, M., Stonkus, O., & Ismagilov, Z. (2021). Hydrogen Production through Autothermal Reforming of Ethanol: Enhancement of Ni Catalyst Performance via Promotion. Energies, 14(16), 5176.

[5] Lin, K.-W., & Wu, H.-W. (2019). Thermodynamic analysis and experimental study of partial oxidation reforming of biodiesel and hydrotreated vegetable oil for hydrogen-rich syngas production. Fuel, 236, 1146-1155.

[6] Rekleitis, G., Haralambous, K.-J., Loizidou, M., & Aravossis, K. (2020). Utilization of Agricultural and Livestock Waste in Anaerobic Digestion (A.D): Applying the Biorefinery Concept in a Circular Economy. Energies, 13(17), 4428.

[7] Fernandez-Lopez, M., Pedroche, J., Valverde, J. L., & Sanchez-Silva, L. (2017). Simulation of the gasification of animal wastes in a dual gasifier using Aspen Plus®. Energy Conversion and Management, 140, 211-217.

[8] Shen, Y., Li, X., Yao, Z., Cui, X., & Wang, C. (2019). CO_2 gasification of woody biomass: Experimental study from a lab-scale reactor to a small-scale autothermal gasifier. Energy, 170, 497-506.

[9] Gao, N., Śliz, M., Quan, C., Bieniek, A., & Magdziarz, A. (2021). Biomass CO_2 gasification with CaO looping for syngas production in a fixed-bed reactor. Renewable Energy, 167, 652-661.

[10] Shahabuddin, M., & Bhattacharya, S. (2021). Co-Gasification Characteristics of Coal and Biomass Using CO_2 Reactant under Thermodynamic Equilibrium Modelling. Energies, 14(21), 7384.

[11] Hu, J., Shao, J., Yang, H., Lin, G., Chen, Y., Wang, X., Zhang, W., & Chen, H. (2017). Co-gasification of coal and biomass: Synergy, characterization and reactivity of the residual char. Bioresource Technology, 244, 1-7.

[12] Seçer, A., Fakı, E., Türker Üzden, Ş., & Hasanoğlu, A. (2020). Hydrothermal co-gasification of sorghum biomass and çan lignite in mild conditions: An optimization study for high yield hydrogen production. International Journal of Hydrogen Energy, 45(4), 2668-2680.

[13] Teixeira, P., Bacariza, C., Correia, P., Pinheiro, C. I. C., & Cabrita, I. (2022). Hydrogen Production with In Situ CO_2 Capture at High and Medium Temperatures Using Solid Sorbents. Energies, 15(11), 4039.

[14] Wang, Y., Li, Y., Yang, L., Fan, X., & Chu, L. (2022). Revealing the effects of Ni on sorption-enhanced water-gas shift reaction of CaO for H_2 production by density functional theory. Process Safety and Environmental Protection, 157, 254-265.

[15] Roshan Kumar, T., Mattisson, T., Rydén, M., & Stenberg, V. (2022). Process Analysis of Chemical Looping Gasification of Biomass for Fischer–Tropsch Crude Production with Net-Negative CO_2 Emissions: Part 1. Energy & Fuels, 36(17), 9687-9705.

[16] Li, F., Zeng, L., Velazquez-Vargas, L. G., Yoscovits, Z., & Fan, L.-S. (2010). Syngas chemical looping gasification process: Bench-scale studies and reactor simulations. AIChE Journal, 56(8), 2186-219.

[17] Liu, L., Cao, Y., Ma, D., Liu, Q., & Yang, J. (2017). Process simulation of coal-direct chemical looping gasification for syngas production. RSC Advances, 7(87), 55450-55458.

[18] Ahmed, K., & F**Ö**ger, K. (2017). Analysis of equilibrium and kinetic models of internal reforming on solid oxide fuel cell anodes: Effect on voltage, current and temperature distribution. Journal of Power Sources, 343, 83-93.

[19] Teramoto, K., Iwai, H., Kishimoto, M., Kawaguchi, T., Takemoto, M., Saito, M., & Yoshida, H. (2020). Direct reforming of Methane–Ammonia mixed fuel on Ni–YSZ anode of solid oxide fuel cells. International Journal of Hydrogen Energy, 45(15), 8965-8974.

[20] Powell, M., Meinhardt, K., Sprenkle, V., Chick, L., & McVay, G. (2012). Demonstration of a highly efficient solid oxide fuel cell power system using

adiabatic steam reforming and anode gas recirculation. Journal of Power Sources, 205, 377-384.

[21] Liu, M., Gao, J., Liu, X., & Meng, G. (2011). High performance of anode supported $BaZr_{0.1}Ce_{0.7}Y_{0.2}O_{3-\delta}$ (BZCY) electrolyte cell for IT-SOFC. International Journal of Hydrogen Energy, 36(21), 13741-13745.

[22] Chen, X., Zhang, H., Li, Y., Xing, J., Zhang, Z., Ding, X., Zhang, B., Zhou, J., & Wang, S. (2021). Fabrication and performance of anode-supported proton conducting solid oxide fuel cells based on $BaZr_{0.1}Ce_{0.7}Y_{0.1}Yb_{0.1}O_{3-\delta}$ electrolyte by multi-layer aqueous-based co-tape casting. Journal of Power Sources, 506, 229922.

[23] Xie, D., Ling, A., Yan, D., Jia, L., Chi, B., Pu, J., & Li, J. (2020). A comparative study on the composite cathodes with proton conductor and oxygen ion conductor for proton-conducting solid oxide fuel cell. Electrochimica Acta, 344, 136143.

[24] Wang, D., Xia, Y., Lv, H., Miao, L., Bi, L., & Liu, W. (2020). $PrBaCo_{2-x}Ta_xO_{5+\delta}$ based composite materials as cathodes for proton-conducting solid oxide fuel cells with high CO_2 resistance. International Journal of Hydrogen Energy, 45(55), 31017-31026.

[25] Abdul Malik, L., Mahmud, N. A., Mohd Affandi, N. S., Mazlan, N. W., Zakaria, N. H. A., Abd Malek, N. I., Hassan, O. H., Md Jani, A. M., & Osman, N. (2021). Effect of nickel oxide - Modified $BaCe_{0.54}Zr_{0.36}Y_{0.1}O_{2.95}$ as composite anode on the performance of proton-conducting solid oxide fuel cell. International Journal of Hydrogen Energy, 46(8), 5963-5974.

[26] Wei, Z., Wang, J., Yu, X., Li, Z., Zhao, Y., & Chai, J. (2021). Study on Ce and Y co-doped $BaFeO_{3-\delta}$ cubic perovskite as free-cobalt cathode for proton-conducting solid oxide fuel cells. International Journal of Hydrogen Energy, 46(46), 23868-23878.

[27] Patcharavorachot, Y., Paengjuntuek, W., Assabumrungrat, S., & Arpornwichanop, A. (2010). Performance evaluation of combined solid oxide fuel cells with different electrolytes. International Journal of Hydrogen Energy, 35(9), 4301-4310.

[28] Ni, M. (2013). The effect of electrolyte type on performance of solid oxide fuel cells running on hydrocarbon fuels. International Journal of Hydrogen Energy, 38(6), 2846-2858.

[29] Kumuk, B., Asmare Alemu, M., & Ilbas, M. (2022). Investigation of the effect of ion transition type on performance in solid oxide fuel cells fueled hydrogen and coal gas. International Journal of Hydrogen Energy, 47(5), 3409-3415.

[30] Liu, D., Fan, X., Li, Z., Liu, T., Sun, M., Qian, C., Ling, M., Liu, Y., & Liang, C. (2019). A cation/anion co-doped $Li_{1.12}Na_{0.08}Ni_{0.2}Mn_{0.6}O_{1.95}F_{0.05}$ cathode for lithium ion batteries. Nano Energy, 58, 786-796.

[31] Ozcan, H., & Dincer, I. (2015). Performance evaluation of an SOFC based trigeneration system using various gaseous fuels from biomass gasification. International Journal of Hydrogen Energy, 40(24), 7798-7807.

[32] Pandya, B., El-Kharouf, A., Venkataraman, V., & Steinberger-Wilckens, R. (2020). Comparative study of solid oxide fuel cell coupled absorption refrigeration system for green and sustainable refrigerated transportation. Applied Thermal Engineering, 179, 115597.

[33] Gwak, G., Kim, M., Kim, D., Faizan, M., Oh, K., Lee, J., Choi, J., Lee, N., Lim, K., & Ju, H. (2019). Performance and Efficiency Analysis of an HT-PEMFC System with an Absorption Chiller for Tri-Generation Applications. Energies, 12(5), 905.

[34] Katsaros, G., Nguyen, T.-V., & Rokni, M. (2017). Tri-generation System based on Municipal Waste Gasification, Fuel Cell and an Absorption Chiller. Journal of Sustainable Development of Energy, Water and Environment Systems, 6, 13-32.

[35] Shabbar, S., & Janajreh, I. (2013). Thermodynamic equilibrium analysis of coal gasification using Gibbs energy minimization method. Energy Conversion and Management, 65, 755-763.

[36] อมรชัย อาภรณ์วิชานพ “ระบบเซลล์เชื้อเพลิงชนิดออกไซด์ของแข็งสำหรับการผลิตพลังงานไฟฟ้าสะอาด การจำลอง การออกแบบ และการวิเคราะห์” สำนักพิมพ์แห่งจุฬาลงกรณ์มหาวิทยาลัย , 2561

[37] Hu, Y., Cheng, Z., & Zhou, Z. (2021). High-purity H2 production by sorption-enhanced water gas shift on a K_2CO_3-promoted $Cu/MgO–Al_2O_3$ difunctional material [10.1039/D1SE00400J]. Sustainable Energy & Fuels, 5(13), 3340-3350.

[38] Cormos, A.-M., & Simon, A. (2015). Assessment of CO_2 capture by calcium looping (CaL) process in a flexible power plant operation scenario. Applied Thermal Engineering, 80, 319-327.

[39] Saebea, D., Arpornwichanop, A., & Patcharavorachot, Y. (2021). Thermodynamic analysis of a proton conducting SOFC integrated system fuelled by different renewable fuels. International Journal of Hydrogen Energy, 46(20), 11445-11457.

[40] Milewski, J., Szczęśniak, A., & Szablowski, L. (2019). A discussion on mathematical models of proton conducting Solid Oxide Fuel Cells. International Journal of Hydrogen Energy, 44(21), 10925-10932.

[41] Bavarian, M., & Soroush, M. (2012). Mathematical modeling and steady-state analysis of a proton-conducting solid oxide fuel cell. Journal of Process Control, 22(8), 1521-1530.

[42] Huang, X., et al. (2006). Fuel Cell Technology for Distributed Generation: An Overview. 2006 IEEE International Symposium on Industrial Electronics.

[43] Wang, Y., & Feng, X. (2020). Sustainable utilization of low-grade heat: Modeling and case study. In (pp. 171-197). https://doi.org/10.1016/B978-0-12-818376-2.00007-7

[44] Montgomery, D.C. Design and Analysis of Experiments, 5th ed.; John Wiley & Sons Ltd.: New York, NY, USA, 2001.

[45] Somers, C., Mortazavi, A., Hwang, Y., Radermacher, R., Rodgers, P., & Al-Hashimi, S. (2011). Modeling water/lithium bromide absorption chillers in ASPEN Plus. Applied Energy, 88(11), 4197-4205.

[46] Xiang, D., Huang, W., Cai, M., Cao, Y., Li, P., & Shu, R. (2019). Process modeling, simulation, and technical analysis of coke-oven gas solid oxide fuel cell integrated with anode off-gas recirculation and CLC for power generation. Energy Conversion and Management, 190, 34-41.

[47] Arteaga-Pérez, L. E., Casas-Ledón, Y., Pérez-Bermúdez, R., Peralta, L. M., Dewulf, J., & Prins, W. (2013). Energy and exergy analysis of a sugar cane bagasse gasifier integrated to a solid oxide fuel cell based on a quasi-equilibrium approach. Chemical Engineering Journal, 228, 1121-1132.

[48] Mehrpooya, M., Khalili, M., & Sharifzadeh, M. M. M. (2018). Model development and energy and exergy analysis of the biomass gasification process (Based on the various biomass sources). Renewable and Sustainable Energy Reviews, 91, 869-887.

[49] Salman, C. A., Naqvi, M., Thorin, E., & Yan, J. (2018). Gasification process integration with existing combined heat and power plants for polygeneration of dimethyl

ether or methanol: A detailed profitability analysis [article]. Applied Energy, 226, 116-128.

[50] Loha, C., Chatterjee, P. K., & Chattopadhyay, H. (2011). Performance of fluidized bed steam gasification of biomass – Modeling and experiment. Energy Conversion and Management, 52(3), 1583-1588.

[51] Minutillo, M., Perna, A., Jannelli, E., Cigolotti, V., Nam, S. W., Yoon, S. P., & Kwon, B. W. (2017). Coupling of Biomass Gasification and SOFC – Gas Turbine Hybrid System for Small Scale Cogeneration Applications. Energy Procedia, 105, 730-737.

[52] Mota, R., Krishnamoorthy, G., Dada, O., & Benson, S. A. (2015). Hydrogen rich syngas production from oxy-steam gasification of a lignite coal – A design and optimization study. Applied Thermal Engineering, 90, 13-22.

[53] Atsonios, K., Zeneli, M., Nikolopoulos, A., Nikolopoulos, N., Grammelis, P., & Kakaras, E. (2015). Calcium looping process simulation based on an advanced thermodynamic model combined with CFD analysis. Fuel, 153, 370-381.

[54] Zhang, J.-H., Lei, L.-B., Liu, D., Zhao, F.-Y., Ni, M., & Chen, F. (2018). Mathematical modeling of a proton-conducting solid oxide fuel cell with current leakage. Journal of Power Sources, 400, 333-340.

[55] Ni, M., Leung, D. Y. C., & Leung, M. K. H. (2008). Modeling of methane fed solid oxide fuel cells: Comparison between proton conducting electrolyte and oxygen ion conducting electrolyte. Journal of Power Sources, 183(1), 133-142.

[56] Nomura, K., & Kageyama, H. (2007). Transport properties of $Ba(Zr_{0.8}Y_{0.2})O_{3-\delta}$ perovskite. Solid State Ionics, 178(7), 661-665.

[57] Herold Keith, Radermacher Reinhard, Klein Sanford. Absorption chillers and heat pumps. 2nd ed. CRC Press; 2016.

[58] American Society of Heating, Refrigerating and Air Conditioning Engineers. 2009 ASHRAE handbook: fundamentals. Atlanta, GA: American Society of Heating, Refrigeration and Air-Conditioning Engineers; 2009.

[59] Asgari, N., Khoshbakhti Saray, R., & Mirmasoumi, S. (2020). Energy and exergy analyses of a novel seasonal CCHP system driven by a gas turbine integrated with a biomass gasification unit and a LiBr-water absorption chiller. Energy Conversion and Management, 220, 113096.

[60] Canbolat, A. S., Bademlioglu, A. H., Arslanoglu, N., & Kaynakli, O. (2019). Performance optimization of absorption refrigeration systems using Taguchi, ANOVA and Grey Relational Analysis methods. Journal of Cleaner Production, 229, 874-885.

[61] Krerkkaiwan, S.; Fushimi, C.; Tsutsumi, A.; Kuchonthara, P. Synergetic effect during copyrolysis/gasification of biomass and sub-bituminous coal. Fuel Process. Technol. 2013, 115, 11–18.

[62] Ongkabin, T. Syngas from Coal and Biomass Gasification Integrated with Combustion in Circulating Fluidized Bed. Master's Thesis, Chulalongkorn University, Krung Thep Maha Nakhon, Thailand, 2017. Available online: http://cuir.car.chula.ac.th/bitstream/123456789/38326/1/Tassanai_on.pdf (accessed on 10 April 2022).

[63] Lei, L., Tao, Z., Hong, T., Wang, X., & Chen, F. (2018). A highly active hybrid catalyst modified $(La_{0.60}Sr_{0.40})_{0.95}Co_{0.20}Fe_{0.80}O_{3-\delta}$ cathode for proton conducting solid oxide fuel cells. Journal of Power Sources, 389, 1-7.

[64] Li, B., Wei, L., Yang, H., Wang, X., & Chen, H. (2014). The enhancing mechanism of calcium oxide on water gas shift reaction for hydrogen production. Energy, 68, 248-254.

APPENDIX

Appendix A

Result of coal/biomass co-gasification integrated with calcium looping carbon dioxide capture process

Data result of Integrated co-gasification of biomass and coal with calcium looping carbon dioxide capture process

Table A.1 Model validation of experimental data and numerical result of biomass gasification process at S/F 1 – 1.7 and gasifier temperature 700 °C and validated with Loha et al. [50]

	Experiment			Simulation		
Steam to feeding biomass ratio (S/F)	1.0	1.32	1.70	1.0	1.32	1.70
Syngas composition (% Volume)						
H_2	49.50	52.30	52.90	56.62	57.98	59.04
CO	23.70	17.75	16.40	19.04	15.42	12.56
CO_2	21.20	22.25	22.90	24.28	26.57	28.38
CH_4	5.60	7.40	7.80	0.06	0.03	0.01

Table A.2 Model validation of experimental data and numerical result of biomass gasification process at gasifier temperature 1,173 K and Air to biomass ratio 1.96 and validated with Mota et al. [52]

	Simulation	Experiment
Steam to feeding biomass ratio (S/F)	1.96	1.96
Syngas composition (% Volume)		
H_2	23.7831	18±2
CO	16.449	19±3
CH_4	0	>3
CO_2	13.9451	10±3
N_2	43.22716	50

Table A.3 Model validation of experimental data and numerical result of biomass gasification process at gasifier temperature 750 °C and oxygen carrier to carbon 1 and validated with Minutillo et al. [51]

	Simulation	Experiment
Syngas composition (% Volume)		
H_2	38.00	39.00
CO	16.00	14.00
CH_4	0.01	2.50
CO_2	36.00	32.0

Table A.4 Effect of gasifier temperature on syngas composition at chemical equilibrium reactor outlet with biomass feeding mass flow rate = 1,000 kg/hr , coal feeding mass flow rate = 1,000 kg/hr and steam to feed (S/F) = 1:1

Gasifier temperature (°C)	500	550	600	650	700	750	800	850	900	950	1,000
Mole fraction											
H_2	45.80	63.00	78.60	87.46	89.35	88.38	86.81	85.23	83.77	82.47	81.29
CO	3.94	8.58	15.10	20.99	24.74	27.22	29.19	30.88	32.36	33.68	34.86
CO_2	33.21	34.03	33.04	30.84	28.50	26.39	24.53	22.86	21.39	20.07	18.90
CH_4	16.60	11.14	5.61	1.92	0.51	0.136	0.039	0.012	0.004	0.0016	0.0006
N_2	0.29	0.29	0.294	0.29	0.29	0.294	0.294	0.294	0.294	0.294	0.294
H_2S	0.132	0.13	0.132	0.13	0.132	0.13	0.132	0.132	0.13	0.132	0.132

Table A.5 Effect of S/F mass ratio on syngas composition at chemical equilibrium reactor outlet with biomass feeding mass flow rate = 1,000 kg/hr , coal feeding mass flow rate = 1,000 kg/hr and gasifier temperature = 700 °C

S/F	0.5	1	1.5	2.0	2.5	3.0	3.5	4.0	4.5	5.0	5.5
Mole fraction											
H_2	58.71	62.43	64.08	65.019	65.61	66.03	66.33	66.57	66.75	66.91	67.03
CO	25.27	17.28	12.96	10.31	8.54	7.28	6.34	5.62	5.04	4.571	4.180
CO_2	14.70	19.91	22.81	24.60	25.80	26.66	27.30	27.79	28.19	28.51	28.78
CH_4	1.30	0.306	0.135	0.061	0.031	0.018	0.011	0.007	0.004	0.003	0.002

Table A.5 (Continue) Effect of S/F mass ratio on syngas composition at chemical equilibrium reactor outlet with biomass feeding mass flow rate = 1,000 kg/hr , coal feeding mass flow rate = 1,000 kg/hr and gasifier temperature = 700 °C

S/F	6.0	6.5	7.0	7.5	8.0	8.5	9.0	9.5	10.0
Mole fraction									
H_2	67.14	67.23	67.30	67.37	67.43	67.47	67.53	67.57	67.61
CO	3.85	3.57	3.32	3.11	2.92	2.76	2.612	2.48	2.36
CO_2	29.00	29.20	29.36	29.51	29.64	29.75	29.85	29.94	30.02
CH_4	0.0017	0.0013	0.0010	0.0079	0.00062	0.0005	0.0004	0.0003	0.0002

Table A.6 Effect of CaO/F ratio on syngas composition at chemical equilibrium reactor outlet with biomass feeding mass flow rate = 1,000 kg/hr , coal feeding mass flow rate = 1,000 kg/hr , gasifier temperature = 700 °C , S/F = 1:1 and carbonator temperature = 450 °C

CaO/F	0.5	1	1.5	2.0	2.5	3.0	3.5	4.0	4.5	5.0	5.5	6.0
Mole fraction												
H_2	73.17	81.87	92.28	99.63	99.63	99.63	99.63	99.63	99.63	99.63	99.63	99.63
CO	6.11	4.40	1.988	0.00	0.00	0.00	0.00	0.00	0.00	0.00	0.00	0.00
CO_2	20.42	13.400	5.38	0.00	0.00	0.000	0.000	0.000	0.000	0.000	0.00	0.00
CH_4	0.00	0.00	0.00	0.00	0.00	0.00	0.00	0.00	0.00	0.00	0.00	0.00

Table A.7 Effect of carbonator temperature on syngas composition at chemical equilibrium reactor outlet with biomass feeding mass flow rate = 1,000 kg/hr , coal feeding mass flow rate = 1,000 kg/hr , gasifier temperature = 700 °C , S/F = 1:1 and calciner temperature = 950 °C

Carbonator temperature (°C)	400	450	500	550	600	650	700	750	800	850	900	950	1,000
Mole fraction													
H_2	99.66	99.63	99.61	99.52	99.07	97.29	91.52	77.11	61.60	61.14	60.72	60.35	60.00
CO	4.84e-05	0.00068	0.0068	0.0509	0.296	1.376	4.95	13.10	20.72	22.15	23.46	24.63	25.73
CO_2	0.000192	0.0017	0.0113	0.060	0.260	0.966	3.17	9.45	17.38	16.40	15.50	14.68	13.95
CH_4	0	0	0	0	0	0	0	0	0	0	0	0	0
N_2	0.252	0.252	0.252	0.252	0.25175	0.249	0.244	0.228	0.208	0.211	0.213	0.215	0.21
H_2S	0.11	0.11	0.114	0.114	0.114	0.112	0.110	0.103	0.094	0.095	0.096	0.097	0.098

Table A. 8 Effect of calciner temperature on syngas composition at chemical equilibrium reactor outlet with biomass feeding mass flow rate = 1,000 kg/hr , coal feeding mass flow rate = 1,000 kg/hr , gasifier temperature = 700 °C , S/F = 1:1 and carbonator temperature = 450 °C

Calciner temperature (°C)	400	500	600	700	800	900	1000	1,100	1,200	1,300
Mole flowrate (kmol/hr)										
CO_2 at reactor exit	0	0	0	0	0	0	39.59	39.59	39.59	39.59
H_2 at reactor exit	129.18	129.18	129.18	129.18	129.18	129.18	129.18	129.18	129.18	129.18

Appendix B

Result of trigeneration process consisting of a proton conducting solid oxide fuel cell and a LiBr absorption chiller

Data result of trigeneration process consisting of a proton conducting solid oxide fuel cell and a LiBr absorption chiller

Table B.1 Model validation of experimental data and numerical result of proton conducting solid oxide fuel cell at operating temperature 550 to 700 ℃ and validated with Zhang et al. [54]

Temperature (℃)	Current density (A/cm^2)	Cell voltage from experiment (V)	Cell voltage from simulation(V)
	1.2	0.18	0.17
	1.0	0.30	0.31
700	0.8	0.4	0.44
	0.6	0.52	0.58
	0.4	0.66	0.73
	0.2	0.78	0.88
	1.0	0.14	0.11
	0.8	0.28	0.27
650	0.6	0.42	0.44
	0.4	0.58	0.63
	0.2	0.82	0.82
	0.8	0.08	0.06
	0.6	0.28	0.26
600	0.4	0.48	0.48
	0.2	0.7	0.73
550	0.4	0.32	0.29
	0.2	0.6	0.59

Table B.2 Effect of SOFC-H^+ operating temperature on cell voltage at operating pressure = 1 bar, hydrogen feeding molar flow rate = 1 kmol/hr , Air to fuel ratio 2.78 and fuel utilization factor = 0.8

Operating temperature (°C)	Cell voltage (V)	Activation Overpotential (V)	Concentration Overpotential (V)	Ohmic Overpotential (V)	Power density (W/cm^2)
550	0.775	0.185	0.0001501	0.104	0.0796
600	0.876	0.096	0.0001689	0.081	0.0899
650	0.930	0.047	0.0001888	0.065	0.0955
700	0.953	0.023	0.0002098	0.054	0.0980

Table B.3 Effect of SOFC-H^+ operating pressure on cell voltage at operating pressure = 1 bar, hydrogen feeding molar flow rate = 1 kmol/hr , Air to fuel ratio 2.78 , operating temperature = 550 ℃ and fuel utilization factor = 0.8

Operating pressure (bar)	Cell voltage (V)	Activation Overpotential (V)	Concentration Overpotential (V)	Ohmic Overpotential (V)	Power density (W/cm^2)
1	0.7756	0.1855	0.000150	0.1045	0.0796
2	0.7880	0.18555	5.2843E-05	0.1045	0.0809
3	0.7952	0.18555	3.03046E-05	0.1045	0.0816
4	0.8003	0.18555	2.08832E-05	0.1045	0.0821
5	0.8043	0.18555	1.5821E-05	0.1045	0.0826
6	0.8075	0.18555	1.26923E-05	0.1045	0.0829
7	0.8103	0.18555	1.0578E-05	0.1045	0.0832
8	0.8126	0.18555	9.05812E-06	0.1045	0.0834
9	0.8147	0.18555	7.91505E-06	0.1045	0.0836
10	0.8166	0.18555	7.02518E-06	0.1045	0.0838

Table B.4 Effect of fuel utilization factor on cell voltage at operating pressure = 1 bar, hydrogen feeding molar flow rate = 1 kmol/hr , Air to fuel ratio 2.78 and operating temperature = 550 ℃ and operating pressure = 1 bar

Fuel utilization factor	Cell voltage (V)	Activation Overpotential (V)	Concentration Overpotential (V)	Ohmic Overpotential (V)	Power density (W/cm^2)
0.8	0.7756	0.1855	0.0001501	0.1045	0.0796
0.85	0.7618	0.19284	0.0001595	0.1110	0.0831
0.90	0.74815	0.19993	0.0001690	0.11764	0.0864
0.95	0.73494	0.20662	0.0001783	0.12416	0.0896

Table B.5 Effect of air to fuel molar ratio in proton conducting solid oxide fuel cell on cell voltage at operating pressure = 1 bar, , Air to fuel ratio 2.78 and operating temperature = 550 ℃ .

Hydrogen molar flow rate (kmol/hr)	Air molar flow rate (kmol/hr)	Air to fuel molar ratio (-)	Cell voltage (V)	Activation Overpotential (V)	Concentration Overpotential (V)	Ohmic Overpotential (V)	Power density (W/cm^2)	Enthalpy to mole of exhaust SOFC-H^+ stream (kJ/mol)
1	1	1	0.7829	0.1865	0.000169	0.1053	0.0810	-40.35
1	2	2	0.7714	0.1865	0.000147	0.1053	0.0798	-61.96
1	3	3	0.7760	0.1865	0.000155	0.1053	0.0803	-52.39
1	4	4	0.7850	0.1865	0.000173	0.1053	0.0812	-37.20
1	5	5	0.7920	0.1865	0.000192	0.1053	0.0820	-27.54
1	6	6	0.7980	0.1865	0.000211	0.1053	0.0825	-20.85
1	7	7	0.8030	0.1865	0.000223	0.1053	0.0831	-15.94
1	8	8	0.8073	0.1865	0.000248	0.1053	0.0835	-12.19
1	9	9	0.8113	0.1865	0.000267	0.1053	0.0840	-9.22
1	10	10	0.8150	0.1865	0.000285	0.1053	0.0843	-6.83

Table B.5 (Continue) Effect of air to fuel molar ratio in proton conducting solid oxide fuel cell on cell voltage at operating pressure = 1 bar, , Air to fuel ratio 2.78 and operating temperature = 550 ℃ .

Hydrogen molar flow rate (kmol/hr)	Air molar flow rate (kmol/hr)	Air to fuel molar ratio (-)	Cell voltage (V)	Activation Overpotential (V)	Concentration Overpotential (V)	Ohmic Overpotential (V)	Power density (W/cm^2)	Enthalpy to mole of exhaust SOFC-H^+ stream (kJ/mol)
2	1	0.5	0.604	0.2756	0.00042	0.210	0.1250	-20.37
2	2	1	0.588	0.2756	0.00033	0.210	0.1217	-40.35
2	3	1.5	0.581	0.2756	0.00030	0.210	0.1202	-53.11
2	4	2	0.576	0.2756	0.00029	0.210	0.1194	-61.96
2	5	2.5	0.576	0.2756	0.00029	0.210	0.1192	-63.78
2	6	3	0.581	0.2756	0.00031	0.210	0.1203	-52.39
2	7	3.5	0.586	0.2756	0.00032	0.210	0.1213	-43.85
2	8	4	0.590	0.2756	0.00034	0.210	0.1222	-37.20
2	9	4.5	0.594	0.2756	0.00036	0.210	0.1229	-31.89
2	10	5	0.597	0.2756	0.00038	0.210	0.1236	-27.54

Table B.5 (Continue) Effect of air to fuel molar ratio in proton conducting solid oxide fuel cell on cell voltage at operating pressure = 1 bar, , Air to fuel ratio 2.78 and operating temperature = 550 °C.

Hydrogen molar flow rate (kmol/hr)	Air molar flow rate (kmol/hr)	Air to fuel molar ratio (-)	Cell voltage (V)	Activation Overpotential (V)	Concentration Overpotential (V)	Ohmic Overpotential (V)	Power density (W/cm^2)	Enthalpy to mole of exhaust SOFC-H^+ stream (kJ/mol)
3	1	0.33	0.453	0.331	0.00077	0.316	0.1408	-10.94
3	2	0.66	0.435	0.331	0.00057	0.316	0.1353	-28.18
3	3	1.00	0.427	0.331	0.00050	0.316	0.1326	-40.35
3	4	1.33	0.421	0.331	0.00047	0.316	0.1310	-49.40
3	5	1.66	0.418	0.331	0.00045	0.316	0.1299	-56.40
3	6	2.00	0.415	0.331	0.00044	0.316	0.1290	-61.96
3	7	2.33	0.413	0.331	0.00043	0.316	0.1284	-66.50
3	8	2.66	0.416	0.331	0.00044	0.316	0.1294	-59.588
3	9	3.00	0.420	0.331	0.00046	0.316	0.1305	-52.39
3	10	3.33	0.423	0.3311	0.00048	0.316	0.1315	-46.45

Table B.5 (Continue) Effect of air to fuel molar ratio in proton conducting solid oxide fuel cell on cell voltage at operating pressure = 1 bar, , Air to fuel ratio 2.78 and operating temperature = 550 ℃ .

Hydrogen molar flow rate (kmol/hr)	Air molar flow rate (kmol/hr)	Air to fuel molar ratio (-)	Cell voltage (V)	Activation Overpotential (V)	Concentration Overpotential (V)	Ohmic Overpotential (V)	Power density (W/cm^2)	Enthalpy to mole of exhaust SOFC-H^+ stream (kJ/mol)
4	1	0.25	0.3160	0.3712	0.00120	0.421	0.1308	-5.44
4	2	0.5	0.2971	0.3712	0.00085	0.421	0.1230	-20.37
4	3	0.75	0.2876	0.3712	0.000738	0.421	0.1190	-31.60
4	4	1	0.2816	0.3712	0.000679	0.421	0.1166	-40.35
4	5	1.25	0.2774	0.3712	0.000643	0.421	0.1148	-47.37
4	6	1.5	0.2743	0.3712	0.000619	0.421	0.1136	-53.11
4	7	1.75	0.2719	0.3712	0.000603	0.421	0.1126	-57.90
4	8	2	0.2700	0.3712	0.000590	0.421	0.1118	-61.96
4	9	2.25	0.2685	0.3712	0.000580	0.421	0.1112	-65.44
4	10	2.5	0.2692	0.3712	0.000585	0.421	0.1115	-63.78

Table B.5 (Continue) Effect of air to fuel molar ratio in proton conducting solid oxide fuel cell on cell voltage at operating pressure = 1 bar, , Air to fuel ratio 2.78 and operating temperature = 550 ℃ .

Hydrogen molar flow rate (kmol/hr)	Air molar flow rate (kmol/hr)	Air to fuel molar ratio (-)	Cell voltage (V)	Activation Overpotential (V)	Concentration Overpotential (V)	Ohmic Overpotential (V)	Power density (W/cm^2)	Enthalpy to mole of exhaust SOFC-H^+ stream (kJ/mol)
5	1	0.2	0.1854	0.4025	0.00170	0.526	0.0959	-1.84
5	2	0.4	0.1659	0.4025	0.00110	0.526	0.0858	-14.94
5	3	0.6	0.1557	0.4025	0.00090	0.526	0.0806	-25.23
5	4	0.8	0.1492	0.4025	0.00090	0.526	0.0772	-33.52
5	5	1	0.1446	0.4025	0.00080	0.526	0.0748	-40.35
5	6	1.2	0.1412	0.4025	0.00080	0.526	0.0731	-46.08
5	7	1.4	0.1385	0.4025	0.00078	0.526	0.0717	-50.94
5	8	1.6	0.1364	0.4025	0.00076	0.526	0.0706	-55.13
5	9	1.8	0.1346	0.4025	0.00075	0.526	0.0697	-58.77
5	10	2	0.1331	0.4025	0.00074	0.526	0.0689	-61.96

Table B.5 (Continue) Effect of air to fuel molar ratio in proton conducting solid oxide fuel cell on cell voltage at operating pressure = 1 bar, , Air to fuel ratio 2.78 and operating temperature = 550 ℃ .

Hydrogen molar flow rate (kmol/hr)	Air molar flow rate (kmol/hr)	Air to fuel molar ratio (-)	Cell voltage (V)	Activation Overpotential (V)	Concentration Overpotential (V)	Ohmic Overpotential (V)	Power density (W/cm^2)	Enthalpy to mole of exhaust SOFC-H^+ stream (kJ/mol)
6	1	0.16	0.0594	0.4282	0.0023	0.632	0.0369	0.68
6	2	0.33	0.0395	0.4282	0.00154	0.632	0.0245	-10.94
6	3	0.50	0.0289	0.4282	0.00128	0.632	0.0180	-20.37
6	4	0.66	0.0221	0.4282	0.00115	0.632	0.0137	-28.18
6	5	0.83	0.0172	0.4282	0.00107	0.632	0.0106	-34.75
6	6	1.00	0.0135	0.4282	0.00102	0.632	0.0083	-40.35
6	7	1.16	0.0106	0.4282	0.00098	0.632	0.0065	-45.19
6	8	1.33	0.0082	0.4282	0.00095	0.632	0.0051	-49.40
6	9	1.50	0.0063	0.4282	0.00093	0.632	0.0039	-53.11
6	10	1.66	0.0046	0.4282	0.00091	0.632	0.0028	-56.40

CURRICULUM VITAE

Name-Surname: Mr. Ratikorn Sornumpol

Date of Birth: January 26, 1988

University Education:

Bachelor's degree

2006 – 2010 King Mongkut 's University Technology Thonburi Bangkok , Faculty of Engineering, Department of Chemical Engineering, Bangkok, Thailand

Master's degree

2013 – 2015 Chulalongkorn University, Faculty of Science, Department of Chemical Technology, Bangkok, Thailand

Published research paper:

1. Sornumpol, R., Saebea, D., Arpornwichanop, A., & Patcharavorachot, Y. (2023). Process Optimization and CO_2 Emission Analysis of Coal/Biomass Gasification Integrated with a Chemical Looping Process. *Energies, 16(6), 272.*

2. Sornumpol, R., Arpornwichanop, A., & Patcharavorachot, Y. (2023). Performance analysis and optimization of a trigeneration process consisting of a proton-conducting solid oxide fuel cell and a LiBr absorption chiller. *International Journal of Hydrogen Energy, 48(18), 6837-6854.*